

Modelling of Serrated Trailing Edges to Reduce Aerodynamic Noise in Wind Turbines Using Computational Fluid Dynamics

Carlos A. Arce-León



UPPSALA
UNIVERSITET

**Teknisk- naturvetenskaplig fakultet
UTH-enheten**

Besöksadress:
Ångströmlaboratoriet
Lägerhyddsvägen 1
Hus 4, Plan 0

Postadress:
Box 536
751 21 Uppsala

Telefon:
018 – 471 30 03

Telefax:
018 – 471 30 00

Hemsida:
<http://www.teknat.uu.se/student>

Abstract

Modelling of Serrated Trailing Edges to Reduce Aerodynamic Noise in Wind Turbines

Carlos A. Arce-León

An analysis is pursued on how serrations fitted on a section of a wind turbine blade affect noise generation and properties, seeking to ultimately verify its noise mitigation effects. The research is conducted using computational fluid dynamics with aid from a basic acoustic model following the theory developed by Proudman and Lilley, coupled with an analysis of sound properties by the characterization of turbulence length scales present in the flow. An outline of the numerical methods, aeroacoustic principles and the theory behind trailing edge noise generation is presented in order to achieve a more complete understanding of why noise is generated, with what means it can be studied and how it can ultimately be modified. It is found that, for the case at hand, turbulent structures become complex and anisotropic due to the presence of the serrations, thus cutting down on the effectiveness of the chosen acoustic model. The turbulence length scale analysis is used to compliment this method and, by coupling the results from both methods, a conclusion is reached on that noise can be mitigated by using serrated trailing edges since they extend the presence of a more varied range of turbulence length scales, thus reducing the effect of constructive interference from pressure fluctuations generated by eddies shed from the trailing edge of the blade.

Handledare: Peter Fuglsang
Ämnesgranskare: Per Lötstedt
Examinator: Anders Jansson
IT 10 053
Sponsor: LM Wind Power

Tryckt av: Reprocentralen ITC

To all who in my past I hold dear, for every word and gesture has helped me sculpt who I am, what I've done and where I want to go.

To all, but to none a greater debt of gratitude than to my parents, my brother and grandparents I owe.

ACKNOWLEDGEMENTS

First and foremost, thanks to my parents; it's only because of their support, education and touring of the world that I've been able to make it this far.

Thanks to everyone that has ever given me the opportunity to learn and grow from their insight, ideas and beliefs, be that in a classroom or over coffee some afternoon.

A special thanks to the supervisors of this research, Per Lötstedt and Peter Fuglsang, for the much needed insight, information, suggestions and especially for the time they've invested in it. Thanks also to Jesper Madsen for taking the time to provide the crucial simulation data used in this study.

To my friends, here and far away, for motivating a gasp of fresh air and a healthy escape from the routine. Also for bringing back the pleasure of having music in my life again.

Thanks to professor Gunilla Kreiss, with whom it was an honour to work in a project which, not only has greatly influenced the writing of this thesis, but also allowed me to sharply expand my horizons into this world of computational science. To professors Stefan Pålson and Michael Thuné for their very valuable guidance in this M.Sc. program.

A huge recognition of appreciation to prof. Herman Snel, the inspiration and catalyst that introduced me to the art and science of wind energy and without whom this thesis and my cooperation with LM Wind Power would never have been conceived.

I'm in great debt to the open source community, without which I truly believe that achieving this research would never have been so rewarding and fun. Especial thanks to the developers of \LaTeX ¹, Vim² and its \LaTeX -Suite, Octave³, GIMP⁴, Inkscape⁵ and Blender⁶. To the GNU/Linux community, and KitWare for their magnificent VTK⁷ and Paraview⁸ products. But most of all, thanks to the people that have introduced me to all these amazing possibilities and motivated me to take a jump in the deep end. Especially thanks to Dr.rer.nat. Marcelo Magallón, who introduced me to the world of computational science and whom I'll always consider to be my mentor back home, and Dr.rer.nat. Francisco Frutos, to whom, amongst many other things, I owe the pleasure of first hearing about \LaTeX .

Lastly, I extend my deepest appreciation to both the University of Costa Rica and Uppsala University for sheltering me in the academic environment I've always looked for, and by doing so, helping me make so many dreams come true.

¹www.latex-project.org

²www.vim.org

³www.gnu.org/software/octave/

⁴www.gimp.org

⁵www.inkscape.org

⁶www.blender.org

⁷www.vtk.org

⁸www.paraview.org

CONTENTS

1	Introduction	1
1.1	Social Impact of Wind Turbine Noise	3
1.2	Sources of Wind Turbine Noise	6
2	Numerical Methods in CFD	11
2.1	The Navier-Stokes Equations	12
2.2	Turbulence	15
2.3	Direct Numerical Simulation	16
2.4	Large Eddy Simulation	17
2.5	Reynolds Averaged Navier-Stokes Models	18
3	Aeroacoustics	23
3.1	The Lighthill Analogy	25
3.2	The Ffowcs-Williams and Hawkings Analogy	27
3.3	The Proudman/Lilley Approach	30
3.4	Computational Aeroacoustics and its Issues Regarding Computational Expense	31
4	Theory of Noise Generation by Trailing Edges	35
4.1	The Theory of Noise Generated by a Straight Trailing Edge	35
4.2	Computational Aeroacoustic Research on Straight Trailing Edge Sound Generation	40
4.3	Computational Aeroacoustic Research on Straight Trailing Edge Wind Turbine Blades	43
4.4	The Effect of Serrated Trailing Edges on Sound Generation	46
4.5	Trailing Edges Noise Generation and Experimental Research	50
5	Case Set Up	55
5.1	Blade Geometry	55
5.2	2D Set Up	57
5.3	3D Set Up	59
6	Simulations and Results	65
6.1	The 2D Case	65
6.2	The 3D Case	72
7	Conclusions	83
7.1	Further Work	84

A	Definitions	87
A.1	Reynolds Number, Re	87
A.2	The Dimensionless Wall Distance, y^+	87
A.3	The Dirac Delta Function, $\delta(x)$	88
A.4	Green's Function	88
A.5	Wedge Product, \wedge	89
	References	90
	Acronyms	95

NOMENCLATURE

α	Angle of attack (AOA)	$\overline{\rho u'_i u'_j}$	Reynolds stress
Δ	Length scale	σ	Stress tensor
$\delta(f)$	Dirac delta function	σ_{ij}	Normal stress component ij
δ_{ij}	Kronecker delta function	τ_{ij}	Shear stress component ij
κ	Kármán constant	τ_w	Wall shear stress
κ_0	Acoustic wave number	θ	Elevation angle
λ	Bulk viscosity of a fluid	ε	Turbulence kinetic energy dissipation
λ	Serration wavelength	$\varphi^*(\mathbf{x})$	Flow velocity potential
$\boldsymbol{\Omega}(\mathbf{x}, t)$	Vorticity	T	Total time
μ	Coefficient of viscosity	U	Characteristic velocity of energy containing eddies
∇	Differential operator	$a'(x_i, t)$	Fluctuation around a variable $a(x_i, t)$
ν	Kinematic viscosity	Ma	Mach number
ν_T	Eddy viscosity	a_n	n -th order coefficient of the differential equation
ω	Acoustic angular frequency	Re	Reynolds number
\bar{a}	Mean value of the variable a	\mathbf{a}	Vector of components (a_1, a_2, \dots, a_n)
$\partial\Omega$	Surface of volume Ω	B	Total enthalpy
Φ	Function representing the dissipation of energy due to viscous effects	c_0	Speed of sound
$\phi(\mathbf{x}, t)$	Velocity potential	C_d	Drag coefficient
$\Phi(\omega, \mathbf{x})$	Acoustic pressure frequency spectrum	C_l	Lift coefficient
$\Phi^*(\mathbf{x})$	Incompressible flow potential	dA	Infinitesimal part of an area
ψ	Azimuthal angle	D/Dt	Convective derivative
ρ	Density	dV	Infinitesimal part of a volume

\mathbf{F}	Body force vector	p_I	Pressure inherent to an environment
\mathbf{f}	Force vector		
f_{\max}	Maximum acoustic frequency	p_{ij}	Stress tensor for a Stokesian gas
f_{\min}	Minimum acoustic frequency	p'_L	Loading noise
$G(x, x')$	Filter kernel	p_{op}	Operating pressure
$G(x, z)$	Green's function	p'_T	Thickness noise
Δ_g	Grid size	\mathbf{r}	Position vector
h	Enthalpy	R	Universal gas constant
h	Serration amplitude	Re_λ	Taylor-scale Reynolds number
I	Identity matrix	R_{ij}	Subgrid-scale Reynolds stress tensor
$I(\mathbf{x})$	Intensity of sound as measured at position \mathbf{x}	S	Sources/sinks
\mathbf{K}	Turbulent eddy wavenumber	\mathbf{T}	Deviatoric stress
\mathbf{k}	Fourier component vector	T	Temperature
k	Boltzmann constant	t	Time
k	Turbulence kinetic energy	Δt	Simulation time step
k_T	Eddy wave number	Δt	Time step
k_i	i^{th} Fourier component	T_{ij}	Lighthill's tensor
\mathcal{L}	Linear differential operator	\mathbf{u}	Fluid velocity
L	Turbulence integral length scale	U	Free stream velocity
l'	Turbulence length scale	u^+	Dimensionless velocity
L_p	Sound pressure level	U_∞	Free stream velocity
L_W	Sound power level	\mathbf{u}^a	Acoustic part of the velocity perturbation \mathbf{u}'
M_w	Molecular weight	U_c	Eddy convection velocity
\mathbf{n}	Normal vector	u_i	Velocity in the i -th spacial dimension
\wedge	Exterior product operator	u_k	Velocity perturbation of eddy with wave number k
P	Sound power	\mathbf{u}^ν	Solenoidal part of the perturbation velocity \mathbf{u}'
p	Effective sound pressure		
p	Pressure		
$p'(\mathbf{x}, t)$	Acoustic pressure		
P_0	Sound power reference level	u_τ	Friction velocity
p_0	Effective sound pressure reference level	$x_1 \ x_2 \ x_3$	Spacial coordinates
P_A	Acoustic power due to unit volume of isotropic turbulence	y^+	Dimensionless wall distance

INTRODUCTION

Our ever growing need for energy headlines today's news in a shade of green. Human nature has always led us to pursue a life of greater advancements, of comfort, travel, security, of fun and every other behaviour that will ultimately lead us to be happier and more fulfilled—or at least make us think that we will be. The only common factor amongst our actions is that, whatever we chose to do, we will require energy to do it; we *do* have to follow the laws of thermodynamics, like it or not. Our thirst for energy has always been palpable and for many years now the answer to quench it has been found comfortably in the relatively cheap priced oil and coal solution.

But since about two decades ago, a once lonely and quiet voice has been ringing in society's ears of conscience warning us about their dangers and what consequences they may bring upon us and, what was once inconceivable, to the entirety of our planet and the rest of its inhabitants. A physical and chemical issue, simply put, a meddling of nature's own cycles, a slight perturbation in its inner workings that has gone from being just a lone warning light to a renewal of human kind's consciousness and a era of relearning of global proportions. An issue that was once in the mouth of a few has now spread through the fabrics of society, politics, science, and basic human behaviour to become a scream that we can only hope has arrived in time.

Alternatives are sought, options are reborn. Our technology, that which has turned us into gas and coal consuming addicts, will have to rise and save us—or so it could be said if one were to blame it for what is really ours. It has been a while since we've realized that we need to change our ways, but we've turned our heads for too long to the fact that it is us who must build the crossroad and then have the courage and a certain amount of self-sacrifice to actually take the turn. But far from the technological potential not being there and ready, it's our willingness and effort to embrace it that is lacking. The ideas have been around, the technology is there, scientists from all over the world have just been waiting for the change, the funding, the go-ahead to tackle this problem. And it's because of a brave few of our kind that finally we've started to move forward.

Ultimately it is an issue of relearning what we've been taught and regaining perspective on how we've come to see our world and even our own technology. For example, who could bluntly have predicted that those little solar cells that were once powering our (once very technologically advanced) hand-held calculators would one day grow into powerful interconnected arrays that could light up a whole city? Or how about considering using the power that the Sun and the Moon have on our oceans to, in turn, convert its movement into light and heat? Or perhaps to look back to search for the answer in how we once milled our grains to make bread and pumped water from the ground? Wind, a driving force that has been faithful to us throughout our history and has just been waiting to mature.



Figure 1.1: The Enercon E-126 wind turbine, the largest turbine manufactured at the time of writing this thesis, with a rotor diameter of 125m, a height of 198m and an output capacity of 7MW (Image source: http://en.wikipedia.org/wiki/File:E_126_Georgsfeld.JPG, attributed to author “Jfz”).

Consider the time it took us to develop the technology to extract useful energy from oil. In 1824 Sadi Carnot established the thermodynamic theory of idealized heat engines, in 1870 the first mobile gasoline engine was put on a handcart by Siegfried Marcus, in 1885 Karl Benz put the first automobiles in production, and in 1897 Rudolph Diesel developed the diesel engine and its physics. On the other hand, the first instance of a known wind powered machine dates all the way back to the 1st century AD, built by Heron of Alexandria—and if one considers that wind has been powering sailing ships, its history then goes back over 5500 years. The underlying issue in advancement lies not so much in the *how* but instead in our own will.

It has been a while but our priorities are beginning to change. The amount of people that are aware of that electricity can be processed from wind gets larger by the day. And, perhaps more importantly, so is the amount of policy makers that are aware that, not only it exists, but that it’s also becoming even more profitable—in case that aiming to have a habitable planet for still a few more years is not convincing enough. The wind power industry now is in a very interesting juncture in its development; it has gained visibility and is being fuelled by a growing concern for the environment. It’s leading a technology of change. But with every change comes resistance, a maxim that is shown not only to be true in physics but also in the complicated workings of social and human behaviour.

Although welcomed by many, alternatives such as solar energy, tidal energy, biomass, do have their opponents. And by all means should this be that way. If there would have been more opponents to coal and oil, we would have perhaps averted the ecological problems we’re now facing. But it mostly boils down to how one gets the information that’s used to oppose, how that information was researched and also how it is read. For example, many are against wind turbines because they are said to kill birds and, unfortunately, this is undeniably true. In fact, in the migratory year of 1986, 38 dead birds were found in the proximity of the San Geronio Pass wind farm near Palm Springs in the United States; but that same year 69 million birds migrated through that same route. So, in other words, the amount of birds struck and killed by wind turbines at San Geronio Pass represent 0.00006% of the birds that migrate close to it in a regular year; hardly a number to consider. And to put things in further perspective, it is reported that utility transmission and distribution lines are responsible for 130 to 174 million bird deaths per year; automobile and truck collisions, between 60 and 80 million; building collisions, between 100 million and 1000 million; agricultural pesticides, about 67 million. So, even if one would only considers bird collisions with man-made structures, wind turbines are estimated to

represent about only 0.01% to 0.02% of direct bird deaths of that kind. To cite another example, in the Altamont Pass wind farm it's estimated that 92 birds are killed a year, a relatively high amount for a wind farm, yet it would take it 500 to 1000 years of operation time to equal the same bird mortality level as the Exxon Valdez oil spill did in 1989 (Sagrillo 2010)

Opposition of course goes beyond environmental impact and into direct human impact. The difficulties that this brings up are multiple and of a very different nature than counting migratory birds, especially when complaints of a subjective nature are made. Such voiced concerns are particularly strong regarding the unsightliness wind farms in the horizon, the flickering that their blades produce during daytime, and the noise they make. The first case is of a purely aesthetic nature that could non the less be of big importance if the presence of a wind turbine would affect the real estate market surrounding it, but there are studies such as (Hoen, Wiser, Cappers, Thayer and Sethi 2009) where no effect on a market has been found. The other two conditions are much harder to analyse as they pose perceptual and psychological elements that may have deeper effects on a person's quality of life. The flicker effect won't be pursued much further in this thesis and, being noise reduction possibilities in a wind turbine its main objective, an overview of what the current state is on wind turbine noise studies, research and impact from a social point of view shall be given next.

1.1 Social Impact of Wind Turbine Noise

Wind energy is in many ways a maturing technology where rapid advancements achieved in efficiency and design require a quick response from all its related fields. One such case is its impacts on the quality of life of the inhabitants and animals residing close to where wind farms are located, in which case the acoustic footprint is of particular importance. Non the less, the lag in research and consensus about its consequences is felt by an evident discrepancy in the most basic levels between opponents and proponents of wind energy projects, a situation that naturally hinders the proper development of this technology.

In fact, studies on which wind energy noise regulation are based are often out of date in correspondence to the rapidly advancing technology and physical growth of wind turbines. For example, the current document on which wind farm projects in the United Kingdom are regulated, (Ene 1997), is based on studies carried out back in 1997. It must be taken into account that at that time wind turbine rotor size was just developing past the 50m mark¹ (see Figure 1.2) while at the time of writing of this thesis it is not uncommon to find rotor sizes of some 126m in diameter.

A research was conducted in 2007 by request of the Government of the UK, (Moorhouse, Hayes, von Hünenbein, Piper and Adams 2007), on the aerodynamic modulation of wind turbine noise as a response to pressure by popular demand but it was disregarded and (Off 2004) is continued to be used as a guideline for the planning of wind energy projects and refers to (Ene 1997), mentioned above, as its main reference:

“Take into account noise issues according to PAN 45 and the recommended good practice in The Assessment and Rating of Noise from Wind Farms, ETSU for OTI 1996. This is kept under review and led to research on Aerodynamic Modulation of Wind Turbines

Have regard to Issues raised by members of the community, including positive and negative opinions; and bear in mind the relevance of the research findings (...) regarding public attitudes to wind farms”

where PAN 45 is a reference to (Sco 2002) and the ETSU document to (Ene 1997).

¹Source: Garrad Hassan through “Wind Energy The Facts” at <http://www.wind-energy-the-facts.org>

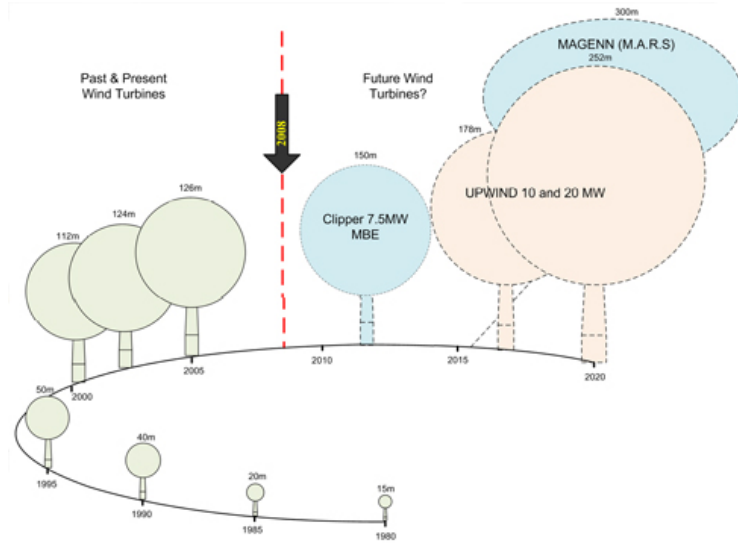


Figure 1.2: Wind turbine growth over the years. Source: Garrad Hassan

Country	Day time limit	Night time limit
UK	5 dB above background noise	5 dB above background noise
France	5 dB above background noise	3 dB above background noise
Denmark	85 dB of infrasound noise	85 dB of infrasound noise
	25 dB of low frequency noise	20 dB of low frequency noise
	30 dB usual noise limit	25 dB usual noise limit
S. Australia	Cannot exceed 35 dB for 10% of the time or background noise +5 dB for 90% of the time	
Michigan (USA)	55 dB at closest residence line and ambient noise +5 dB if ambient noise exceeds 55 dB	

Table 1.1: Noise level regulations for wind farms in different legislative territories.

Examples of noise level regulations in the UK and other countries can be found in (Weed 2006) and some are summarized in Table 1.1. When reading this table one should take into account that a car at 56 km/h produces 55 dB measured at 100 m and rural night time noise can reach 40 dB (Sco 2002). The formulating of a noise limit should ideally come from a thorough research on what effects noise, its intensity and type, has on the human body and psyche. But, as it's seen in the next section, the state of this is far from ideal.

1.1.1 Studies on the health effects caused by wind turbine related noise

Often noise issues will be addressed concerning its intensity level, case which is of interest in scenarios like airport planning, construction site management, factories and other potentially loud elements in modern urban and rural environments. But in the case of wind farms, negative noise effects can also be caused by more than just high sound volume and special care must be taken to research other kinds of disturbances such as those produced by low frequency and periodic noise generation.

In (Herbrandson and Messing 2009), high frequency noise was found to be of much lesser concern as it is often attenuated in short distances and especially so by walls and windows of normal households, providing a special protection when indoors. On the other hand, low frequency noise is said to transfer much easier through open spaces and also the structural elements of a house, thus causing a particular problem where insulation is typically unavailable and people are said often to be found especially annoyed at night time. It states:

“The most common complaint in various studies of wind turbine effects on people is annoyance or an impact on quality of life. Sleeplessness and headache are the most common health complaints and are highly correlated (but not perfectly correlated) with annoyance complaints. Complaints are more likely when turbines are visible or when shadow flicker occurs. Most available evidence suggests that reported health effects are related to audible low frequency noise. Complaints appear to rise with increasing outside noise levels above 35 dB. It has been hypothesized that direct activation of the vestibular and autonomic nervous system may be responsible for less common complaints, but evidence is scant.”

Here “low frequency” refers to noise below 20 Hz to 100 Hz, which is considered to be at the very low end of the auditory human range, yet this study suggests that its effects on health are unknown and it could be picked up by other systems in the human body, not only the audible. Furthermore it is noted that people have been found with audible sensibility down to 12.5 Hz and that noise pollution studies are usually not carried out taking into account frequencies as low as this one.

It must also be noted that perception of wind turbine presence is related to personal tolerance to the disturbances created by it, not only on their physical capabilities to perceive them. In other words, people with identical physical characteristics could still be annoyed in different amounts depending on their independent ability to ignore those disturbances. For example, some people are just more capable of sleeping in a noisier environment than others, and this fact will cause big differences in health effect study results as it would be possible to find no apparent common ground in the complainers’ nature and trend. One trend that could be of importance is that wind farms will usually be located in rural environments where people have, either become very accustomed to the naturally low noise and disturbance level of these environments, or are actually seeking them by having moved from an urban area. Therefore individuals near rurally located wind farms may actually be more susceptible to noise and other effects they create on the surroundings like light flicker and general landscape morphology.

In (Fields 1990) a psychological background on noise annoyance is presented where the following conclusions are drawn:

- The awareness of non-noise problems increases annoyance.
- Fear of noise source increases annoyance.
- The belief that the noise could be prevented increases annoyance.

It goes on to suggest that if people are instead convinced that the source of the noise is important, i.e. the need for wind turbines in this case, the annoyance level is decreased.

Because of the clear psychological importance of the noise impact factor, in parallel to research on noise reduction at a scientific and engineering level, a very carefully devised strategy in public relations must be also be adopted. In (Garrad 1991) it’s stated that

“There is a (...) not-in-my-back-yard attitude over wind energy as over the majority of industrial developments. However, unlike most other developments the public is, given its increasing greenness, basically well disposed to the development of wind

energy. From experience in Denmark and The Netherlands, the successful development of wind farms seems to depend on providing the public with enough information to be able to make an informed decision. The tendency to approach wind farm developments with a ‘big brother’ attitude has been disastrous and must be avoided. It is important to capitalize on people’s positive attitudes towards wind energy as opposed to polluting coal and nuclear stations”

Furthermore, (Wagner, Bareiss and Guidati 1996) states that

“Opinion about the turbines may change as is reported in the study carried out by Exeter University about public acceptance near the Delabole wind farm in UK which increased from 17% before construction of the wind farm to 85% after the wind farm had commenced operation.”

So it is of great value for the successful implementation of wind farm projects to acknowledge that the *source* of noise is not necessarily located only at the blades of a wind turbine and instead its impact is often influenced by much more than just aerodynamics. Non the less it’s also necessary to gather perspective through knowledge and research on how much more wind turbine sound generation can be minimized. This task must be celebrated and communicated as an important part of the growing worldwide effort to harness renewable energy in tandem with the objective of achieving also a socially aware development.

1.2 Sources of Wind Turbine Noise

1.2.1 General sound considerations

Sound is defined as a quick fluctuation in pressure in a medium, be it gaseous like air, solid or liquid (Rogers and Manwell 2004). It is perceived by humans through the medium’s interaction with the auditory system and other organs as vibrations. Sound with an adverse effect on the observer is addressed as *noise* and can be caused by different properties in the pressure fluctuations such as high powered sound, high pitched sound (in relation to its frequency), low pitched sound and its pulsating characteristics.

Sound power and sound pressure measurements are related to each other in the sense that they both involve the intensity with which sound is perceived. The difference is that sound power is the intensity at which sound is generated by the causing mechanism and sound pressure is instead related to the intensity at which the observer perceives it to be at its location. By increasing sound power, sound pressure will also be increased if medium properties are not changed, but by changing them or by changing the location at which measurements are being taken, sound pressure will vary without changing sound power at the source. This is of importance when analysing data for wind farm location and sound effects since wind direction, terrain shape and distance from inhabited places will sharply affect the results even when using the same wind turbine configuration.

The sound power level of a source is measured in [dB] as

$$L_W = 10 \cdot \log_{10} (P/P_0)$$

with P the sound power of the source and P_0 a reference level. Sound pressure level is measured, also in [dB], as

$$L_p = 20 \cdot \log_{10} (p/p_0)$$

where p is the effective sound pressure and p_0 is a reference level. Usually $P_0 = 10^{-12}$ W and $p_0 = 20 \times 10^{-5}$ Pa (Rogers and Manwell 2004). The threshold of pain for the human ear is set at around 200 Pa, thus 140 dB.

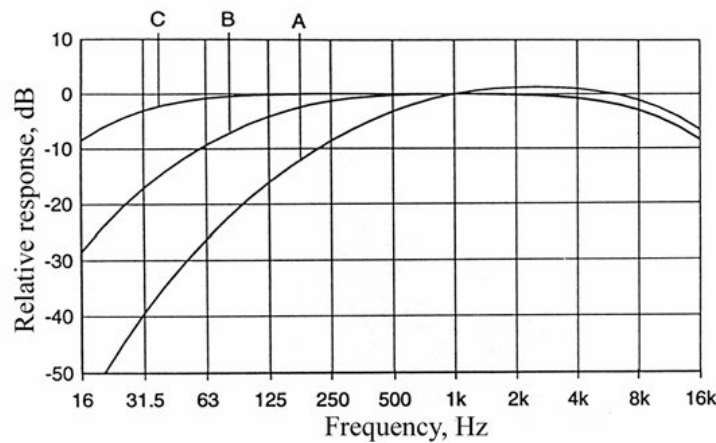


Figure 1.3: Graph outlining the various sound filters used to compensate for differences in human sound perception at different frequencies (Beranek and Vér 1992).

The human ear perceives sound pressure at different levels for different frequencies since the eardrum is a non linear oscillator (Aerts and Dirckx 2009), so care must be taken that general sound pressure increase or decrease at two different frequencies will not always render the same perceptual results, not even considering samples from the same group of people. To address this issue, several filters can be used to weigh data differently at different frequencies. These can be observed in Figure 1.3. Usually filter A is used for environmental noise assessment and results are expressed in units of [dB (A)].

1.2.2 Sound generation from wind turbines

As most—if not all—mechanical devices, wind turbines aren’t exempt from some level of noise generation and, being one that interacts with the flowing dynamics of air, it has special aeroacoustic considerations that must be taken into account and which turn the problem or noise generation into a more complex one.

Typical causes of sound are general moving parts in devices. These may produce it as a consequence of poor design, poor lubrication, electromechanical elements that can vibrate, or simply because of an inevitability-by-definition consequence that they just move. Other than the turning rotor, wind turbines contain a high amount of other moving parts that are often causes of sound generation. Amongst them are the gearbox, the generator, the pivoting mechanism that turns the turbine against the wind, the blade pitch control mechanism, cooling fans, all or at least some of which are found in all turbines and produce different ranges of sound varying in both intensity and tone.

There are also several aerodynamic causes of sound in wind turbines, produced both by static and dynamic conditions. The tower and other structural elements are static sound producers but may influence the sound generation by dynamically interacting with other parts. In the case of downwind turbines (in which the blades are behind the tower in relation to wind direction) the turbulent flutter produced by the tower interacts with the passing blades in a region where flow is disturbed and causes a significant noise increase. But in general aerodynamic broadband noise (covering a large frequency spectrum) is regarded as the largest sound generator in wind turbines (Rogers and Manwell 2004).

To study the different aerodynamic causes (Wagner et al. 1996) splits sound generation in three different categories:

Low frequency noise

Is the noise characterized by the downwind or upwind blade/tower wake interaction. When wind rushes at certain velocities through the tower it separates from the boundary layer and creates a turbulent wake behind it which causes a dynamic pressure change. When the blade of the turbine goes through this wake a rapid change in blade loading occurs. These forces, acting from a surface onto the air, are source of dipole type loading noise (noise source polarity and type shall be addressed in Chapter 3). Since they are closely related to the passing of the blades through the wake, the sound spectrum produced is dominated by the frequency of their interaction and its harmonics, meaning blade number and blade rotational speed, often yielding values of just 1–3 Hz, hence the term low frequency noise. This noise, however, is reduced sharply by putting the rotor in front of the tower—in an upwind configuration.

Inflow–turbulence noise

This noise is caused by atmospheric turbulence incoming through the rotor area and interacting with the blade's aerodynamics. It can be of two natures; low frequency where the turbulence eddies are of much larger than the blade chord which produces a fluctuation of the total blade loading and again causes noise radiation of dipole type with a frequency of around 5 Hz with intensity varying in the order of Ma^6 where Ma denotes the Mach number. And high frequency noise which is related to eddy size close to or smaller than the blade chord. This form is product of complicated interactions in the aerodynamics of the blade, and not the global aerodynamic force like in the previous case. The result is sound at a much higher frequency and an intensity that varies in the order of Ma^5 .

Airfoil self–noise

This kind of noise is expected as a normal occurrence of blade aerodynamic properties. It can be generated in a number of different aerodynamic sections through different reasons caused by the behaviour of the fluid along and across the blade. Amongst these are:

- Trailing edge noise which happens when the flow is separated from the trailing edge surface and turbulence beneath the boundary layer induces a fluctuating pressure field. This type of noise is what will be researched in detail in this thesis, including why it's produced and how it could be dampened.
- Laminar-boundary-layer-vortex-shredding noise which happens when blades operate at a Reynolds² number at around $10^5 < Re < 10^6$ and laminar flow can join at the trailing edge from both the upper and lower side of the blade. This may cause an unstable interaction of the trailing edge noise and an unstable laminar flow transition. The upstream travelling acoustic wave couples to Tollmien-Schlichting instabilities³ resulting in tonal noise. This condition is of importance almost only in small or medium sized turbines that actually operate in this Reynolds region. If this is the case and if this phenomenon is seen to occur, it is often solved by tipping the boundary layer separation point to the front of the blade.
- Tip noise is a mechanism that is yet to be fully understood and is believed to be caused by a similar aerodynamic interaction as trailing edge noise. It is of broadband character and believed to be influenced by the convection speed of the vortex produced by the tip and its spanwise extent. Measures to reduce its effects have been carried out by trying out different blade tip geometries.

²See A.1 for the definition of the Reynolds number

³Tollmien-Schlichting instabilities refers to a disturbance wave created by perturbed laminar flow that grows in amplitude due to destabilizing effects of the no-slip condition at the boundaries and viscous effects of the fluid.

- Separated or stalled flow noise happens when increased angles of attack stall conditions occur causing the presence of unsteady flow around the airfoil. It is also of a broadband nature and can easily be reduced by avoiding stall conditions through proper angle of attack control.
- Blunt trailing edge noise is caused by eddies shedding from the blunt trailing edges of blades that are designed this way. Noise can be increased up to 360% from a square blunt trailing edge case and down to below 1% depending on different shapes used.
- Noise can also be produced by imperfections in the blade surface caused by dirt, dead insects, damage or mechanism related slits that produce perturbations in the air flow causing eddies and other disturbances that generate sound.

A study was conducted in (Oerlemans and Méndez-López 2005) by setting an array of microphones at a certain distance from a wind turbine to identify, in a working setting, which areas of the turbine are generating sound. The measurements were conducted on a GAMESA G58 wind turbine model and a graphic showing the results for different frequencies can be seen in Figure 1.4. A summary of the conclusions is presented below:

- The blades are the dominant source of aerodynamic noise in this model.
- Noise was mainly emitted on the downward motion of the blades.
- Blade noise is produced with greater intensity on the outer part of the blade but not at the very tip.
- Noise scales with the 5th power of the air flow⁴
- The noise observed is of broadband type and studies were made on ranges from 300 to 5000 Hz.
- The study suggests that there are two main mechanisms for noise generation: inflow-turbulent noise from incoming atmospheric turbulence and its interaction with the leading edge, and trailing edge generated noise, and out of both trailing edge is considered to be the larger source.

This research shall be given more prominence in section 4.5.

⁴Note that this is the same order of magnitude predicted by (Wagner et al. 1996) for inflow-turbulent noise of small scale eddies and in (Oerlemans and Méndez-López 2005) it is assumed that it also relates to trailing edge generated noise.

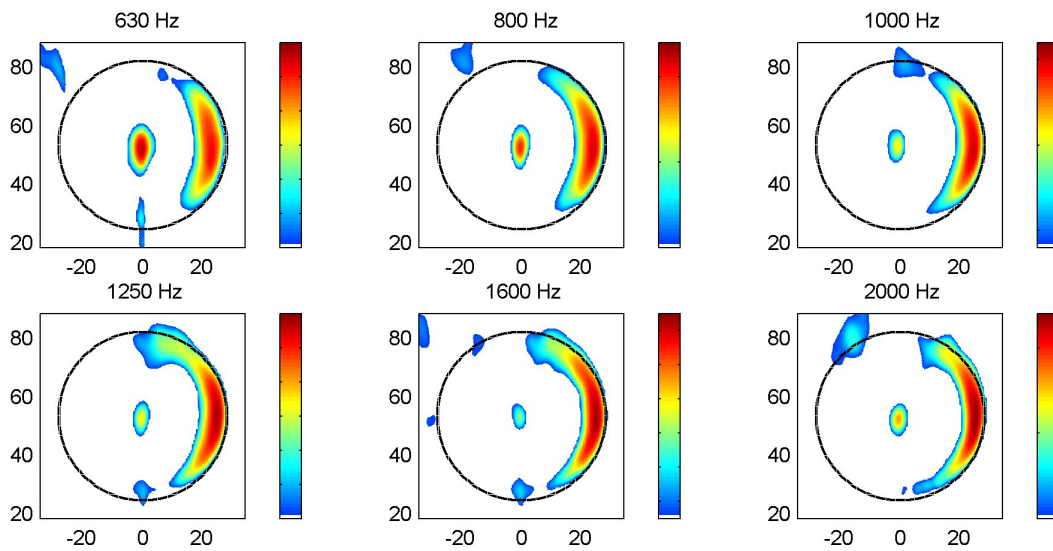


Figure 1.4: Measurements of noise in different areas of a GAMESA G58 wind turbine rotor and hub. Range of colour scale is 12 dB and the blade tip path is shown by the black circumference turning clockwise. (Oerlemans and Méndez-López 2005)

NUMERICAL METHODS IN COMPUTATIONAL FLUID DYNAMICS

Without going deep into the vast theory of fluid dynamics, a general overview shall be given on the important considerations of turbulence modelling that shall be of use in the rest of this work and are used as basis for most notable research in aeroacoustics or themselves applied in the modelling that was undertaken to pursue the objectives of this thesis.

As it will be outlined here and emphasized again in following chapters, the search for solutions in the branch of fluid dynamics is highly complicated by the non-linearity of the equations involved. These equations, called the Navier-Stokes equations, represent the cornerstone of fluid dynamics and by themselves are capable of modelling fluid behaviour, handling as a velocity field. This latter fact is important in that they are adhered to an Eulerian representation of fluid motion, compared to a Lagrangian representation which would instead concern itself in representing the *position* of the individual particles that would form the fluid.

Their importance in physics is immeasurable and their span of action goes beyond classic fluid problems. With adequate manipulation of their terms they can be extended to cases such as crowd dynamics or traffic modelling, the dynamics of stars inside a galaxy, and, coupled with Maxwell's equations, they can be used to study magnetohydrodynamics. In mathematics they represent a challenge in themselves as it is not yet known if in three dimensions solutions do or don't exist and, if in case they do, should they contain any singularities. This is called the Navier-Stokes existence and smoothness problems and are considered one of the few most important open problems in mathematics.

Convective acceleration of fluids is the physical reason behind their mathematical non-linearity and turbulence is the foremost example of its presence. Horace Lamb has been attributed to having once said

“I am an old man now, and when I die and go to heaven there are two matters on which I hope for enlightenment. One is quantum electrodynamics, and the other is the turbulent motion of fluids. And about the former I am rather optimistic.”

A chaotic system by definition, turbulence is the quintessential problem in fluid dynamics. The analytical solution of a problem which will become turbulent is impossible to find simply because there are no solutions to the system of partial differential equations (PDE's) that are the Navier-Stokes equations. Non the less, great advancement has been made since more than a century ago, most notably by Osborne Reynolds, Joseph Valentin Boussinesq, Ludwig Prandtl, Theodore von Kármán and Andrey Kolmogorov, amongst others who have pointed mainly to the use of statistical models, the description of the turbulent eddy viscosity, the mixing length concept and the similarity principle. A canvas of newly proposed concepts and models that has been knit into a complex fabric that allows for the approximation of how turbulence shall behave, but we know that an approximation is all we will ever achieve.

The advent of fast calculation power with the computer age has allowed scientists to finally approach these unresolvable equations in a way that translates them into solvable discretized systems. The derivatives encountered are then approximated by differential methods in a discrete numerical domain that represents the physical system. A great deal of effort is put into evaluating the correctness of this analogy and there is a very harsh trade off between the accuracy that's achieved and the amount of calculations one needs to achieve it.

In the field of aeroacoustics, as it will be discussed more deeply in following chapters, turbulence is of special importance since it's attributed as one of the main sources of sound in a flow. Later an overview of the theory behind aeroacoustics will be given and several methods of computational modelling of turbulence shall be mentioned, therefore a background of the most important and common ones shall be outlined next.

2.1 The Navier-Stokes Equations

All fluid motion can be described by the Navier-Stokes equations and in turn they are developed from basic physical principles. They assume that a fluid can be represented as a continuum instead of being composed of discrete particles. This can be conceived to be true if the relative size of such particles is very small compared to the scale of the fluid itself and in this way one could consider water molecules moving in a litre of water a continuum as much as a large container of marbles or even stars in a galaxy, all within a certain amount of accuracy.

The basic principles from which they are derived are the conservation of mass, energy and momentum, concepts which call for the need to consider a finite arbitrary sub-volume inside the general fluid volume and which is called a control volume.

To apply these conservation principles the Reynolds transport theorem must first be defined. Consider a control volume which moves with the fluid in such a way that it contains the same particles all the time. Call this volume Ω and its boundary, which is arbitrary in shape, $\partial\Omega$. The Reynolds transport theorem states that the sum of the changes in a certain property inside Ω , say for example pressure or density, will be equal to what is transferred through $\partial\Omega$ plus what is changed inside Ω due to sources or sinks. This principle is expressed by

$$\frac{d}{dt} \int_{\Omega} L dV = - \int_{\partial\Omega} L \mathbf{u} \cdot \mathbf{n} dA - \int_{\Omega} S dV$$

where L is the property of the fluid which is desired to be represented, \mathbf{u} is the velocity of the fluid, \mathbf{n} is the normal vector on $\partial\Omega$, S are the sources and sinks in Ω , and dA and dV are infinitesimal parts of the surface and the volume, respectively. By applying the divergence theorem on the surface integral it can be combined with the volume integral such that

$$\frac{d}{dt} \int_{\Omega} L dV = - \int_{\Omega} (\nabla \cdot (L \mathbf{u}) + S) dV$$

which, by applying Leibniz's rule,

$$\frac{d}{dx} \int_a^b F(x, y) dy = \int_a^b \frac{\partial F(x, y)}{\partial x} dy$$

becomes

$$\int_{\Omega} \left(\frac{\partial L}{\partial t} + \nabla \cdot (L \mathbf{u}) + S \right) dV = 0 \quad (2.1)$$

which is the mathematical representation of the Reynolds transport theorem.

One can now apply this condition to the conservation of momentum, writing it as $\rho \mathbf{u}$ such that, relating it to (2.1), if $L = \rho \mathbf{u}$, then the following must be true,

$$\frac{\partial}{\partial t} (\rho \mathbf{u}) + \nabla \cdot (\rho \mathbf{v} \mathbf{v}) + S = 0$$

where $\mathbf{v} \mathbf{v} = \mathbf{u} \otimes \mathbf{u}$ is a dyad such that for $\mathbf{u} = (u_1, u_2, u_3)$,

$$\mathbf{u} \otimes \mathbf{u} = \begin{pmatrix} u_1^2 & u_1 u_2 & u_1 u_3 \\ u_2 u_1 & u_2^2 & u_2 u_3 \\ u_3 u_1 & u_3 u_2 & u_3^2 \end{pmatrix}$$

The previous expression can be rearranged to,

$$\mathbf{u} \left(\frac{\partial \rho}{\partial t} + \nabla \cdot (\rho \mathbf{u}) \right) + \rho \left(\frac{\partial \mathbf{u}}{\partial t} + \mathbf{u} \cdot \nabla \mathbf{u} \right) = S$$

where S , still representing sources and sinks in the control volume, will represent body forces in this momentum case and thus shall be represented as \mathbf{F} .

Here the conservation of mass pops up in the lefter most term and, since no source terms in S are expected to generate mass or destroy it in our considerations, it can be considered to be zero. This leads to what is called the continuity equation,

$$\frac{\partial \rho}{\partial t} + \nabla \cdot (\rho \mathbf{u}) = 0 \quad (2.2)$$

Coming back to the momentum expression and considering the continuity equation as defined in (2.2), one now obtains the representation of conservation of momentum as

$$\rho \left(\frac{\partial \mathbf{u}}{\partial t} + \mathbf{u} \cdot \nabla \mathbf{u} \right) = \mathbf{F} \quad (2.3)$$

which can also be expressed as

$$\rho \frac{D\mathbf{u}}{Dt} = \mathbf{F}$$

having the convective derivative defined as

$$\frac{D}{Dt} = \frac{\partial}{\partial t} + \mathbf{u} \cdot \nabla \quad (2.4)$$

The body forces, \mathbf{F} , can be split up into stress forces and external forces and thus (2.3) can be represented by what's known as the Cauchy momentum equation,

$$\rho \frac{D\mathbf{u}}{Dt} = \nabla \cdot \boldsymbol{\sigma} + \mathbf{f}$$

where $\boldsymbol{\sigma}$ is known as the stress tensor,

$$\sigma_{ij} = \begin{pmatrix} \sigma_{11} & \tau_{12} & \tau_{13} \\ \tau_{21} & \sigma_{22} & \tau_{23} \\ \tau_{31} & \tau_{32} & \sigma_{33} \end{pmatrix}$$

in which the σ components represent the normal stresses and the τ components the shear stresses. The pressure is contained in the normal stresses and thus is separated for clarity reasons. By doing this, the tensor can now be written as

$$\sigma_{ij} = -pI + \mathbf{T}$$

where

$$\mathbf{T} = \begin{pmatrix} \sigma_{11} + p & \tau_{12} & \tau_{13} \\ \tau_{21} & \sigma_{22} + p & \tau_{23} \\ \tau_{31} & \tau_{32} & \sigma_{33} + p \end{pmatrix}$$

is the deviatoric stress tensor and I is the identity matrix. This permits the writing of (2.3) in a more complete form as

$$\rho \frac{D\mathbf{u}}{Dt} = -\nabla p + \nabla \cdot \mathbf{T} + \mathbf{f}$$

but where \mathbf{T} has still not been completely defined and its form actually depends on the type of fluid one is encountered with. For example, in the case of a Newtonian fluid for which

$$\tau \propto \frac{\partial u}{\partial x_2}$$

such that the shear stress is proportional to the velocity gradient perpendicular to the direction of shear, the deviatoric tensor is defined in its Einstein notation form as

$$\mathbf{T}_{ij} = \mu \left(\frac{\partial u_i}{\partial x_j} + \frac{\partial u_j}{\partial x_i} \right) + \delta_{ij} \lambda \nabla \cdot \mathbf{u}$$

where μ is the coefficient of viscosity and λ is related to the bulk viscosity of the fluid and is usually approximated as $\lambda \approx -2\mu/3$ (Batchelor 2000), while δ_{ij} is the Kronecker delta function.

So far the equations obtained are the continuity equation

$$\frac{\partial \rho}{\partial t} + \nabla \cdot (\rho \mathbf{u}) = 0 \quad (2.5)$$

and the conservation of momentum equation

$$\rho \frac{D\mathbf{u}}{Dt} = -\nabla p + \nabla \cdot \mathbf{T} + \mathbf{f} \quad (2.6)$$

Here equation (2.6) is a vector equation of three components and with equation (2.5) one sums up four equations but amongst them they contain five unknowns, namely the three components of \mathbf{u} , the density and pressure, so an additional equation must be formulated to have a closed system. This equation comes from the energy considerations which are very dependant on the kind of problem being approached. If one considers again a Newtonian fluid and applies the ideal gas law, the conservation of energy will yield

$$\rho \frac{Dh}{Dt} = \frac{D\rho}{Dt} + \nabla \cdot (k \nabla T) + \Phi \quad (2.7)$$

where h is the enthalpy of the system, T is the temperature, k is the Boltzmann constant, all of which are defined by an appropriate equation of state, and Φ is a function that represents the dissipation of energy due to viscous effects. Hereby (2.7) can be used as the 5th equation to fulfil the completeness of a 5 variable system.

So, the Navier-Stokes equations are composed of equations (2.5), (2.6) and (2.7) (in case of an ideal gas law abiding Newtonian fluid). It is very common to simplify them by considering incompressible fluids such that $\nabla \cdot \mathbf{u} = 0$, a condition that approximates fluids such as water and low Mach number air flow. This simplification transforms equation (2.6) into

$$\rho \left(\frac{\partial \mathbf{u}}{\partial t} + \mathbf{u} \cdot \nabla \mathbf{u} \right) = -\nabla p + \mu \nabla^2 \mathbf{u} + \mathbf{f} \quad (2.8)$$

and equation (2.5) to

$$\rho \nabla \cdot \mathbf{u} = 0 \quad (2.9)$$

where the term $\mathbf{u} \cdot \nabla \mathbf{u}$ (encountered in both incompressible and compressible form) is of particular importance since it represents the convective acceleration that was mentioned before. The term $\partial \mathbf{u} / \partial t$ represents the unsteady acceleration of the fluid and these two, multiplied by ρ , as found in equation (2.6), represent the inertia of the fluid in the control volume. On the right hand side of this same equation, $-\nabla p$ is the pressure gradients, $\nabla \cdot \mathbf{T}$ the internal forces in the fluid encountered due to viscous effects, and finally \mathbf{f} any other forces encountered such as gravity or centrifugal force exerted over the system.

2.2 Turbulence

A great deal can be said and has been written about turbulence yet it remains one of physics' most troubling problems and one of nature's most common phenomenons, especially if one considers the effect it has on our day to day activities. It can be characterized by the following properties as described in (Ferziger, Peric and Morton 1999):

- Turbulence is highly unsteady and the motion of particles in a turbulent flow will seem random,
- it is three dimensional,
- it contains a great deal of vorticity,
- it increases the rate at which conserved quantities are stirred,
- fluids of differing momentum content are brought by it into contact, therefore reducing the velocity gradient due to the action of viscosity and in turn reducing the kinetic energy of the flow as well. The lost energy is converted into internal energy and follows thermodynamic law,
- it contains coherent structures, being these repeatable and essentially deterministic events, yet the random component of turbulent flows causes any such events to differ greatly from each other in essential ways, thus making any assumptions and progress in their study very difficult,
- it fluctuates on a broad range of length and time scales, being this a great setback when attempting direct numerical simulation of them.

Some characteristics of a turbulent flow are relatively easily obtained from experimental studies, yet, as technology and optimization requirements advance, more detailed knowledge over more variables is needed in the general behaviour of a flow, thus calling for the better description of a turbulent flow's behaviour. In (Bardina, Ferziger and Reynolds 1980) a classification is made on the different approaches that can be taken to study such a flow:

- By using correlations such as ones that give the friction factor as a function of the Reynolds number or the Nusselt number of heat transfer as a function of the Reynolds and Prandtl numbers. This approach is limited to just a number of simple flow cases.
- By using integral equations derived from the equations of motion and thus reducing the problem to just one or more ordinary differential equations. This is limited to ordinary differential equations.

- By using direct numerical simulation in which case no approximations or models are used other than applying the bare Navier-Stokes equations on all the motions of the turbulent fluid. They will be explained in section 2.3.
- By using large eddy simulation in which the largest scale motions of the flow are solved while the smaller scales are just modelled or approximated. This method will be treated in section 2.4.
- By averaging the equations of motion over time in a statistically steady flow. This is called one-point closure and leads to the Reynolds averaged Navier-Stokes equations which will be explained in section 2.5.
- By using two-point closure methods in which equations for the correlation of the velocity components at two spatial points. The Fourier transform of these equations can also be used.

Despite the fact that much more can be said about turbulence, the objective remains to outline the different computational models that can be used to simulate it and will be encountered in the next chapters.

2.3 Direct Numerical Simulation

The most complete computational simulation of a flow comes from the direct numerical simulation approach (DNS). By undertaking the problem using this method, it is modelled at every point in the discretized space fully by the Navier-Stokes equations and thus no turbulence models or approximations are applied. This requires even the smallest scales in turbulent flow, called Kolmogorov scales, to be resolved. Based on this, (Ferziger et al. 1999) cites that the number of grid points then needed to perform such a simulation must be of at least L/η in *each* direction. Here L is the turbulence integral length scale¹ and η refers to the Kolmogorov scale, but this ratio has been found to be proportional to $Re_L^{3/4}$ for Re_L a Reynolds number based on the magnitude of the velocity fluctuations and the integral scale. Furthermore the time step used in the simulation is related to the grid size and, because the number of points must be employed in each of the three directions, the cost of a simulation scales as Re_L^3 .

Considering that Reynolds numbers of $Re = 10^6$ are commonly found, one can see that the computational expense of this method goes beyond what we're practically capable of providing. So far the record holder in a DNS study used 4096^3 mesh points and was carried out by the Japanese Earth Simulator in a 16.4 TFLOPS (trillion floating-point calculations per second) supercomputer. To put things into perspective this means that over 68×10^9 mesh points were used to simulate a flow with $Re_\lambda = 1217$ where Re_λ is the so-called Taylor-scale Reynolds number and $Re_\lambda \propto Re^{1/2}$, the integral scale was $L = 1.21$ and the Kolmogorov scale $\eta = 0.00053$ for a time step of $\Delta t = 2.5 \times 10^{-4}$ until $t \approx 5T$ for $T = L/U$ where U is the characteristic velocity of energy containing eddies. To conduct this simulation a memory capacity of 7.2 terabytes was required and a time of $30.7 \cdot s$ was estimated to be needed for each time step to be completed (Yokokawa, Ken'ichi Itakura, Ishihara and Kaneda 2002).

Having put the computational expense of DNS in perspective, it's important to note that, although it may not be possible to use it for everyday simulations, it is definitely not a useless method. Simulations such as the one performed in the Earth Simulator are important to study the validity of lighter but less accurate methods such as the ones that will be described next. Results

¹The integral scale L is the distance over which the fluctuating component of the velocity remains correlated, and thus can be regarded as the length scale opposite to the Kolmogorov scale which deals instead with the smallest scales on which viscosity is active.

from DNS can then be used to fine-tune and verify their applicability in order to wage where their weaknesses and advantages are. In addition, there are scientifically valuable cases which can be simulated in such low Reynolds numbers and limited domain size scenarios. These include the interest of understanding the very fine resolution mechanisms of turbulence production, energy transfer and dissipation in turbulent flows, studying drag on a solid surface, studying turbulence in compressible environments and, most importantly for this thesis, the production of aerodynamic noise. In this case one can only limit the numerical simulation to small cases of simple geometries and low Reynolds number flow, yet again its results will have valuable insight when studying other, more permissive methods, which can then be scaled to more complex settings.

2.4 Large Eddy Simulation

In large eddy simulations (LES) one looks to model a turbulent flow by filtering out values of quantities that are below a defined threshold. The idea behind this is that the small scale eddies don't carry enough energy to effectively transport conserved properties and thus can be neglected to a certain extent without harming the solution on the fluid's general behaviour too much. It is critical then to properly select the threshold which, in turn, could be different for different cases that are wished to be modelled. By doing this the computational requirements can be greatly minimized in comparison to DNS making this method much more feasible for use on more complex problems and lighter machines.

The process of separating the properties' values below which they will be approximated instead of directly simulated involves the filtering of these properties. This is done by equations of the following type, written as an example for the one-dimensional velocity field,

$$\bar{u}_i(x) = \int G(x, x') u_i(x') dx'$$

where u_i represents the one dimensional velocity field, $G(x, x')$ is called the filter kernel and can be composed of a Gaussian, a box or a cut-off filter to which a length scale, Δ , is associated and represents the desired threshold. Below this threshold the eddies are just modelled or approximated and not explicitly solved. The three-dimensional filtering is directly generalized from this one-dimensional example.

As a more explicit example, found in (Ferziger et al. 1999), the incompressible flow Navier-Stokes equations in their filtered form can be expressed as

$$\rho \left(\frac{\partial \bar{\mathbf{u}}}{\partial t} + \nabla \bar{\mathbf{u}} \bar{\mathbf{u}} \right) = -\nabla \bar{p} + \mu \nabla^2 \bar{\mathbf{u}} + \mathbf{f}$$

with the continuity equation unchanged (due to its linearity)

$$\rho \nabla \bar{\mathbf{u}} = 0$$

These equations can be compared with (2.8) and (2.9).

There is an added difficulty in finding the solution of the term $\overline{u_i u_j}$. It must be noted that $\overline{u_i u_j} \neq \bar{u}_i \bar{u}_j$ and thus, to aid in its evaluation, a modelling approximation is then introduced as the difference between them, namely

$$R_{ij} = -\rho (\overline{u_i u_j} - \bar{u}_i \bar{u}_j)$$

where R_{ij} is called the subgrid-scale Reynolds stress tensor. The design of R_{ij} is one of the key aspects of LES's research and applicability. It is common to use the model proposed in (Smagorinsky 1963) and derivatives from it. The basic proposal by this model is to use

$$R_{ij} = -2\nu_T \bar{S}_{ij} \tag{2.10}$$

where

$$\bar{S}_{ij} = \frac{1}{2} \left(\frac{\partial \bar{u}_i}{\partial x_j} + \frac{\partial \bar{u}_j}{\partial x_i} \right)$$

and ν_T is the eddy viscosity and is calculated as

$$\nu_T = (C_S \Delta_g)^2 \sqrt{2 \bar{S}_{ij} \bar{S}_{ij}}$$

where Δ_g is the grid size and C_S is a constant that could be calculated through empirical experiments of similar flows of those being modelled or by being dynamically calculated as a function of space and time.

Although LES is much less expensive than DNS, it still poses an important challenge in computational requirements, especially for simulating larger domains such as those commonly encountered in aerospace, car design or wind turbine modelling. In order to take advantage of this technology a trend of using hybrid methods has become popular in which regions of critical accuracy in a simulation are modelled using LES and then they are immersed in larger regions of lesser complexity to which other less expensive methods are applied. Amongst these are the Reynolds averaged Navier-Stokes equations family of models which will be addressed in the next section.

2.5 Reynolds Averaged Navier-Stokes Models

The idea behind Reynolds averaged Navier-Stokes models (RANS) lies behind the fact that the previous models may solve parameters that are not needed in a particular research or with much higher accuracy than required. The obvious penalty that is paid is a far greater computational expense than what is really needed and thus a more lighter method can be expected if one chooses to lose accuracy on those parameters which are not critical for the research objective.

This simplification of parameters is done through the averaging of their unsteadiness in the turbulent flow, causing the non-linearity of the Navier-Stokes equations to give rise to terms that must be modelled, like in the case of that was treated in the previous section for LES. The simplification of the flow begins by considering that it should be statistically steady over a time T which is large compared to the typical time scale of the fluctuations, and thus its variables can be written as a sum of a time-averaged value and a fluctuation around it,

$$\phi(x_i, t) = \bar{\phi}(x_i) + \phi'(x_i, t) \quad (2.11)$$

where

$$\bar{\phi}(x_i) = \lim_{T \rightarrow \infty} \frac{1}{T} \int_0^T \phi(x_i, t) dt$$

In case the flow is unsteady then ensemble averaging is used instead where

$$\bar{\phi}(x_i, t) = \lim_{N \rightarrow \infty} \frac{1}{N} \sum_{n=1}^N \phi(x_i, t)$$

where N is the number of members of the ensemble and should be large enough such that effects of the fluctuations are eliminated.

Considering now an incompressible Newtonian fluid such that equations (2.9) and (2.8) apply and shall be written in tensor notation

$$\begin{aligned} \frac{\partial u_i}{\partial x_i} &= 0 \\ \frac{\partial u_i}{\partial t} + u_j \frac{\partial u_i}{\partial x_j} &= -\frac{1}{\rho} \frac{\partial p}{\partial x_i} + \nu \frac{\partial^2 u_i}{\partial x_j \partial x_j} + f_i \end{aligned}$$

where $\nu = \mu/\rho$ is the kinematic viscosity. By taking the time-average of these equations one gets

$$\begin{aligned}\frac{\partial (\overline{u_i + u'_i})}{\partial x_i} &= 0 \\ \frac{\partial (\overline{u_i + u'_i})}{\partial t} + \overline{(\overline{u_j} + u'_j) \frac{\partial (\overline{u_i + u'_i})}{\partial x_j}} &= -\frac{1}{\rho} \frac{\partial (\overline{p} + p')}{\partial x_i} + \nu \frac{\partial^2 (\overline{u_i + u'_i})}{\partial x_j \partial x_j} + \overline{(f_i + f'_i)}\end{aligned}$$

but, since $\overline{\phi'} = 0$, the mean of a fluctuating variable is zero by definition, these can then be simplified to

$$\begin{aligned}\frac{\partial \overline{u_i}}{\partial x_i} &= 0 \\ \frac{\partial \overline{u_i}}{\partial t} + \overline{(\overline{u_j} + u'_j) \frac{\partial (\overline{u_i + u'_i})}{\partial x_j}} &= -\frac{1}{\rho} \frac{\partial \overline{p}}{\partial x_i} + \nu \frac{\partial^2 \overline{u_i}}{\partial x_j \partial x_j} + \overline{f_i}\end{aligned}$$

furthermore,

$$\overline{\overline{\psi}} = \overline{\psi}$$

and

$$\begin{aligned}\overline{\phi\psi} &= \overline{(\overline{\phi} + \phi') (\overline{\psi} + \psi')} \\ &= \overline{\overline{\psi}\phi + \overline{\psi}\phi' + \psi'\overline{\phi} + \psi'\phi'} \\ &= \overline{\phi\psi} + \overline{\phi'\psi'}\end{aligned}$$

thus the second term on the left hand side is rewritten and

$$\begin{aligned}\frac{\partial \overline{u_i}}{\partial x_i} &= 0 \\ \frac{\partial \overline{u_i}}{\partial t} + \overline{u_j} \frac{\partial \overline{u_i}}{\partial x_j} + \overline{u'_j} \frac{\partial \overline{u'_i}}{\partial x_j} &= -\frac{1}{\rho} \frac{\partial \overline{p}}{\partial x_i} + \nu \frac{\partial^2 \overline{u_i}}{\partial x_j \partial x_j} + \overline{f_i}\end{aligned}$$

Now, from the continuity equation,

$$\frac{\partial \overline{u_i}}{\partial x_i} = \frac{\partial \overline{u_i}}{\partial x_i} + \frac{\partial \overline{u'_i}}{\partial x_i} = 0$$

and, using the chain rule, one can make the following substitutions

$$\begin{aligned}\overline{u_j} \frac{\partial \overline{u_i}}{\partial x_j} &= \frac{\partial \overline{u_i} \overline{u_j}}{\partial x_j} - \overline{u_i} \frac{\partial \overline{u_j}}{\partial x_j} = \frac{\partial \overline{u_i} \overline{u_j}}{\partial x_j} + \overline{u_i} \frac{\partial \overline{u'_j}}{\partial x_j} = \frac{\partial \overline{u_i} \overline{u_j}}{\partial x_j} \\ \overline{u'_j} \frac{\partial \overline{u'_i}}{\partial x_j} &= \frac{\partial \overline{u'_i} \overline{u'_j}}{\partial x_j} - \overline{u'_i} \frac{\partial \overline{u'_j}}{\partial x_j} = \frac{\partial \overline{u'_i} \overline{u'_j}}{\partial x_j} + \overline{u'_i} \frac{\partial \overline{u_j}}{\partial x_j} = \frac{\partial \overline{u'_i} \overline{u'_j}}{\partial x_j}\end{aligned}$$

by again using the fact that the product of a mean quantity and a fluctuating quantity has zero mean. Now, the momentum equation can be written as

$$\frac{\partial \overline{u_i}}{\partial t} + \frac{\partial \overline{u_i} \overline{u_j}}{\partial x_j} + \frac{\partial \overline{u'_i} \overline{u'_j}}{\partial x_j} = -\frac{1}{\rho} \frac{\partial \overline{p}}{\partial x_i} + \nu \frac{\partial^2 \overline{u_i}}{\partial x_j \partial x_j} + \overline{f_i}$$

and, by introducing the mean rate of the viscous stress tensor (Wilcox 1998)

$$\overline{\tau}_{ij} = \mu \left(\frac{\partial \overline{u_i}}{\partial x_j} + \frac{\partial \overline{u_j}}{\partial x_i} \right)$$

the Navier-Stokes equations obtain the form²

$$\begin{aligned}\frac{\partial \bar{u}_i}{\partial x_i} &= 0 \\ \rho \frac{\partial \bar{u}_i}{\partial t} + \rho \frac{\partial \bar{u}_j \bar{u}_i}{\partial x_j} &= \frac{\partial}{\partial x_j} \left[-\bar{p} \delta_{ij} + \bar{\tau}_{ij} - \rho \overline{u'_i u'_j} \right] + \rho \bar{f}_i\end{aligned}$$

An expression has now been obtained for the time-averaged Navier-Stokes equations yet the introduction of the term $\rho \overline{u'_i u'_j}$, called the Reynolds stress, and other variables means that now there are more variables than equations to be solved and thus the system is not closed. The definition of these variables through approximations by prescribing them in terms of the mean quantities is the way to achieve closure and represent what's defined as the turbulence models (Ferziger et al. 1999).

The kinetic energy of the turbulent fluctuations is given as

$$\frac{1}{2} \overline{u'_i u'_i} = \frac{1}{2} \left(\overline{u'^2} + \overline{v'^2} + \overline{w'^2} \right)$$

which is related to the trace of the Reynolds stress tensor,

$$R_{ii} = -\rho \overline{u'_i u'_i}$$

and, by defining the *specific turbulence kinetic energy* (or just turbulence kinetic energy) as $k = \overline{u'_i u'_i} / 2$,

$$R_{ii} = -2\rho k$$

A transport equation for the turbulence kinetic energy is presented in (Wilcox 1998) as

$$\rho \frac{\partial k}{\partial t} + \rho \bar{u}_j \frac{\partial k}{\partial x_j} = R_{ij} \frac{\partial \bar{u}_i}{\partial x_j} - \rho \varepsilon + \frac{\partial}{\partial x_j} \left[\mu \frac{\partial k}{\partial x_j} - \frac{1}{2} \rho \overline{u'_i u'_i u'_j} - \overline{p' u'_j} \right]$$

where ε is called the *dissipation per unit mass* and is defined as

$$\varepsilon = \nu \overline{\frac{\partial u'_i}{\partial x_k} \frac{\partial u'_i}{\partial x_k}}$$

The previous equation is closely related to physical phenomena:

- The terms on the left hand side, namely the unsteady and convection term, comes from applying the convective derivative as defined in (2.4).
- The term $R_{ij} (\partial \bar{u}_i / \partial x_j)$ represents the rate at which kinetic energy is transferred from the mean flow to the turbulence.
- Dissipation refers to the rate at which turbulence kinetic energy is converted into thermal internal energy.
- Molecular diffusion, represented by the term $\mu (\partial k / \partial x_j)$, represents the diffusion of turbulence energy caused by the fluid's natural molecular transport process.
- The triple velocity correlation term is the turbulent transport, which is the rate at which turbulence energy is transported through the fluid by turbulent fluctuations.

²It should again be noted that Einstein notation is used such that repeated indices shall be summed over all their components.

- And the last term on the right hand side is the pressure diffusion, which comes from the correlation of pressure and velocity fluctuations and causes another form of turbulent transport.

The objective at this point is to seek closure on this equation by specifying R_{ij} , and the terms for dissipation, turbulent transport and pressure diffusion. For the Reynolds stress tensor it is assumed that the effect of turbulence can be represented as an increased viscosity, which leads to the eddy-viscosity model

$$R_{ij} = 2\mu_T S_{ij} - \frac{2}{3}\rho k \delta_{ij}$$

where μ_T is the eddy viscosity about which more will be mentioned below. In the case of turbulent transport it is assumed from the molecular transport process that $-\overline{u'_j \phi'} \approx \mu_T (\partial \overline{\phi} / \partial x_j)$, known as the eddy-diffusion model for a scalar. From DNS results shown in (Mansour, Kim and Moin 2006) it is further assumed that

$$\frac{1}{2} \overline{\rho u'_i u'_i u'_j} + \overline{p' u'_j} = -\frac{\mu_T}{\sigma_k} \frac{\partial k}{\partial x_j}$$

for σ_k a closure coefficient.

Dissipation and turbulent length scale, L , can be assumed to be strictly functions of the turbulence and independent of natural fluid properties, then

$$\varepsilon \approx k^{3/2} / L$$

for which various methods can be used to prescribe L .

Using these assumptions (Wilcox 1998) gives the modelled version of the turbulence kinetic energy equation as

$$\rho \frac{\partial k}{\partial t} + \rho \bar{u}_j \frac{\partial k}{\partial x_j} = R_{ij} \frac{\partial \bar{u}_i}{\partial x_j} - \rho \varepsilon + \frac{\partial}{\partial x_j} \left[\left(\mu + \frac{\mu_T}{\sigma_k} \right) \frac{\partial k}{\partial x_j} \right] \quad (2.12)$$

which is used in most turbulence energy equation models.

Amongst these models is the k - ε model which describes the eddy viscosity as

$$\begin{aligned} \mu_T &= \rho C_\mu \sqrt{k} L \\ &= \rho C_\mu \frac{k^2}{\varepsilon} \end{aligned}$$

where C_μ is a dimensionless constant. In total this method contains five parameters whose values are usually given as

$$C_\mu = 0.04 \quad C_{\varepsilon 1} = 1.44 \quad C_{\varepsilon 2} = 1.92 \quad \sigma_k = 1.0 \quad \sigma_\varepsilon = 1.3$$

There exist a number of other models such as the k - ω , yet their use is omitted in this thesis and therefore the reader is encouraged to find more information on them and further details about k - ε in (Wilcox 1998) and (Ferziger et al. 1999).

AEROACOUSTICS

In (Ffowcs-Williams 1995), the author, one of the most important researchers in aeroacoustics, presents a timeline of this field’s development. Gaining strength in the 1950’s as a direct consequence of a pressing need to mitigate the sound produced by jet noise, it has helped turn air travel into an ever-growing business that is more in sync with modern society’s needs.

Until 1952, when L.J. Lighthill published his paper “On sound generated aerodynamically”, (Lighthill 1952), experimental methods and instruments had both proven inadequate to study and predict the sound generated from jet engines. Lighthill came forward to lay the mathematical ground work behind the theory of aeroacoustics by proposing that airflow, in the absence of resonators and boundaries, could be considered equivalent in its sound generating ability to a distribution of quadrupoles. An important and applicable consequence of his calculations was that these structures would generate noise that scales according to the 8th power of jet velocity, a milestone for research and development. His paper brought some very needed mathematical background and orientation to the complex problem of aeroacoustics and has come to become a landmark by proposing the quadrupole nature of aerodynamic sources and the convective effect and space-time structure of fluctuating Reynolds stresses.

An important extension to Lighthill’s acoustic analogy came in 1955 when Curle published his article “The influence of solid boundaries upon aerodynamic sound”, (Curle 1955). It introduced the effect of flow boundaries and showed that boundary terms can indeed provide effective mass and momentum injection into the main flow, which acoustically would be the same as having monopole and dipole sources that, to his regard, would have fundamentally greater acoustic efficiency than Lighthill’s quadrupole structures (an application of his theory is briefly covered in section 4.1). In this sense, the now regarded Lighthill/Curle approach, relates sound exactly to integrals of volume *and* surface source terms. In addition it also specifies precisely what these source terms are and, as a consequence of knowing them, sheds light on the sound field itself.

It was so until Alan Powell’s 1960 paper “Aerodynamic noise and the plane boundary”, (Powell 1960), made note of the fact that the interrelation between source and sound was seen to be unacceptably codependent. The reason behind this is that the surface source terms could actually not be specified independently of sound in a general sense since sound itself might in turn create a disturbance in the source—failing a need in aeroacoustics that the sound and source be separated and the sound be defined purely as a linear response to the source’s environment. Powell realized this when he noticed that the turbulence bounded by a rigid plane would actually generate only quadrupoles and that Curle’s surface sources were just a specular reflection of the volumetric sources, making his predictions valid only when the surfaces are acoustically compact and of linear scale much smaller than any in the sound field. Non the less, Curle’s researched has introduced these monopole and dipole sources which effectively yield U^4 and U^6 scaling laws, in much the same way that Lighthill’s quadrupoles introduced the U^8 law.

It was this eighth power law relating noise and jet speed that had a very important role in the design and manufacturing of jet turbines until today. The need to reduce jet speed was emphasized if one wished to reduce the noise made by it and as a consequence companies started making higher mass flow engines with lower specific thrust—an additional advantage was that propulsive efficiency also was expected to improve by achieving this goal. Change proved not to come with a hasted solution to the problem since the modified designs now parted from the quadrupole scaling predictions. Instead more efficient acoustic sources which were much less sensitive to jet speed came now into prominence. Effects from turbulence, behaving as an axial dipole, that generated in the jet stream because of a number of factors forced the U^6 scale law to be considered. Furthermore unsteady exhaust output is equivalent to an acoustic monopole and thus a U^4 scale law was also observed.



Figure 3.1: Picture of a Rolls-Royce Trent 1000 jet engine used in the Boeing 787 model, retrofitted with serrations, called *chevrons*, in the posterior side of the pod (Image source: http://en.wikipedia.org/wiki/File:Boeing_787_engine_chevrons.jpg. Author: Mark Handel)

Since then, jet engines have been fitted with flow smoothing devices and sound insulation in their frames to mitigate internal sources such as combustion effects, internal irregular flow and its own turbomachinery. These techniques have greatly reduced jet engine noise in the past four decades and in fact it has seized to be the dominant source when overall aircraft noise is considered near airports where the aircraft's aerodynamic frame itself, especially in landing configuration, represents a very important source of noise.

The application range of Lighthill's theory is bounded by cases where turbulence is the noise generator but is contained in an ideal atmosphere at rest, a sufficient condition for studying jet noise. But cases

that it cannot model, such as the aircraft frame noise, called for a very needed. Gustav Kirchhoff made such an attempt by enclosing the source region in a control surface, such that the sound field inside or outside this surface, where no sources are present, can be produced as a superposition of monopoles and dipoles on its surface. His theory descends from the wave equation and a non-zero flow velocity can be considered by setting a moving frame of reference with the outer flow speed. Unfortunately it encounters problems where nonlinear effects are present outside the integration surface such as when a wake crosses the surface in cases like those of noise radiated by a cylinder in uniform flow or transonic flow over a rotor blade (Crocker 1998).

In 1969 a paper by Ffowcs-Williams and Hawkins came to propose a similar approach to the problem but by deriving the theory straight from Lighthill's. Their method also proposed the use of a control surface around the source of noise to be able to account for them to have movement inside the atmospheric environment, and sources outside this surface can now be accounted by just adding an extra volume integral over quadrupole sources, just as in Lighthill's theory. This advancement was highly motivated by the research field of helicopter rotor noise done during that time and is now applicable to a very wide variety of cases. This theory will be explained with more detail in section 3.2.

3.1 The Lighthill Analogy

The key aspect about Lighthill's trend changing article, (Lighthill 1952), is a rearrangement of the Navier-Stokes equations into an inhomogeneous wave equation thereby connecting fluid theory and acoustic prediction. The derivation of his equation starts with Navier-Stokes' continuity equation

$$\frac{\partial \rho}{\partial t} + \frac{\partial}{\partial x_i} \rho u_i = 0 \quad (3.1)$$

and an approximation to the conservation of momentum equation

$$\frac{\partial}{\partial t} \rho u_i + c_0^2 \frac{\partial \rho}{\partial x_i} = 0 \quad (3.2)$$

where c_0 is the speed of sound, u_i is the velocity in the x_i direction, and ρ is the density. Then, by differentiating 3.1 with time and 3.2 with space,

$$\begin{aligned} \frac{\partial}{\partial t} \left[\frac{\partial \rho}{\partial t} + \frac{\partial}{\partial x_i} \rho u_i \right] &= \frac{\partial^2 \rho}{\partial t^2} + \frac{\partial^2}{\partial t \partial x_i} \rho u_i \\ \frac{\partial}{\partial x_i} \left[\frac{\partial}{\partial t} \rho u_i + c_0^2 \frac{\partial \rho}{\partial x_i} \right] &= \frac{\partial^2}{\partial t \partial x_i} \rho u_i + c_0^2 \frac{\partial^2 \rho}{\partial x_i^2} \end{aligned}$$

the momentum density term ρu_i can be subtracted from these equations by relating them to produce

$$\frac{\partial^2 \rho}{\partial t^2} - c_0^2 \frac{\partial^2 \rho}{\partial x_i^2} = 0 \quad (3.3)$$

Equation 3.2 in its exact, Reynolds form is written as

$$\frac{\partial}{\partial t} \rho u_i + \frac{\partial}{\partial x_j} (\rho u_i u_j + p_{ij}) = 0 \quad (3.4)$$

where Einstein summation convention is being used, and

$$p_{ij} = p \delta_{ij} + \mu \left[-\frac{\partial u_i}{\partial x_j} - \frac{\partial u_j}{\partial x_i} + \frac{2}{3} \left(\frac{\partial u_k}{\partial x_k} \delta_{ij} \right) \right]$$

is the stress tensor for a Stokesian gas. Here δ_{ij} is the Kroenecker delta such that if $i = j$, $\delta_{ij} = 1$ and if $i \neq j$ then $\delta_{ij} = 0$.

Defining

$$T_{ij} = \rho u_i u_j + p_{ij} - c_0^2 \rho \delta_{ij} \quad (3.5)$$

equation 3.4 can be rewritten as

$$\frac{\partial}{\partial t} \rho u_i + c_0^2 \frac{\partial \rho}{\partial x_i} = -\frac{\partial T_{ij}}{\partial x_j} \quad (3.6)$$

and then, by applying the same procedure as before to produce equation 3.3,

$$\frac{\partial^2 \rho}{\partial t^2} - c_0^2 \frac{\partial^2 \rho}{\partial x_i \partial x_j} = \frac{\partial^2 T_{ij}}{\partial x_i \partial x_j} \quad (3.7)$$

Equations 3.1, 3.6 and 3.7 represent the equations of the propagation of sound in a uniform medium at rest due to externally applied fluctuating stresses. Equation 3.7, a hyperbolic PDE, is

known as Lighthill's equation and is an inhomogeneous wave equation describing a wave moving at the speed of sound in a medium at rest.

The underlying analogy behind these equations is between the equations governing the fluctuations of density in a fluid and the equations dealing with a uniform acoustic medium at rest. A fluctuating external force acting on the acoustic medium represents the difference between these two sets of equations. T_{ij} is the representation of this external force and is in fact the difference between the effective stresses in the flow and the stresses in the acoustic medium as seen in equation 3.5. The completeness of this external stress system T_{ij} is so that it incorporates the generation of sound, the convection with the flow, its propagation with variable speed and the gradual dissipation by conduction, and dissipation by viscosity, represented by the terms $\rho u_i u_j$, the difference between the pressure variations and c_0^2 times the density variations and the viscous contribution to the stress system, p_{ij} , respectively. It can be further said that in commonly used length scales only the term $\rho u_i u_j$ presents meaningful contribution to T_{ij} .

Lighthill explains that sound produced by a concentrated fluctuating force is manifested in the form of a dipole of perturbations and, since the driving force behind the perturbations in the acoustic medium, T_{ij} , is a stress field, it represents instead a distribution of quadrupoles whose instantaneous strength per unit volume is proportional to the local stress.

The integral nature of Lighthill's analogy comes from that the integral of T_{ij} over the source region is the sound field outside this region. As noted in (Pedley 2001), in the far field (at a distance large compared to $1/2\pi$ times the wavelength of interest) this integral reduces to

$$\rho(\mathbf{x}) - \rho_0 \approx \frac{1}{4\pi c_0^4} \int \frac{(x_i - y_i)(x_j - y_j)}{|\mathbf{x} - \mathbf{y}|^3} \frac{\partial^2}{\partial t^2} T_{ij} \left[\mathbf{y}, t - \frac{|\mathbf{x} - \mathbf{y}|}{c_0} \right] dy \quad (3.8)$$

where \mathbf{x} is the acoustic observation point, \mathbf{y} is the source location, and t is the current observation time.

To find the intensity of the radiated sound, given by

$$I(\mathbf{x}) = \frac{c_0^3}{\rho_0} \overline{(\rho - \bar{\rho})^2(\mathbf{x}, t)}$$

where the notation \bar{a} represents the mean value of a variable a , one can look to the proportionality between the stream velocity U (correlated to a length-scale L) and the density fluctuation which is given by equations 3.7 and 3.8,

$$\rho - \rho_0 \propto \frac{1}{c_0^4} \frac{1}{R} \left(\frac{U}{L} \right)^2 \cdot \rho_0 U^2 L^3 = \rho_0 \left(\frac{U}{c_0} \right)^4 \frac{L}{R}$$

where R is the distance between the source and the receiver. This proportionality is come across by (Lighthill 1952) through taking $\partial^2 T_{ij} / \partial t^2 \propto (U/L)^2 \rho_0 U^2$. So, by writing this into the intensity equation, the landmark eight-power law equation arises:

$$I \propto \rho_0 \frac{U^8}{c_0^5} \left(\frac{L}{R} \right)^2 \quad (3.9)$$

Overall the work of Lighthill in his 1952 paper is a monumental contribution to aeroacoustics written with mathematical elegance whose complete derivation goes beyond the purpose of this thesis. Its contributions and meaning are not to be taken lightly and are expected to still ripple through the advancements we'll see in the future of this research field, much in the same way Ffowcs-Williams and Hawkings' own work will do.

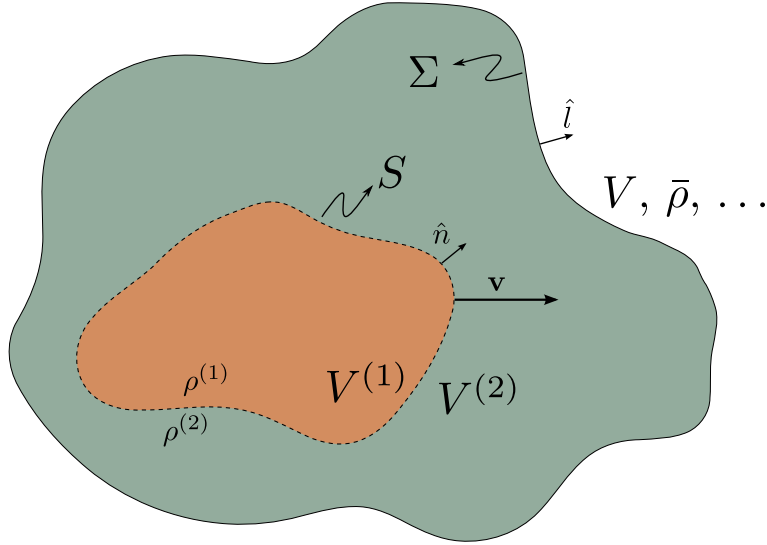


Figure 3.2: A representation of Ffowcs-Williams and Hawkings' surface approach.

3.2 The Ffowcs-Williams and Hawkings Analogy

In (Ffowcs-Williams and Hawkings 1969) it's noted that the equations used in (Lighthill 1952) are valid only in the region exterior to whatever closed surfaces may exist. The solution to this problem is approached by devising an unbounded volume V which is partitioned into regions by *mathematical* surfaces that may correspond to the real surfaces (see Figure 3.2). The key advantage in this is that motion on and outside these surfaces now coincides with the real fluid motion, and the motion in their interior can be specified arbitrarily. One way to see this approach is that now the original situation has been embedded in a more general one where movement by the surfaces is allowed. This extends Lighthill's theory to one that's applicable to cases such as helicopter rotor analysis, wing and blade analysis, turbomachinery, and any such other case where the noise source is in movement with respect to the surrounding fluid conditions.

For a case such as the one illustrated in Figure 3.2, where there exist two volumes, $V^{(1)}$ and $V^{(2)}$ such that $V = V^{(1)} \cup V^{(2)}$, separated by a surface S and where V is contained by a surface Σ , each of which has normals \hat{n} and \hat{l} respectively, the properties for each, for example density, will be designated as $\rho^{(1)}$ if it belongs to $V^{(1)}$ and $\rho^{(2)}$ if it belongs to $V^{(2)}$, and $\bar{\rho}$ if it belongs to the overall volume V . Furthermore, the surface S is allowed to move with velocity $\mathbf{v} = (v_1, v_2, v_3)$ in the space (x_1, x_2, x_3) . This way, the rate of change of the mass within V is given by

$$\frac{\partial}{\partial t} \int_V \bar{\rho} dV = \frac{\partial}{\partial t} \int_{V^{(1)}} \rho^{(1)} dV + \frac{\partial}{\partial t} \int_{V^{(2)}} \rho^{(2)} dV$$

where the rate of change of the mass within $V^{(1)}$ is

$$\frac{\partial}{\partial t} \int_{V^{(1)}} \rho^{(1)} dV = - \int_{\Sigma} (\rho u_i)^{(1)} l_i d\Sigma - \int_S [\rho (u_i - v_i)]^{(1)} n_i dS$$

for a fluid velocity of $\mathbf{u} = (u_1, u_2, u_3)$. Here the difference of mass leaving the surfaces S and Σ is just being subtracted from the volume with units of $[\text{kg}/\text{m}^2\text{s}]$. This expansion can also be applied to the rate of change of mass within $V^{(2)}$ and, by combining them, the overall rate of

change of mass is

$$\frac{\partial}{\partial t} \int_V \bar{\rho} dV = - \int_{\Sigma} (\bar{\rho} u_i) l_i d\Sigma + \int_S [\rho (u_i - v_i)]_{(1)}^{(2)} n_i dS$$

where $[a]_{(1)}^{(2)} = a^{(2)} - a^{(1)}$. Then, by applying the divergence theorem to the integral over the surface Σ the authors are able to convert it to a volume integral and relate it to the left hand side of the equation such that

$$\int_V \left[\frac{\partial \bar{\rho}}{\partial t} + \frac{\partial}{\partial x_i} (\bar{\rho} u_i) \right] dV = \int_S [\rho (u_i - v_i)]_{(1)}^{(2)} n_i dS$$

The next step is to convert the previous expression's right hand side also to a volume integral such that the generalized mass equation can be obtained. This is done by defining a function $f(\mathbf{x})$ such that

$$f(\mathbf{x}) \begin{cases} < 0 & \text{if } x \in V^{(1)} \\ = 0 & \text{if } x \in S \\ > 0 & \text{if } x \in V^{(2)} \end{cases}$$

and multiplying the integrand by

$$\delta(f) \left[\left(\frac{\partial f}{\partial x_j} \right)^2 \right]^{1/2}$$

where $\delta(f)$ is the Dirac delta¹. Furthermore, the derivative of f in terms of x_j taken in the direction n_i is related to the derivative in terms of x_i , such that

$$n_i \left[\left(\frac{\partial f}{\partial x_j} \right)^2 \right]^{1/2} = \frac{\partial f}{\partial x_i}$$

and thus, by plugging this into the last equation of rate of mass change and deriving by dV to remove the volume integrals,

$$\frac{\partial \bar{\rho}}{\partial t} + \frac{\partial}{\partial x_i} (\bar{\rho} u_i) = [\rho (u_i - v_i)]_{(1)}^{(2)} \delta(f) \frac{\partial f}{\partial x_i} \quad (3.10)$$

which is the generalized mass equation. Relate this equation to Navier–Stokes' continuity equation, (3.1), where the term $[\rho (u_i - v_i)]_{(1)}^{(2)} \delta(f) (\partial f / \partial x_i)$ now represents a shell distribution of mass sources (on the surface S) whose purpose is to maintain the unbounded fluid in its defined state.

Using the same methods the authors derive the generalized momentum equation,

$$\frac{\partial}{\partial t} (\bar{\rho} u_i) + \frac{\partial}{\partial x_j} (\bar{\rho} u_i u_j + \bar{p}_{ij}) = [p_{ij} + \rho (u_j - v_j)]_{(1)}^{(2)} \delta(f) \frac{\partial f}{\partial x_j} \quad (3.11)$$

To relate these equations to a real life applicable situation the following assumptions are made:

- In the region 1 the fluid is assumed to be at rest with density ρ_0 and pressure p_0 .
- The stress tensor p_{ij} has the same mean value $p_0 \delta_{ij}$ in both regions, such that it can be removed from where it appears in the right hand side of equation 3.11.

¹See Appendix A.3

- The interior condition is $p_{ij} = 0$.
- S is impermeable such that $u_n = v_n$

Having this, the equations become

$$\begin{cases} \frac{\partial \bar{\rho}}{\partial t} + \frac{\partial}{\partial x_i} (\bar{\rho} u_i) = \rho_0 v_i \delta(f) \frac{\partial f}{\partial x_i} \\ \frac{\partial}{\partial t} \bar{\rho} u_i + \frac{\partial}{\partial x_j} (\bar{\rho} u_i u_j + \bar{p}_{ij}) = p_{ij} \delta(f) \frac{\partial f}{\partial x_j} \end{cases} \quad (3.12)$$

where the superscript referring to volume 2 has been dropped. Of course the objective here, as it was in Lighthill's development, is to arrive at a wave equation governing the generation and propagation of sound, and, also as before, and using the same technique, this is achieved by removing the overall momentum term $\bar{\rho} u_i$ from equation 3.12, thus arriving at

$$\left(\frac{\partial^2}{\partial t^2} - c_0^2 \frac{\partial^2}{\partial x_i^2} \right) (\bar{\rho} - \rho_0) = \frac{\partial^2 \bar{T}_{ij}}{\partial x_i \partial x_j} - \frac{\partial}{\partial x_i} \left(p_{ij} \delta(f) \frac{\partial f}{\partial x_j} \right) + \frac{\partial}{\partial t} \left(\rho_0 v_i \delta(f) \frac{\partial f}{\partial x_i} \right) \quad (3.13)$$

Here the Lighthill stress tensor, T_{ij} , is zero within the surface S , and the generalized density perturbation $\bar{\rho} - \rho_0$ is a measure of the sound amplitude. This equation shows that sound can be regarded as generated by three source distributions:

- One of acoustic quadrupoles of strength density T_{ij} in the region outside the surface. This is identical to that described by Lighthill.
- A surface distribution of acoustic dipoles of strength density $p_{ij} n_j$ which is described in (Curle 1955).
- A surface distribution of monopole sources that arises when the surfaces are moving and represent a volume displacement effect.

The solution to equation 3.13 is non-trivial and its derivation goes beyond the purpose of this work. In Chapter 21 of (*Fluent 6.3, User's Guide* 2006) it is outlined that Fluent, the software that will later be used to solve the cases addressed in this thesis, uses a solution of the form

$$p'(\mathbf{x}, t) = p'_T(\mathbf{x}, t) + p'_L(\mathbf{x}, t)$$

where $p' = p - p_0$ and

$$4\pi p'_T(\mathbf{x}, t) = \int_{f=0} \left[\frac{\rho_0 (\dot{U}_n + U_{\dot{n}})}{r(1 - \text{Ma}_r^2)} \right] dS \\ + \int_{f=0} \left[\frac{\rho_0 U_n \{ r \text{Ma}_r + c_0 (\text{Ma}_r - M^2) \}}{r^2 (1 - \text{Ma}_r)^3} \right] dS$$

$$4\pi p'_L(\mathbf{x}, t) = \frac{1}{c_0} \int_{f=0} \left[\frac{\dot{L}_r}{r(1 - \text{Ma}_r)^2} \right] dS \\ + \int_{f=0} \left[\frac{L_r - L_M}{r^2 (1 - \text{Ma}_r)^2} \right] dS \\ + \frac{1}{c_0} \int_{f=0} \left[\frac{L_r \{ r \text{Ma}_r + c_0 (\text{Ma}_r - M^2) \}}{r^2 (1 - \text{Ma}_r)^3} \right] dS$$

where

$$\begin{aligned} U_i &= v_i + \frac{\rho}{\rho_0} (u_i - v_i) \\ L_i &= p_{ij} \hat{n}_j + \rho u_i (u_n - v_n) \\ \dot{U} &= \frac{\partial U}{\partial t} \end{aligned}$$

and r is the distance to the observer while Ma_r is the Mach number at which the source approaches the field point.

Physically p'_T corresponds to a concept called *thickness noise* which corresponds to the displacement of the fluid in the flow field by the sound source (a blade, for example). The term p'_L refers to the *loading noise* which is created by the accelerating force on the fluid generated by the moving surface. See (Brentner and Farassat 2003). The thickness term is related to the monopole sources and the loading term to the dipole sources described above. The additional term containing Lighthill's stress tensor in equation 3.13 represents the quadrupoles as seen in Lighthill's theory and which applies to the whole *exterior* volume. It can be thus observed that the Ffowcs-Williams and Hawkings equation is a general case of Lighthill's which includes physical surfaces in arbitrary motion represented by the thickness and loading terms.

It can be seen that this approach has problems when $\text{Ma}_r = 1$ which comes from the term $|1 - \text{Ma}_r|$ in the integrands, called the Doppler factor. But this singularity has been overcome numerically by applying a collapsing sphere formulation (Farassat and Brown 1977) or an emission-surface formulation (Brentner and Farassat 2003), thus allowing the analogy to now be applicable to cases with supersonic motion.

3.3 The Proudman/Lilley Approach

In (Proudman 1952) the author approaches Lighthill's theory from a perspective of noise generation by isotropic turbulence related structures in the flow. Its model considers an infinite volume at rest with a finite region of turbulent motion, assumed to be excited by some forcing function such that its initial characteristics are isotropic and are generated by a *very large* Reynolds number. His theory relies just on information concerning statistical properties of isotropic turbulence, including retarded-time and the space covariance of Lighthill's T_{ij} tensor.

Proudman reaches the conclusion that the generation of sound from turbulence is mainly a consequence of two kinds of eddies, those with scales in the dissipation range and those with them in the energy containing range. Of the two only the latter is foreseen to make a considerable contribution to sound at high values of the Reynolds number. Furthermore, he states that sound appears from the decay of the turbulence kinetic energy and from its instantaneous generation.

Proudman's theory is best applied to cases where the intensity of the turbulence is maintained constant in time and with a low Mach number such that retarded-time effects can be neglected. Both these conditions apply when one is dealing with a high Reynolds number so that, as mentioned above and given these flow characteristics, the eddy scale spectrum with scales in the energy containing range are expected to be prominent noise generators. The author finds that the total acoustic power radiated from the embedded finite region of turbulence is a function of the local time-averaged kinetic energy of the turbulence per unit volume, k , and the time averaged rate of dissipation of the kinetic energy per unit volume, ε .

Amongst the considerations taken in his theory are that the length scale of the turbulence, L , has to be very small compared with the typical dimension D , of the turbulent domain. It is argued that the distance needed for the covariance to fall to zero must also be small in order that edge effects from the boundaries to the turbulent domain will be relatively small. With this boundary layer, the turbulence intensity and vorticity are zero outside the region of

turbulent flow. Inside that boundary layer, though, turbulence is expected to have very different characteristics from the turbulence inside the central region of turbulent motion, including that it would be anisotropic. The definition of a small boundary layer in comparison to the rest of the region is that L/D be smaller than $1/100^{\text{th}}$ order of magnitude, a scale that may present accuracy problems in a numerical computation (Lilley 1994). Further constraints are that the Mach number of the turbulence must satisfy the condition $\text{Ma} \ll L/D \ll 1$.

In his theory Lilley describes the use of very low Mach numbers, $\text{Ma} \ll 0.01$, and warns of that special considerations must be taken into account if higher values are encountered. Fluent’s implementation of the Proudman/Lilley approach states a similar warning and, as it will be seen in depth in following chapters, the Mach number simulated in this work is usually one of $\text{Ma} = 0.15$, thus larger than the recommended, and effects of this difference will later be studied. As explained in (*Fluent 6.3, User’s Guide 2006*), Chapter 21, the acoustic power due to unit volume of isotropic turbulence as derived from the Proudman/Lilley theory yields

$$P_A = \alpha \rho_0 \left(\frac{u^3}{L} \right) \frac{u^5}{c_0^5}$$

which has units of $[\text{W}/\text{m}^3]$. Here u is the eddy velocity magnitude and L is its length scale, and c_0 the speed of sound. α is a model constant which has been calibrated from (Sarkar and Hussaini 1993) from direct numerical simulation (DNS) experiments. If the equation above is written in terms of k , the turbulence kinetic energy, and ε , the turbulence viscosity ratio, it becomes

$$P_A = \alpha_\varepsilon \rho_0 \varepsilon M_t^5 \quad (3.14)$$

where

$$M_t = \frac{\sqrt{2k}}{c_0}$$

and $\alpha_\varepsilon = 0.1$ is used by Fluent. A clear advantage seen in this method is that it can be run using a relatively inexpensive k - ε turbulence model as a steady state simulation since only statistical properties of the variables in equation 3.14 are needed. A more detailed view of requirements and chosen models will be presented in Chapters 5 and 6.

By the nature of the considerations needed to be made in aeroacoustic modelling, the expensive computational nature of the available approaches is by rule the chief concern. The Proudman/Lilley approach, though, presents itself as a promising option that doesn’t require the prohibiting nature of using DNS or LES, or the transient properties of the Ffowcs-Williams and Hawkings approach. The next section gives an overview of the problems that are typically encountered in computational aeroacoustics.

3.4 Computational Aeroacoustics and its Issues Regarding Computational Expense

As it was explained above, sound is nothing more than a fluctuation of pressure in a fluid. Its presence is captured by our auditory system and reproduced into electric signals which the brain recognizes as everything that we hear. The fluctuation that is generated by a source must be inside a certain frequency for us to recognize it as sound—although beyond those limits we could still be able to perceive it but in other ways, such as by cavity resonance inside our internal organs or skin perception of air movement due to the pressure changes. The audible spectrum of pressure fluctuations, though, involves very rapid and, in many cases, small changes in pressure

at a given point in space. This characteristic is the main culprit behind aeroacoustics being by nature an expensive research field, computationally speaking.

Generally speaking, computational fluid dynamics (CFD) itself is a field which only until relatively recently has seen an increment in viable usability thanks to the rapid increase in computer processing power and the advancement of the methods and models used. It is a field that requires the solution of a series of complex equations in multiple locations, known as nodes, in discrete space and by doing so try to approximate the continuum of a fluid. The larger the amount of nodes the better the approximation, but more calculations are needed; the lesser the amount of nodes the simulation becomes less expensive, but errors should be then expected to arise in the form of loss of information, smudging of values, and general numeric and round off errors which become more critical as nodes are placed further apart in areas of high aerodynamic interest. There is a sense of artistic property married to the scientific nature in the task of designing the placement of these discrete nodes, the meshing of the computational domain, one of the three big steps in a CFD simulation along with solving and post-processing the data.

Having said that, the resolution needed to approximate a CFD simulation dwarfs in comparison to that which is needed in the direct computational aeroacoustic (CAA) approach required to properly model those very quick and potentially small pressure fluctuations that are sound. Furthermore, it is agreed that a turbulent region is a generator of sound, which means that there is a pressing requirement that said area has to be well modelled. The problem that this fact brings up is not to be taken lightly, given that turbulence is the quintessential challenge for fluid dynamicists. Its chaotic nature and the presence of small energy carrying eddies that pose a butterfly effect to the whole domain and thus are hard to ignore without hesitation, call for the need of an extremely fine mesh in this area and the use of DNS or LES at best, means that the computation is prohibitively expensive and applicable only to a very limited number of case scenarios with narrow usefulness in an industrial level other than to be used to calibrate other methods.

Another great difference between CFD and direct computation CAA is that, while in the former the regions of interest can be limited to areas nearby structures and in their wake, in the latter the region of interest compromises the whole domain since acoustic waves remain quick and potentially of small intensity throughout all the region as they travel toward the receiver. Yet, not only is the path to the receiver important but also other lines of reflection between the source and itself since the waves are expected to bounce off any other structures that may be present in the model, for example the fuselage of an aircraft in the case where its aerodynamic surfaces' noise contributions are being studied in landing configuration and their effect is needed to be known for an observer on the ground.

Fortunately, as seen in previous sections, there has been a steady evolution of methods that emulate sound generation through analogies and statistical measures. These, coupled with existing turbulence models that take away the need to use DNS or LES, greatly relax the resolution requirements of the mesh. Non the less, there is still a great price that is paid in terms of loss of acoustic accuracy and the aforementioned approaches are still subject of undergoing research to improve them and make them attractive to a greater number of applications. The acoustic results that are available through them currently only give a rough approximation to real case data and can only be expected to give a general idea of the acoustic properties of the case being studied. See (Tsai, Fu, Tai, Huang and Leong 2009) and (Ask and Davidson 2010). Even studies which have involved expensive LES and DNS cases seem to experience a lack of accuracy and show to be very sensitive to variations and errors because of the nature of their methods. See (Kato, Yamade, Wang, Guo, Miyazawa, Takaishi, Yoshimura and Takano 2007) and (Larsson, Davidson, Eriksson and Olsson 2004).

Straightforward computational aeroacoustics shall be defined as an approach that aims to resolve the acoustic footprint of a numerical domain by capturing the pressure fluctuations

directly and rids itself from the use of acoustic models such as the ones summarized above. It can be considered the most expensive method in both temporal and spacial resolutions and will require LES or DNS to capture the fluctuations in their most direct form without relying on turbulence models which will contaminate the solution for an accurate acoustic profile. In (Tam 2004) an overview is given of the typical requirements this method calls for and the concerns it raises. Amongst the most notable ones is the dispersion and dissipation of information that is commonly associated with the numerical methods used to solve the partial differential equations (PDE's) that are related to the problem. A second is that CAA deals with greatly varying scales of information, namely the length scale of the acoustic source which is usually very different from the acoustic wavelength. Since its inception, improvements on the theory of CAA have managed to overcome many of these issues, some of which will be discussed next.

The ability to capture high frequency wavelengths calls for a typical second order CFD method to use around 20 mesh points per wavelength, a density that will yield impractically dense grids. Two approaches were developed to circumvent the need for so many mesh points, such as the compact scheme found in (Lele 1992) and the so-called dispersion-relation-preserving scheme of (Tam and Webb 1992) which aims for the finite difference scheme to have the same dispersion relations as the original PDE's and optimizes the finite difference approximations of the space and time derivatives in the wave number and frequency space. The compact scheme of Lele relies on Fourier analysis to reach an optimization in the representation of a range of wave numbers. It is also a Fourier (or Laplace) analysis approach which is used to determine the error in a modern CAA simulation. This perspective sheds light on the fact that for acoustics it's not the order of the numerical method that's important to reduce error but instead the resolved bandwidth of a scheme in wave number space (Tam 2004).

Another concern that arose with CAA was that of numerical noise generated by the scheme being used overwhelming the domain and thus blacking out the very small perturbations that are intended to be captured. Indeed it has been proven that this happens with certain schemes, but higher quality options still allow for a good analysis of very small sound waves of very small amplitude. An important study in computational noise effects was performed in (Tam and Dong 1996). Boundary conditions compromise the next concern in CAA. Given the multiple types of real life materials and the different ways that sound interacts with them means that this is a particularly hard subject to deal with. One may have, for example, a wall on which sound waves will reflect but will also transfer kinetic energy to it and make it vibrate, thus adding back perturbations to the domain. A wooden wall will instead absorb part of the energy and reflect the sound waves in another particular manner, perhaps dampening its frequency spectrum or just a part of it. There's also the case of permeable interfaces such as microphone wind screens which will let sound pass but again change its properties. Ever since the genesis of aeroacoustics motivated by the need to study jet noise, aircraft turbines have evolved into very sound conscious machines which contain acoustic lining to mitigate the radiation of noise from their inner regions. These materials, the highly complex geometry inside of the turbine with the multiple definitions of walls and boundary conditions such as inflow and outflow regions with highly varying pressure and velocity properties encased in a very high Reynolds number environment, make it a paramount example of how complex and sensitive a CAA simulation can get.

But definitely the most important aspect of CAA that is concerned with the objectives in this thesis is noise generated from turbulent regions. This approach, especially when dealing with relatively simple geometries such as those of wind turbine blades, will not be so sensitive and dependant on the aforementioned issues, particularly those of boundary conditions since in the close range noise is mainly emitted and not reflected, and in the far field where noise is just lost due to dissipation. In this case the chief concern is instead to achieve the appropriate modelling of the wide range of existing turbulence scales, yet it's still uncertain down to what degree of

resolution the turbulence range has to be modelled to predict sound accurately, namely which smaller eddies still contribute actively to the generation of sound (Tam 2004). Depending on what resolution one desires to obtain in the modelling of turbulence, the available choice of methods will boil down to the use of either LES or DNS to produce higher definition results, but which in turn will require an infeasible number of mesh points in the entirety of the numerical domain range, or to use a common workaround to this problem by using a hybrid approach in which the domain is parted into different sections, each of which is solved using a particular method. For example, one could chose to use LES close to the areas of interest regarding turbulent behaviour and then a RANS, such as a two equation turbulence model (e.g. $k-\varepsilon$), in the regions of less interest and turbulence structure complexity. Such an approach still requires a high number of computational power and time to be solved but can be easily be coupled with the theory of Ffowcs-Williams and Hawkings or Proudman/Lilley's to produce a good quality acoustic profile. In this thesis a single turbulence model $k-\varepsilon$ approach with the Proudman/Lilley theory has been used to achieve a numerical domain broadband noise profile of a section of the blade. An in-depth explanation of the methods and procedures that have been used will be offered in chapters 5 and 6.

THEORY OF NOISE GENERATION BY TRAILING EDGES

In previous chapters an insight has been laid out on what theory is involved in the modelling of fluid dynamics and aeroacoustics. A great deal of effort has been made in the past to try to overcome the complications posed by using the Navier-Stokes equations, and the purpose of trying to model acoustics adds to the challenge. In this chapter this theory is put in practice to present a series of research concerning the section of an aerofoil that is most critical to the purpose of this thesis; the trailing edge.

Achieving a clearer view on what causes trailing edge noise is fundamental to proposing new means to modify its genesis and characteristics. An analysis of theoretical, computational and experimental research is laid out to pursue this objective. The analytical methods will inevitably come under considerable limitation due to the non-linearity of the equations that are involved and these limitations confine the model to just a small number of real-life replicable scenarios. Yet, in turn, they also are of value in that they offers an insight on how other cases should behave and lay out the ground work of why noise is generated and how it could later be mitigated. A summary is also presented on the computational and experimental methods that have been used to study trailing edge noise.

4.1 The Theory of Noise Generated by a Straight Trailing Edge

The approach to study noise generated from trailing edges through analytical means has been thoroughly exposed by Michael S. Howe in a vast number of his research papers. The summary exposed in this section is based on a selection of such papers.

As it was explained briefly in section 1.2.2, sound from an aerofoil can be self generated. In a high Reynolds number environment it is attributed to the instability of the aerofoil boundary layers and their interactions with the trailing edge (Brooks, Pope and Marcolini 1989). The noise can be separated by causality in two types; that of a high frequency nature which is associated to smaller scale components of the boundary layer turbulence being the edge the generating structure, and that of low frequency which is more likely related to larger scale vorticity structures being shed from the separation layer occurring further upstream than the very edge and are due to the aerofoil geometry itself.

The desired expression in the characterization of sound and the main goal pursued in the analytical analysis of sound generation is the acoustic pressure,

$$p'(\mathbf{x}, t) \equiv p(\mathbf{x}, t) - p_0 \quad (4.1)$$

which is given formally by Curle's formula (Curle 1955)

$$p'(\mathbf{x}, t) = \frac{\partial^2}{\partial x_i \partial x_j} \int_V [T_{ij}] \frac{d^3 \mathbf{y}}{4\pi |\mathbf{x} - \mathbf{y}|} - \frac{\partial}{\partial x_i} \oint_S [p'_{ij}] \frac{dS_j(\mathbf{y})}{4\pi |\mathbf{x} - \mathbf{y}|} \quad (4.2)$$

for $|\mathbf{x}| \rightarrow \infty$ and where $[a]$ represents the value of the variable a at the retarded time $t - |\mathbf{x} - \mathbf{y}|/c_0$ being c_0 the speed of sound. Here the first integral is evaluated over the volume V which contains the fluid into which the surface element of the volume, dS_j , is directed. Furthermore, the stokesian gas tensor is

$$p_{ij} = (p - p_0) \delta_{ij} - \sigma_{ij}$$

δ_{ij} being the Dirac delta function¹ and σ_{ij} the viscous stress tensor. As seen in section 3.1, T_{ij} can be approximated to $\rho_0 v_i v_j$ at low Mach numbers and the quadrupole noise can usually be considered negligible. The edge generated noise is contained in the surface integral of (4.2) and is equivalent to that generated by a distribution of dipoles on S as the surface approaches an acoustically compact case (that is, when the aerofoil chord is much smaller than the typical acoustic wavelength) whose strength per unit area of this distribution of dipoles would be the unsteady surface pressure (Lighthill 1952) meaning that it can be approximated by the use of (4.2) and a previous knowledge of the properties of the flow near the edge. It must be taken into account that this approximation is made for an incompressible fluid and is not permissible when compressible properties are considered in the surface integral of (4.2).

The aforementioned limitation is the reason why traditionally edge noise prediction has approached the problem in two ways, namely by assuming that the trailing edge is well approximated by a semi-infinite rigid plate and by using the acoustic analogy theory of Lighthill as it was presented in 3.1 by using a compact Green's function² mathematically adapted to the shape of the trailing edge, leading to an expression of sound in terms of the vorticity in the edge flow. An overview of these approaches will be given next.

4.1.1 Modelling of trailing edge noise through a thin-plate approach

The calculation of sound generation is viewed as a scattering or diffraction problem in which the pressure p_I that is inherent to the environment is scattered by the presence of the trailing edge. In this case the geometry of the edge is given as a thin plate of semi-infinite proportions such that it lies on the $x_1 < 0$ half plane for $x_2 = 0$. The produced scattered pressure p' is composed of both acoustic and hydrodynamic components. Given a condition of low Mach number in the main stream velocity and pressure fluctuations of ω in a turbulence free region, these pressure fluctuations $p(\mathbf{x}, t)$ satisfy the Helmholtz equation

$$(\nabla^2 + \kappa_0^2) p = 0 \quad (4.3)$$

where $\kappa_0 = \omega/c_0$ is the acoustic wavenumber. Another restriction placed on this approximation is that the acoustic wavelength cannot be comparable to the thickness of the boundary layer. Having these properties, the calculation of p' reduces to the determination of the scattered pressure produced by the interaction of each Fourier component

$$\frac{p_s(\mathbf{k}, \omega)}{2} e^{i(\mathbf{k} \cdot \mathbf{x} - \gamma(k)x_2)}$$

of p_I with the surface S . This is done by using equation (4.3) and a condition to vanish the normal velocity on the halfplane as taken in a high Reynolds number approximation,

$$\left. \frac{\partial p_I}{\partial x_2} + \frac{\partial p'}{\partial x_2} \right|_{\text{on } S} = 0$$

¹See Appendix A.3

²See Appendix A.4

This procedure is non-trivial and the reader can refer to (Howe 1999) for details on it. As it was mentioned above, the idea is to arrive at an expression for the acoustic pressure and in this article it's found to be

$$p'(\mathbf{x}, \omega) \approx \frac{\kappa_0^{1/2} \sin^{1/2} \psi \sin(\theta/2) e^{i\kappa_0 |\mathbf{x}|}}{|\mathbf{x}| \sqrt{2}} \int_{-\infty}^{\infty} \frac{\sqrt{\kappa_0^{1/2} \sin \psi + k_1}}{\kappa_0 x_1 / |\mathbf{x}| - k_1} p_s dk_1 \quad (4.4)$$

where $p_s = p_s(k_1, \kappa_0 \cos \psi, \omega)$ and is approximated for $|\mathbf{x}| \rightarrow \infty$. The angles ψ and θ refer respectively to the azimuthal and elevation angles pointing in the direction of the observer which is placed at a distance of $|\mathbf{x}|$ of the source.

The acoustic pressure frequency spectrum $\Phi(\mathbf{x}, \omega)$ follows directly from its definition (Howe 1999)

$$\langle p'^2(\mathbf{x}, t) \rangle = \int_0^\infty \Phi(\mathbf{x}, \omega) d\omega$$

and is found then to be

$$\Phi(\mathbf{x}, \omega) \approx \frac{\omega L \sin^2(\theta/2) \sin \psi}{2\pi c_0 |\mathbf{x}|^2} \int_{-\infty}^{\infty} \frac{P(k_1, 0, \omega)}{|k_1|} dk_1 \quad (4.5)$$

where $P(\mathbf{k}, \omega)$ is an approximation to $p_s(k_1, 0, \omega)$ in the so-called blocked surface pressure wavenumber-frequency spectrum as defined by (Chase 1980) such that $\kappa_0 \cos \psi = 0$ and serves to eliminate the blocked pressure Fourier component of p_s to exclude a sound wave generated by the boundary layer quadrupoles in the absence of the edge, something that can be done in low Mach number cases such as this one.

4.1.2 Modelling of arbitrary trailing edge shape noise generation

By using the theory of vortex sound generation as proposed in (Howe 2006) the diffraction theory of the previous section can be extended to trailing edges of finite thickness (such that it's no longer bound to the plane $x_2 = 0$). The fundamental acoustic variable was before taken to be the pressure but now is changed for the total enthalpy, represented by B . By again having a small enough Mach number such that sound convection can be ignored, and by setting a constant fluid density, the enthalpy follows

$$\left(\frac{1}{c_0^2} \frac{\partial^2}{\partial t^2} - \nabla^2 \right) B = \text{div}(\mathbf{\Omega} \wedge \mathbf{v}) \quad (4.6)$$

where $\mathbf{\Omega} = \mathbf{\Omega}(\mathbf{x}, t)$ represents the vorticity and thus $\mathbf{\Omega} = \text{curl } \mathbf{v}$, and the operator \wedge represents the *exterior product* or wedge product³.

A special case is brought up when an irrotational medium is considered such that the enthalpy can be described by a velocity potential $\phi(\mathbf{x}, t)$ which satisfies $B = -\partial\phi/\partial t$. Furthermore, the small amplitude fluctuations in the far field are determined by the linear relation

$$\frac{p'(\mathbf{x}, t)}{\rho_0} \approx -\frac{\partial\phi}{\partial t} \equiv B(\mathbf{x}, t)$$

The solution to equation (4.6) is required, for each of its Fourier component of frequency ω , to be expressed as the sum of a Kirchhoff integral representing a contribution from the surface

³See Appendix A.5

S of the aerofoil plus the direct radiation from the vortex source (Howe 1999), such that

$$B(\mathbf{x}, \omega) = \oint_S \left[\frac{\partial B(\mathbf{y}, \omega)}{\partial y_n} G(\mathbf{x}, \mathbf{y}, \omega) - B(\mathbf{y}, \omega) \frac{\partial G(\mathbf{x}, \mathbf{y}, \omega)}{\partial y_n} \right] dS(\mathbf{y}) - \int G(\mathbf{x}, \mathbf{y}, \omega) [\text{div}(\boldsymbol{\Omega} \wedge \mathbf{v})(\mathbf{y}, \omega)] d^3\mathbf{y} \quad (4.7)$$

This equation can be manipulated by considering that the aerofoil is rigid and at rest, i.e., on the surface $\mathbf{v} \equiv 0$. Also the Green function is set to let satisfy the rigid surface condition $\partial G / \partial y_n = 0$ on S and

$$\int G \text{div}(\boldsymbol{\Omega} \wedge \mathbf{v}) d^3\mathbf{y} = - \oint_S G(\mathbf{G} \wedge \mathbf{v}) \cdot \mathbf{n} dS(\mathbf{y}) - \int (\mathbf{G} \wedge \mathbf{v}) \cdot \nabla G d^3\mathbf{y}$$

by using the divergence theorem to convert the volume integral. The resulting equation, according to (Howe 1999), is

$$B(\mathbf{x}, \omega) = \int \frac{\partial G(\mathbf{x}, \mathbf{y}, \omega)}{\partial \mathbf{y}} \cdot (\boldsymbol{\Omega} \wedge \mathbf{v})(\mathbf{y}, \omega) d^3\mathbf{y} - \nu \oint_S \boldsymbol{\Omega}(\mathbf{y}, \omega) \wedge \frac{\partial G(\mathbf{x}, \mathbf{y}, \omega)}{\partial \mathbf{y}} \cdot \mathbf{n} dS(\mathbf{y}) \quad (4.8)$$

where the surface integral can be ignored as it represents the contribution to the radiation from the unsteady skin friction on the surface which is minimal for large Reynolds numbers. The kinematic viscosity is represented by ν .

The acoustic far field is found by considering a Green function of the form

$$G(\mathbf{x}, \mathbf{y}, \omega) = -\frac{1}{\pi\sqrt{2\pi i}} \frac{\sqrt{\kappa_0} \varphi^*(\mathbf{x}) \Phi^*(\mathbf{y})}{|\mathbf{x} - y_3 \mathbf{e}_3|^{3/2}} e^{i\kappa_0 |\mathbf{x} - y_3 \mathbf{e}_3|}$$

where the potential $\Phi^*(\mathbf{y})$ describes the incompressible flow potential around the edge of the aerofoil and

$$\varphi^*(\mathbf{x}) = \sqrt{|\mathbf{x}|} \sin^{1/2} \psi \sin(\theta/2)$$

is the velocity potential of incompressible flow around the edge expressed in terms of polar coordinates such that

$$\Phi^*(y_1, y_2, y_3) \rightarrow \varphi^*(y_1, y_2)$$

as $\sqrt{y_1^2 + y_2^2} \rightarrow \infty$. Then

$$p'(\mathbf{x}, \omega) \approx -\frac{\rho_0 \kappa_0^{1/2} \sin^{1/2} \psi \sin(\theta/2) e^{i\kappa_0 |\mathbf{x}|}}{\pi\sqrt{2\pi i} |\mathbf{x}|} \left\{ \int \frac{\partial \Phi^*(\mathbf{y})}{\partial \mathbf{y}} \cdot (\boldsymbol{\Omega} \wedge \mathbf{v})(\mathbf{y}, \omega) d^3\mathbf{y} - \nu \oint_S \boldsymbol{\Omega}(\mathbf{y}, \omega) \wedge \frac{\partial \Phi^*(\mathbf{y})}{\partial \mathbf{y}} \cdot \mathbf{n} dS(\mathbf{y}) \right\} \quad (4.9)$$

for $|\mathbf{x}| \rightarrow \infty$. Evaluating this expression requires considering an analogous representation to a special case of equation (4.4) where an incident disturbance B_1 is introduced, defined to be the exact solution to equation (4.6) in the absence of the aerofoil when the vorticity and velocity have their exact values, thus coming to

$$p'(\mathbf{x}, \omega) \approx \frac{\rho_0 \kappa_0^{1/2} \sin^{1/2} \psi \sin(\theta/2) e^{i\kappa_0 |\mathbf{x}|}}{\pi\sqrt{2\pi i} |\mathbf{x}|} \int_S \left[\Phi^*(\mathbf{y}) \frac{\partial B_1}{\partial y_n}(\mathbf{y}, \omega) + \nu \boldsymbol{\Omega}(\mathbf{y}, \omega) \wedge \frac{\partial \Phi^*(\mathbf{y})}{\partial \mathbf{y}} \cdot \mathbf{n} \right] dS(\mathbf{y}) \quad (4.10)$$

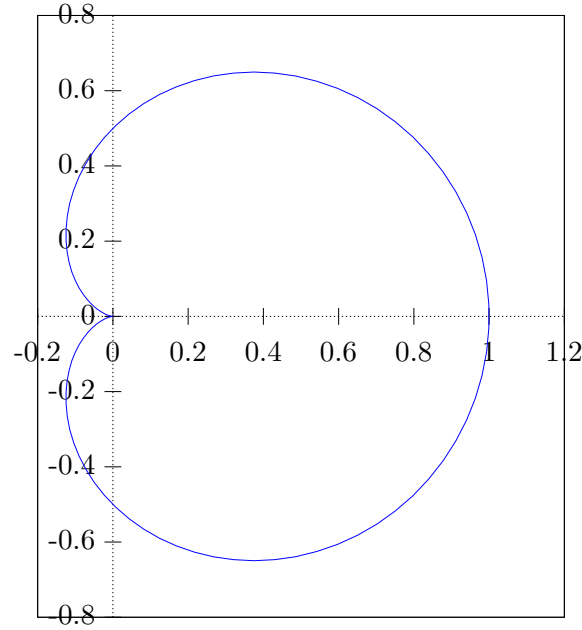


Figure 4.1: Proportionality of sound directivity for a blade positioned with its trailing edge at the origin.

where

$$B_1(\mathbf{x}, \omega) = \frac{1}{4\pi} \int_V \frac{e^{i\kappa_0|\mathbf{x}-\mathbf{y}|}}{|\mathbf{x}-\mathbf{y}|} \frac{\partial}{\partial \mathbf{y}} \cdot (\boldsymbol{\Omega} \wedge \mathbf{v})(\mathbf{y}, \omega) d^3\mathbf{y}$$

for each component of frequency ω .

Further studies in (Howe 2000) go into the analysis of aerofoils with rounded upper (suction side) geometries. It researches the behaviour of high-frequency noise in different boundary layer separation cases, to which it concludes that it would be reduced if separation occurs upstream of the edge. The approach to model this behaviour is to assume that after separation, boundary layer eddies are convected along a path parallel to the undisturbed mean stream such that their distance of closest approach to the sharp trailing edge is equal to the aerofoil thickness at the separation point. The strength of the unsteady interaction which generates sound decreases exponentially with increasing frequency. It is important to notice that his study *does* ignore contributions to sound generation from turbulence in the recirculating zone between the separation streamline and the curved section of the upper surface between the separation point and the edge, which could be expected to contribute more significantly in the lower frequency range⁴.

Experimental research conducted in (Brooks and Hodgson 1981) has shown the accuracy of the aforementioned predictions on a NACA 0012 aerofoil at low angles of attack. Their findings have also suggested that the turbulent boundary layer on an aerofoil with a sharp trailing edge radiates with an acoustic intensity that scales with U^5 and a downstream directivity proportional to $\sin^2(\theta/2)$ (see Figure 4.1).

⁴In fact, this region fails very importantly when considering noise generation in the case studied in this thesis.

4.2 Computational Aeroacoustic Research on Straight Trailing Edge Sound Generation

The theory exposed in the previous section gives an insight on the analytical approach to solving sound generation by a straight trailing edge. The mathematical analysis requires the approximation of the underlying Curle equation by performing several physical assumptions such as a low Mach number and an incompressible fluid which limit the variety of cases to which it can be applied. At the time Howe's research was laid down computational advancements still lacked the sufficient capability to be used instead of a purely analytical approach. The author himself states

“Modern computational procedures will soon yield accurate predictions of the high Reynolds number hydrodynamic motion near a trailing edge, and it is appropriate to re-evaluate the kind of numerical data that will be required to make confident predictions of the farfield sound” (Howe 2000)

Still there is a long way to go regarding computational capability in terms of the amount of cases we can handle and with what amount of precision we can approximate them, but both hardware and method advancements have allowed us to start undertaking this task.

In section 3.4 a deeper explanation has been given on the general approach on computational aeroacoustics and the use of hybrid methods was mentioned as being a useful trick to obtain a good balance between the high resolution and computational requirements that are needed. An example of a study done using this method for a straight trailing edge sound generation model is found in (Singer, Brentner, Lockard and Lilley 1999). In it, the authors have applied the Ffowcs-Williams and Hawkings analogy, thus illustrating the advantage of using numerical methods in comparison to being limited to the approximations needed for an analytical solution. But ultimately it must be remembered that, the closer one is to solving the untreated the Navier-Stokes equations, the better.

That research has used a numerical solution implemented by a code called FW-H/RKIR, which is described in (Brentner and Farassat 1998), to analyse three different cases, one of a cylinder, another of a thin plate and finally one of a non-zero thickness aerofoil. The results from the second case have shown that the use of incompressible data to obtain the integration surface quantities for use in a FW-H acoustic code leads to an incorrect solution considering that a method used to account for a finite propagation in time has not been introduced, emphasizing an important drawback in the analytical methods of Howe—which require the use of such an incompressible medium. Furthermore, it allowed to corroborate the sound directivity as proposed by (Brooks and Hodgson 1981) and shown in Figure 4.1.

Regarding the aerofoil case, a NACA series 00 was used of 2.6% thickness and 1 m chord, a profile of which can be seen in Figure 4.2. Two integration surfaces are employed, one at the aerofoil body and another at approximately 1% of the chord off the aerofoil. The numerical domain is meshed in 7 partitions that allow to provide the different resolution needs of different regions. Yet a generally very fine mesh is used and different resolutions were tested to analyse their effects on the results. Regarding these considerations, the resolution of points on the integration surface itself renders only but small changes to the acoustic profile when a straight line is used to close it in the downstream section (see Figure 4.3). On the other hand, the mesh resolution on the greater numerical domain is of greater concern, as well as the temporal resolution in the transient simulation. A comparison of their results for different mesh and time-steps sizes can be seen in Figure 4.4. A finer time resolution appears to yield a sharp difference in results despite of using a lower or higher space resolution, an emphasis of how important the accuracy of the transient solution is to the Ffowcs-Williams and Hawking method. The numerically introduced effective viscosity was also found to produce significant difference in results, even for

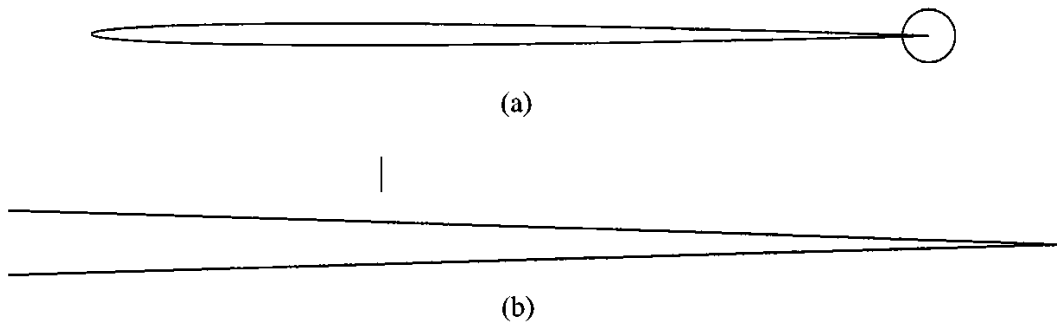


Figure 4.2: Aerofoil profile used in (Singer et al. 1999).

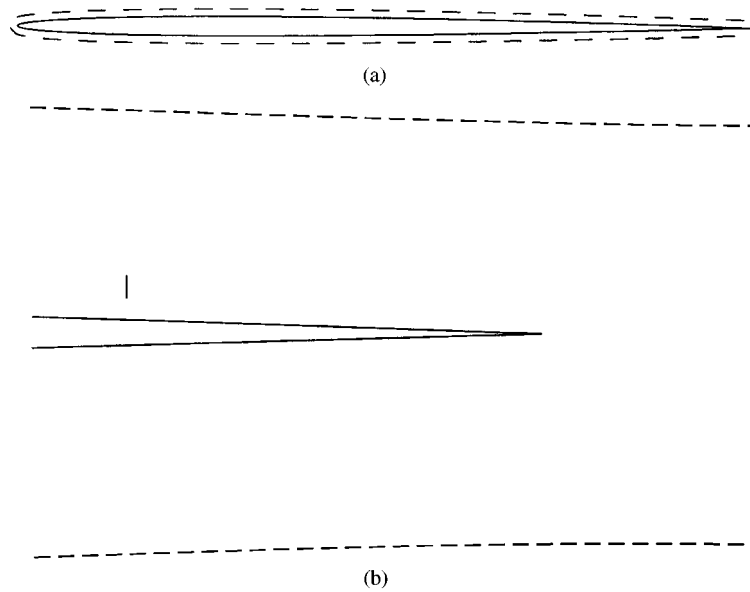


Figure 4.3: Integration surface around the aerofoil used in (Singer et al. 1999).

small discrepancies between its value in one simulation from another.

The simulations were performed at several Mach numbers, and a good agreement with the theory was obtained at a directivity of $-45^\circ < \theta < 45^\circ$, yet, at higher measurement angles the diffraction caused by the leading edge was found to make the solution distance itself from the thin plate case. An approximate scaling of the acoustic signal was found as a function of $\text{Ma}^{5.2}$ but analysis for $\text{Ma} \rightarrow 0$ on the 2D configuration implies a Ma^4 dependency. The results are found to be in acceptable agreement to the theory, yet it is noted by the authors that a complete theory that includes a finite chord of the aerofoil and finite Mach numbers (instead of a semi-finite plate approximation and infinitesimal Mach number) is needed to reach a more confident conclusion.

Another such studies was performed in (Ewert and Schröder 2004) where, instead of using the Ffowcs-Williams and Hawkings analogy used in the previously cited article, they handle the acoustic field computation with the so-called acoustic perturbation equations (APE) forced by sources determined from the unsteady flow field. These equations are derived by decomposing the flow into acoustic and non-acoustic quantities by filtering of the non-linear and viscous terms of the Navier-Stokes in the Fourier/Laplace space. Refer to (Ewert and Schröder 2003) for a

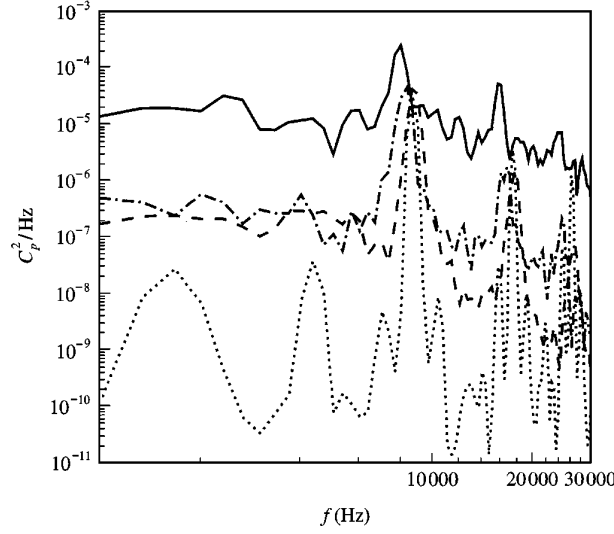


Figure 4.4: Solution comparison for different mesh and time resolutions of (Singer et al. 1999). Here the dotted line showing lower values of pressure coefficient represents the coarser resolution case, while the medium and high resolution cases are in the middle valued dashed lines. The higher value continuous line is the finer time resolution case.

discussion on this method. The equations for the perturbation variables $(p', \mathbf{u}^a)^T$ yield

$$\begin{aligned} \frac{\partial p'}{\partial t} + \bar{c}^2 \nabla \cdot \left[\bar{\rho} \mathbf{u}^a + \frac{p'}{\bar{c}^2} \bar{\mathbf{u}} \right] &= \bar{c}^2 q_c \\ \frac{\partial \mathbf{u}^a}{\partial t} + \nabla (\bar{\mathbf{u}} \cdot \mathbf{u}^a) + \nabla \left(\frac{p'}{\bar{\rho}} \right) &= \mathbf{q}_m \end{aligned}$$

where \bar{a} is the mean of a variable a , p and ρ refer to the pressure and density, \mathbf{u} refers to the main stream velocity, \mathbf{u}^a the acoustic velocity perturbations, q_c and \mathbf{q}_m source terms which are defined as

$$\begin{aligned} q_c &= -\nabla \bar{\rho} \cdot \mathbf{u}^\nu - \nabla \cdot [\rho' \mathbf{u}']' + \frac{\bar{\rho}}{c_p} \left(\frac{\partial}{\partial t} + \bar{\mathbf{u}} \cdot \nabla \right) s' \\ \mathbf{q}_m &= -\frac{\partial \mathbf{u}^\nu}{\partial t} - \nabla (\bar{\mathbf{u}} \mathbf{u}^\nu) - [\omega \times \mathbf{u}']' - \nabla \frac{(u')^2}{2} + \left[\frac{\nabla \cdot \boldsymbol{\tau}}{\rho} \right] + T' \nabla \bar{s} - \nabla \bar{T} s' \end{aligned}$$

and $\bar{c}^2 = \gamma \bar{p} / \bar{\rho}$. The complete perturbation velocity is $\mathbf{u}' = \mathbf{u}^a + \mathbf{u}^\nu$, where the last term shown here is the so-called *solenoidal* part of the perturbation velocity and follows directly from an incompressible flow simulation to satisfy the theory behind this method. The mean flow can be computed using RANS or Euler methods, but LES is usually used in the regions close to the trailing edge of the aerofoil geometry to simulate the turbulent compressible flow more accurately.

For the spacial discretization of APE, a fourth order dispersion relation preserving scheme was used. See (Tam and Webb 1993). The temporal integration was carried out with a fourth order alternating two-step low-dissipation and low-dispersion Runge-Kutta scheme. See (Hu, Hussaini and Manthey 1996). They have used different Reynolds numbers varying from 5×10^5 to 7×10^5 and a free stream Mach number of 0.15 in a numerical domain containing 2.22×10^6 points. An example of a pressure contour solution for such a case can be seen in Figure 4.5. They have found that sound directivity conforms to that predicted by Howe but, unlike (Ewert

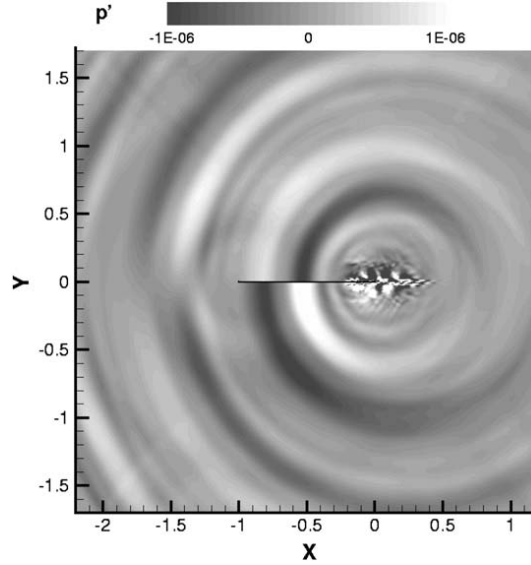


Figure 4.5: Pressure contours for $Ma = 0.15$, $Re = 7 \times 10^5$ at $t = 3.0$ from (Ewert and Schröder 2004)

and Schröder 2004), in this research a thin plate approach is used instead of the thick geometry aerofoil. Due to this, it's expected to adhere better to the theoretically obtained values. Non the less, it also finds that, with increasing wave numbers, a multi-lobe pattern begins to show (see Figure 4.6).

4.3 Computational Aeroacoustic Research on Straight Trailing Edge Wind Turbine Blades

4.3.1 A TNO model application

In (Bertagnolio 2008), the so-called TNO model as described in (Parchen 1998) is applied to the analysis of sound generation from a wind turbine blade profile. This model relies on several methods including Lighthill's analogy as described in section 3.1, diffraction theory as seen in section 4.1 and a vortex method developed in (Howe 1978).

The wavenumber frequency pressure spectrum in this case is described as

$$\Phi_P(\mathcal{K}, \omega) = 4\rho_0^2 \frac{K_1^2}{K_1^2 + K_3^2} \int_0^\infty L_2(y_2) \bar{u}_2^2 \left(\frac{\partial U_1}{\partial y_2}(y_2) \right)^2 \Phi_{22}(\mathcal{K}, \omega) \times \Phi_m(\omega - U_c(y_2) k_1) e^{-2|k|y_2} dy_2 \quad (4.11)$$

where L_2 is the vertical integral length which characterizes the vertical extent of the turbulent eddies, \bar{u}_2^2 is the root mean square value of the vertical velocity fluctuations, Φ_{22} is the spectrum of the vertical velocity fluctuations (also known as turbulent shear stress). Φ_m is the moving axis spectrum which describes how Φ_{22} is distorted by the generation and destruction of eddies during their convection past the trailing edge and finally U_c is the convection velocity of these eddies. The terms Φ_{22} and Φ_m are given analytically and, with the help of this, equation (4.11) can then be related to the far field noise.

The TNO model is validated against previous experimental measurements performed on the VTE-kav aerofoil designed at the Institut für Aerodynamik und Gasdynamik der Universität Stuttgart. See (Herrig, Würz and Wagner 2003). A Reynolds number of around 3.1×10^6 and

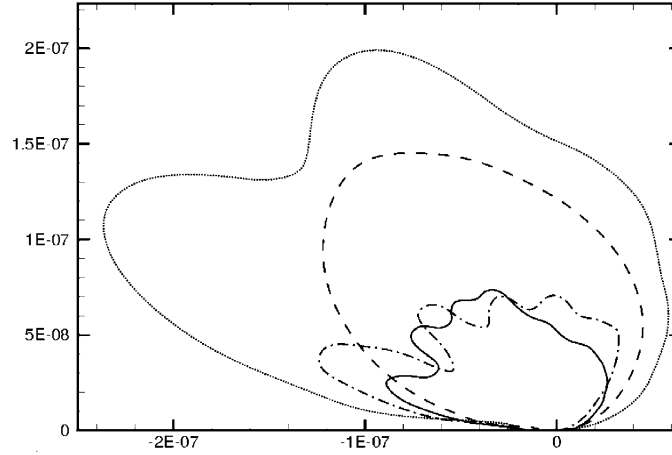


Figure 4.6: Directivity from (Ewert and Schröder 2004) showing the multi-lobe patterns of different wave number acoustic results. The trailing edge is placed at the origin.

a Mach number of 0.178 were used. The angle of attack was set at 2.7° and the sound was measured in the far field at 1 m from the trailing edge. The numerical results with TNO were seen to critically underestimate the experimental measurements, as it can be seen in Figure 4.7.

When comparing the results with research conducted using a CAA approach on a NACA 0015 aerofoil in (Zhu 2007), the results also seem to suffer the same deficiency (refer to Figure 4.8). It must be taken into account that the available angle of attack used in the CAA research doesn't fit the case studies for the TNO model or the experimental data obtained from the VTK-kav aerofoil. Instead, in this case $Re = 10^5$, $Ma = 0.2$ and the LES and CAA computations were performed in 2D. The LES calculation method is seen to produce better turbulence modelling compared to the RANS simulation, as it is expected. Both were used to feed the TNO with data for the acoustic simulation, but the LES-fed TNO data fits better with the CAA study of Zhu. RANS on the other hand predicts lower sound pressure levels, yet it does follow the general shape of the acoustic profile, meaning that it can predict, with a certain level of accuracy, where the acoustic frequency highs and lows will occur but perhaps not their levels.

An interesting result that was obtained in that research comes from the comparison of different aerofoils with two different angles of attack, $\alpha_1 = 0^\circ$ and $\alpha_2 = 3^\circ$. At the lower AOA, α_1 , all three aerofoils exhibited lower sound pressure levels at a lower frequency than at α_2 . The peak level frequency was found to be higher pitched but quieter at the lower AOA and then at higher frequencies both angles kept closely the same levels but with α_1 still slightly lower. This result can be seen in Figure 4.9.

Ultimately the research concludes that the model still cannot be trusted to produce high fidelity results in terms of sound pressure level frequency spectra since the results do differ significantly from the experimental data. Still, the techniques are valued for their ability to offer significant insight when used to compare results between different aerofoils or conditions such as AOA and Mach or Reynolds numbers, something that will remain a leitmotiv in this thesis.

4.3.2 Using a FW-H approach

The use of the Ffowcs-Williams and Hawkings (FW-H) approach (as seen in section 3.2), applied noise simulation in wind turbine blades has been applied in (Morris, Long and Brentner 2004). This method just requires that the FW-H equations be fed by the basic parameters needed to solve them and are usually drawn from an appropriate CFD method as long as it manages to

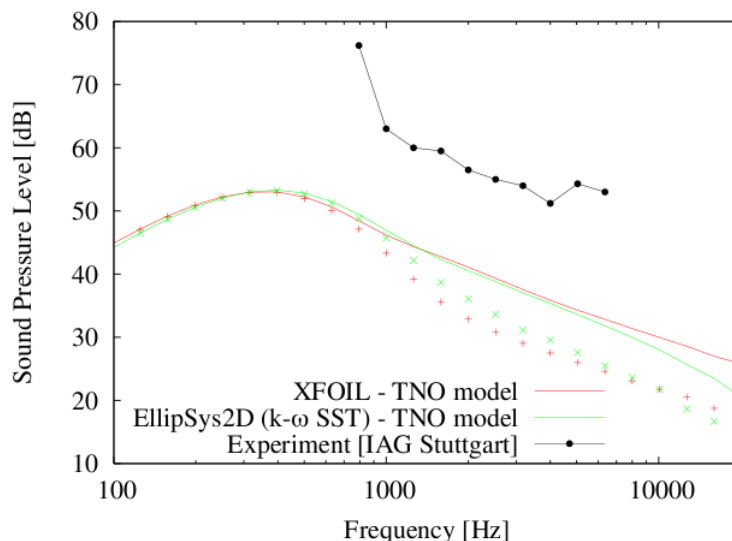


Figure 4.7: Sound pressure level result comparison for the TNO model and experimental observations (black). The points represent results from the TNO model being applied to the suction side of the blade only. (Bertagnolio 2008)

capture them accurately enough.

It's the achievement of this accuracy that can be tricky and requires that both the attached and separated flow created by the blade are well modelled—since both of them are expected to be causal of noise generation in different frequency and amplitude scales. The former is known to be successfully predicted by RANS simulations and the latter by LES, yet, since it's desirable to be able to accurately capture both, the authors have used a model called Detached Eddy Simulation (DES), which can be adapted to the $k-\varepsilon$ and $k-\omega$ models and was first described by (Spalart, Jou, Stretlets and Allmaras 1997). It can be seen as a hybrid RANS/LES model since, in attached flow regions the distance to the nearest wall determines the turbulent length scale, and in separated flow it's instead set by the grid size, thus providing an automatic transition between unsteady RANS (URANS) and LES. To achieve a compromise between scale capturing and computational requirements, the authors have used this method to provide a coarse simulation over the large-scale unsteadiness of the flow with both attached and just mildly separated boundary layers, thus relaxing the mesh size requirement over the larger numerical domain by not fully modelling the separated flow.

The finer turbulent scales encountered in the boundary layer near the aerofoil trailing edge are being solved by a LES model that accounts for the perturbations about the assumed mean flow—which is in turn modelled by DES. This method is described in (Morris, Long, Bangalore and Wang 1997) and is called the Non-Linear Disturbance Equations model (NLDE). The choice of this method over LES lies in that it has been found to increase the accuracy of the solution in the acoustic field and establishes a statistically stationary solution faster.

The coupling of these compressible flow simulations with the FW-H equations allows the prediction of the desired far-field noise. This is done by the authors through a software called Compressible, High-Order, Parallel, Acoustics code (CHOPA) which is based on an explicit 4th order Runge-Kutta time marching scheme with 4th order Dispersion-Relation-Preserving spatial discretization. This is applied on stationary blade geometries to model aerofoil self-noise.

An added difficulty of modelling wind turbine far-field noise in real life settings is the presence of irregular terrain and non-isotropic atmospheric characteristics that will perturb the behaviour

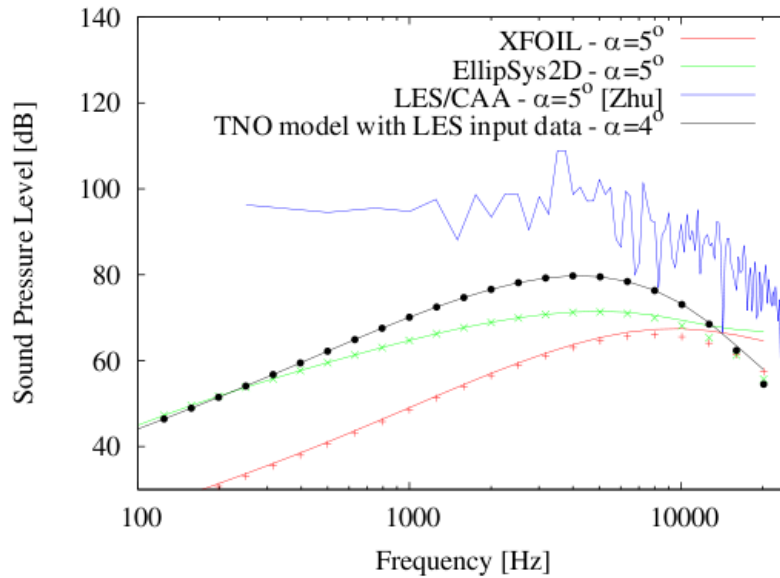


Figure 4.8: Sound pressure level result comparison for the TNO model (black) and a CAA simulation (blue). (Bertagnolio 2008)

of sound propagation that exceeds the line-of-sight capabilities of FW-H. This fact is further emphasized by the ability of low frequency noise to travel long distances before dissipating to a non-contributing level. The solution used by the authors is to predict acoustic propagation in the far-field by using the linearised Euler equations (LEE), thus a third coupling is used in the numerical simulations. Again, the importance of scaling in the problem is highlighted and represents the key in maintaining a balanced level of accuracy and the computational expense needed to achieve it, and address the specific case needed to be solved, be that the analysis of noise generating structures, testing of new geometries, collective wind turbine noise propagation over wide terrains, and behaviour of noise generation under varying atmospheric conditions.

The case is further complicated by considering rotating blades instead of stationary structures. This problem adds factors that include the possibility of having significant spanwise or radial flow, varying flow field from the root to the tip of the blade, and the prolonged proximity of the wake created by the blade to the blade itself, in comparison to a regular wing. LES is suggested to properly be able to address these phenomenons and also is the use of variable boundary conditions considered to allow modelling more real situations such as those of wind gusts, incoming turbulent flows and wind shear. The simulation technology used to model this in wind turbines has been directly adapted from the extensive research that's been applied to helicopter rotor noise prediction. In particular, a code known as WOPWOP has been successful in achieving this, even when considering complex blade-vortex interactions. Results can be seen in Figure 4.10, from (Brentner and Farassat 1994). This code has been extended into another, known as PSU-WOPWOP, and is presented in (Brentner, Perez and Bres 2002). For its scenario handling capabilities, it's been proposed as a suitable candidate code for use in wind turbine modelling by (Morris et al. 2004).

4.4 The Effect of Serrated Trailing Edges on Sound Generation

In section 4.1 an overview was presented regarding previous research on the generation of sound by classic straight trailing edges in both an ideal flat plate and arbitrary thickness models. This approach led to deriving the acoustic pressure generated by the disturbances in the mean flow by

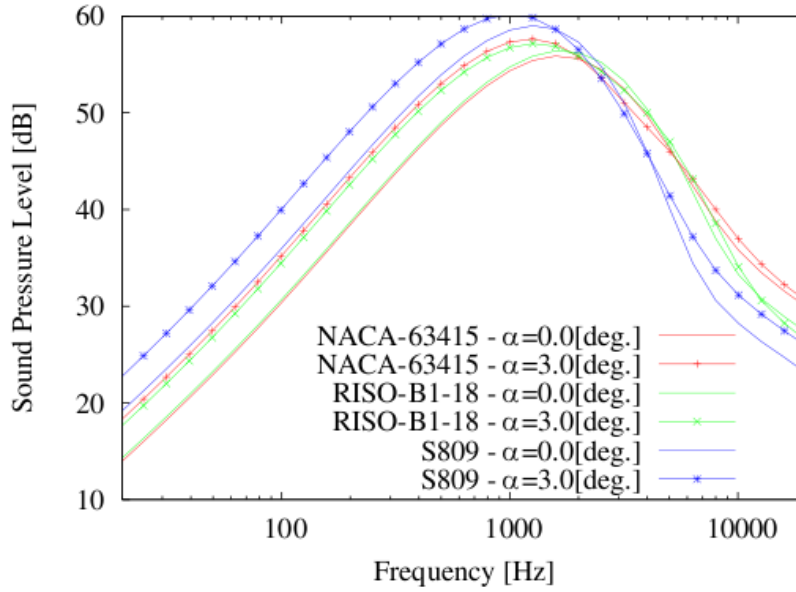


Figure 4.9: Comparison of sound level generation for two angles of attack of three different aerofoils as solved by the TNO model according to (Bertagnolio 2008).

the aerofoil through the use of diffraction theory, where an appropriate form of Green's function and the entropy expression was fundamental, as well as considerations such as low Mach numbers and having an incompressible fluid to make the associated equations solvable by approximations, as well as by having several terms such as vorticity and velocity fields readily known before hand.

In this section a presentation will be given on what effect the use of serrated trailing edges is expected to have in terms of noise generation.

In (Howe 1990) an attempt to solve this problem analytically is proposed by repeating many of the assumptions made in the non-serrated geometries, as seen in the previous section. For this purpose, the frequencies considered are taken to be large enough such that the wavelength of the sound is still small compared to the chord of the aerofoil such that it can again be considered as a half-plane but with a trailing edge geometry which is defined as

$$x_1 = \zeta(x_3)$$

A graphic representation of this geometry is given in Figure 4.11. It is important to note that Howe used sinusoidal serrations in his calculations instead of a sawtooth shape, mainly because this keeps the solution of $\partial\zeta/\partial x_3$ continuous while instead a sharp corner, like that used in a sawtooth geometry, will yield discontinuities making the analytical derivation much more complicated to handle. He separates the pressure as a sum of an incident pressure field which is unchanged by the presence of the aerofoil and a diffracted pressure produced by its presence and the consequent trailing edge effects

$$p(\mathbf{x}, t) = p_0(\mathbf{x}, t) + p_s(\mathbf{x}, t)$$

It's possible to know p_0 beforehand and both are represented as Fourier integrals,

$$\begin{aligned} p_0(\mathbf{x}, t) &= \int_{-\infty}^{\infty} \mathcal{P}_0(\mathbf{x}, \omega) e^{-i\omega t} d\omega \\ p_s(\mathbf{x}, t) &= \int_{-\infty}^{\infty} \mathcal{P}_s(\mathbf{x}, \omega) e^{-i\omega t} d\omega \end{aligned}$$

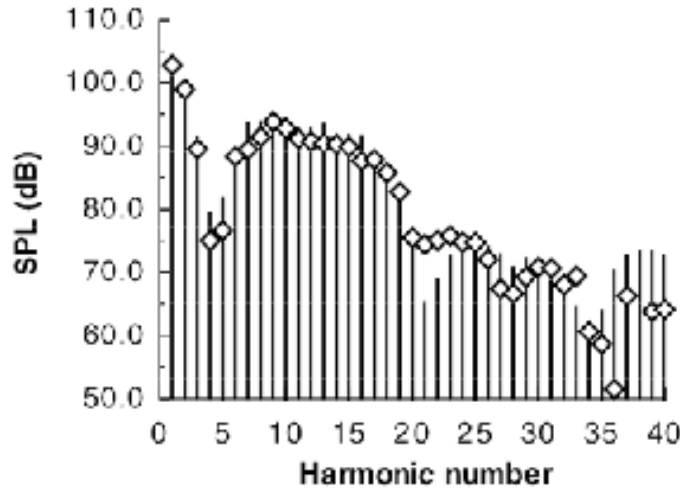


Figure 4.10: Measured (squares) and predicted sound pressure level results as obtained in (Brentner and Farassat 1994) by the code WOPWOP applied to helicopter rotors.

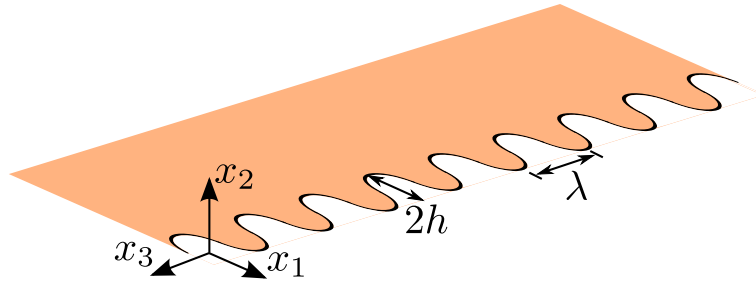


Figure 4.11: Description of the semi-infinite plane serrated aerofoil geometry used in this section

where the terms \mathcal{P}_0 and \mathcal{P}_s satisfy

$$\begin{aligned} \{\nabla^2 + k_0^2\} \mathcal{P}_0 &= Q(\mathbf{x}, \omega) \\ \{\nabla^2 + k_0^2\} \mathcal{P}_s &= 0 \end{aligned}$$

for the proposed assumptions and where $Q(\mathbf{x}, \omega)$ is the Fourier time transform of the aerodynamic quadrupole source as proposed in (Lighthill 1952). Green's function is then used to define the diffraction radiation \mathcal{P}_s , and on which the boundary condition $\partial G / \partial x_2 = 0$ is applied for $x_1 < \zeta(x_3)$. By using the divergence theorem, it can be expressed as

$$\mathcal{P}_s(\mathbf{x}, \omega) = \oint G(\mathbf{x}, \mathbf{y}; \omega) \left[\frac{\partial \mathcal{P}_s(\mathbf{y}, \omega)}{\partial y_n} \right] dS(\mathbf{y})$$

taken over the upper and lower surfaces of the aerofoil. Here y_n is normal to it and positive into the fluid region. By further manipulating this equation it can be written as

$$\begin{aligned} \mathcal{P}_s(\mathbf{x}, \omega) = \frac{i}{2} \int_{-\infty}^{\infty} dy_3 \int_{-\infty}^0 dz_1 \int_{-\infty}^{\infty} \gamma(K) [G(\mathbf{x}, z_1 + \zeta(y_3), y_3; \omega)] \\ \times \hat{p}_b(\mathbf{K}, \omega) e^{i[K_1 z_1 + K_3 y_3 + K_1 \zeta(y_3)]} d^2 \mathbf{K} \end{aligned} \quad (4.12)$$

using the change of variable $z_1 = y_1 - \zeta(y_3)$ and by applying the boundary condition

$$\frac{\partial \mathcal{P}_0}{\partial x_2} + \frac{\partial \mathcal{P}_s}{\partial x_2} = 0$$

for $x_2 = \pm 0$ and $x_1 < \zeta(x_3)$.

To analyse the sound reduction attributes of the applied serrations, consider a turbulent eddy of wavenumber \mathbf{K} convecting at a velocity U_c . This eddy will generate sound of frequency $\omega \approx U_c K_1$ (Howe 1990) as a cause of interaction with the trailing edge. The eddy length scale possibilities can be parted in two, one for which it exceeds the amplitude of the serrations and one for which they are smaller. In the former case, i.e. when $K_1 \zeta \ll 1$, the acoustic pressure frequency spectrum, $\Phi(\omega, \mathbf{x})$, as defined in section 4.1.1, will be very similar from the case of an unserrated aerofoil. In the latter case, though, where $K_1 \zeta \gg 1$, the integrand in (4.12) oscillates rapidly as y_3 varies and the serrations will then tend to reduce the effective spanwise wetted length of the trailing edge responsible for the generation of sound from the actual length l to an aggregate length l_e of those sections within $|\partial \zeta / \partial y_3| < 1$. In this case, and for high frequencies, the corresponding acoustic spectrum can be estimated by

$$\Phi(\omega, \mathbf{x}) \approx \frac{l}{l_e} \Phi_0(\omega, \mathbf{x})$$

If sinusoidal serrations are considered, then

$$\zeta(y_3) = h \cos \frac{2\pi y_3}{\lambda}$$

thus, over one complete wavelength of the serrations, the total spanwise length of the edge wherein $|\partial \zeta / \partial y_3| < 1$, is $4L$, where

$$L = \frac{\lambda}{2\pi} \sin^{-1} \frac{\lambda}{2\pi h} \approx \frac{\lambda^2}{4\pi^2 h}$$

Here the last approximation is taken for $\lambda/h \lesssim 4$. Also $l_e \approx 4L(l/\lambda) \approx l\lambda/\pi^2 h$ for a not too large value of λ/h . The acoustic pressure frequency spectrum is approximately

$$\Phi(\omega, \mathbf{x}) \approx \frac{\Phi_0(\omega, \mathbf{x})}{\pi^2 h / \lambda}$$

for $\omega h / U_c \gg 1$, hence (Howe 1990) predicts a reduction in the high frequency range of about $10 \log(10h/\lambda)$ [dB]. Furthermore, it concludes that high frequency noise can be reduced by using a sawtooth serration geometry in which the straight edges are inclined to the mean flow direction at angles not exceeding 45° . In this case, the largest contributions to the y_3 integral in (4.12) are caused by the tips and roots of the sawtooth geometry.

It is through this reasoning that this research assumes that an attenuation can be achieved. It attributes it to a reduction in the spanwise length of the trailing edge that is actively contributing to the generation of sound, namely because a turbulent layer eddy convecting over the edge, characterized by the wavenumber vector $\mathbf{K} \equiv (K_1, 0, K_3)$ generates edge noise only in the neighbourhood of those regions where \mathbf{K} is normal to the edge. Numerical analysis of this theory has predicted an attenuation of about 8 dB for $\lambda/h = 1$ and less than 1 dB for $\lambda/h \gtrsim 10$ in serrations placed at the exhaust of a jet engine.

Non the less, it must be stressed that, due to the assumptions made in this research, the theory is greatly limited to cases such as those that would be encountered in underwater applications, and contrary to aerospace cases such as the one addressed in this thesis. To expand the domain of applicability of the theory of aeroacoustics into more real life conditions such as those found in wind turbines to predict the behaviour of sound generation by the presence of serrated trailing edges, one must turn to numerical methods instead of analytical ones.

4.5 Trailing Edges Noise Generation and Experimental Research



Figure 4.12: Test set-up used by (Oerlemans and Méndez-López 2005) to measure noise sources on a wind turbine with results visualized in a colour scale.

Of course, other than what has been presented in the previous sections, one other approach to studying sound generation in aerospace applications is by conducting on-site or wind tunnel measurements. The very well known drawbacks of these methods include having to build specialized facilities where the research will be conducted, having to manufacture the prototypes which will be studied, and, amongst others, finding an accurate way of measuring whatever parameters are desired to be known. In turn, the choice of these parameters will have a great impact on the requirements of the methods and hardware that's used.

In acoustics, an added difficulty compared to regular aerodynamic studies lies in that no external noise pollution may exist that could interfere with the observations made (or an appropriate way of filtering it would have to be applied). Therefore, if a wind tunnel is going to be used to reproduce a real-life scenario, it must be retrofitted accordingly to provide an acoustically acceptable environment considering that it should help avoid noise from echo sources, i.e. it should resemble an anechoic chamber. On the other hand, field mea-

surements made on an operating wind turbine will add additional considerations of environmental nature such as external noise sources including those from nearby trees, other wind turbines or ground-wind interactions. The conditions under which the turbine will find itself are by nature varying and relatively unpredictable. Despite of this, field measurements *are* needed and are of particular usefulness if taken over a larger period of time such that they can provide data concerning noise behaviour caused by the changing climatic conditions of a particular region. Furthermore, on-site measurements are practically unreproducible by other currently available methods if one wished to measure sound levels inside houses or other residential settings placed across uneven terrain in medium to long distances from the wind turbine farms.

Despite these difficulties, an important acoustic analysis of wind turbine noise sources has been achieved by placing a carefully arranged grid of microphones a certain distance from an operating wind turbine and then evaluating the resulting signals for small lag differences and other effects that allow to pinpoint sound directivity. This difficult task has been undertaken in (Oerlemans and Méndez-López 2005) where an array of 152 microphones placed in a $15 \times 18 \text{ m}^2$ area 58 m in front of a GAMESA G5 wind turbine. This measurement was made on-site at wind speeds between 6 to 10 m/s. A photograph of this experiment can be seen in Figure 4.12 where the sound source result visualization is overlaid and the microphone array platform can be seen in the lower left corner in front of the wind turbine. The rotor movement is in the clockwise direction. The measurements were obtained during a 7 day period and total 110 samples out of which the goal was to achieve 30 valid measurements. Those selected were then separated to certain parameter limits such as

- variation of wind speed ($\pm 1.5 \text{ m/s}$ of average),

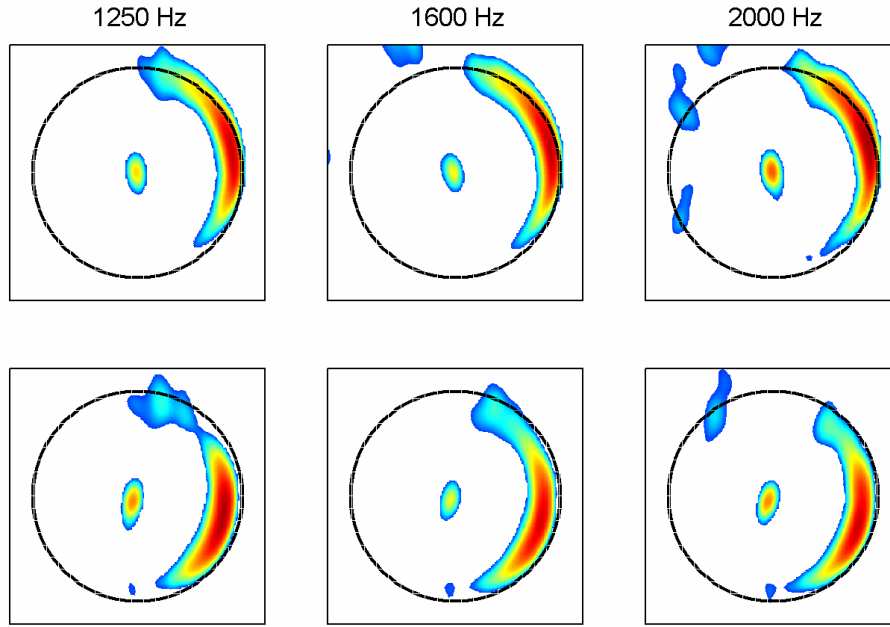


Figure 4.13: Shift of blade noise source due to rotor misalignment in respect to the measuring position. In the top line the rotor was at 11° to the right of the array and in the bottom line it was at 12° to the left. The rotor is moving clockwise and the colour range represents a 12 dB difference.

- $\pm 2^\circ$ misalignment between the microphone platform and the rotor direction but not larger than 12° ,
- variation in rotor RPM within 8% of average,
- variation of blade pitch $\pm 3^\circ$ of average,
- acoustic pollution of less than 1%

The most important and clear result from this study is that the principal noise source in the blades does appear to be the trailing edge. But in addition, two more observations present new and very interesting perspectives. First, despite of that the blade tip had been assumed to be an important noise source, the main source appears instead to be located at the outer parts of the blade but not the very tip—about 75% to 95% of blade length measured from the root. The second observation is that noise seems to be picked up mainly on the downward motion of the blade. The former result will be crucial when planning a noise reduction strategy such that the correct portion of the blade geometry is addressed. The latter is important in that it verifies the periodic noise generation in wind turbines, a property that could account for much more distress in human comfort levels than, for example, a constant intensity sound source—consider trying to sleep close to a dripping faucet versus a constant flowing one albeit having both produce the same sound level.

Misalignment of the rotor in respect to the microphone array seemed to produce a slight shift in the sound source position along the radius. This can be accounted for the relative shift in downward motion of the blade in respect to the observation platform. The results from a misaligned measurement can be seen in Figure 4.13. In addition, the noise was found to be mainly of a broadband nature, as seen in Figure 4.14, and blade noise is observed to increase faster than hub noise for increasing wind speed, yet the latter has an important contribution at $630 \cdot \text{Hz}$ which is attributed by the authors to the gearbox. Furthermore, a relation of U^5

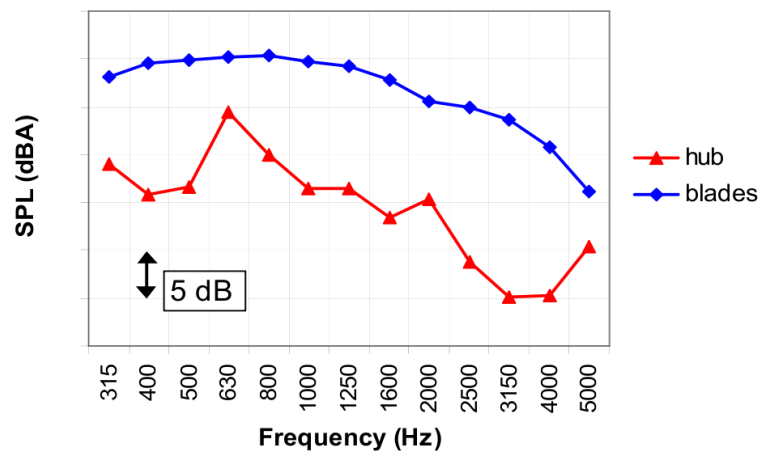


Figure 4.14: Measured sound level of a wind turbine over the acoustic spectrum by (Oerlemans and Méndez-López 2005)

was found between wind speed and sound generation, something predicted in previous studies, including (Wagner et al. 1996).

In a related study, (Oerlemans, Schepers, Guidati and Wagner 2001), a similar approach was used to study the noise generation impact of using serrated trailing edges on a wind turbine placed inside an anechoic chamber at the German-Dutch Wind Tunnel's large low-speed facility in Marknesse, the Netherlands. In this case, an array of 136 microphones was placed on a $4 \times 4 \text{ m}^2$ area. Processing of the data was achieved by using a delay/sum algorithm to obtain the noise source distribution in the stationary rotor plane and also by applying a method called Rotating Source Identifier to pinpoint the noise sources on the rotating blades. Five different types of serrations were used on three rotors, namely an X3 and an X5, which are acoustically optimized designs resulting from the researched conducted in (Guidati, Wagner, Parchen, Oerlemans, van den Berg, Schepers, Braun and Kooi 1999), and a reference aerofoil, the NACA-64418. The experiments were conducted at a wind speed of 14 m/s, an RPM value of 424, and the optimum blade pitch angle (not specified).

Conclusions drawn from this research state that, first of all, a general blade geometry optimization to minimize noise generation is possible, as shown with the X5 rotor, providing a noise reduction of up to 4 dB. But furthermore, the use of serrated trailing edges allows for an extra 2-3 dB reduction on this blade especially observable at higher frequencies ($> 2000 \text{ Hz}$). A plot showing a comparison of sound intensity levels between a standard and a serrated X5 for 8000 Hz is seen in Figure 4.15. The article doesn't specify the serration dimensions that were used.

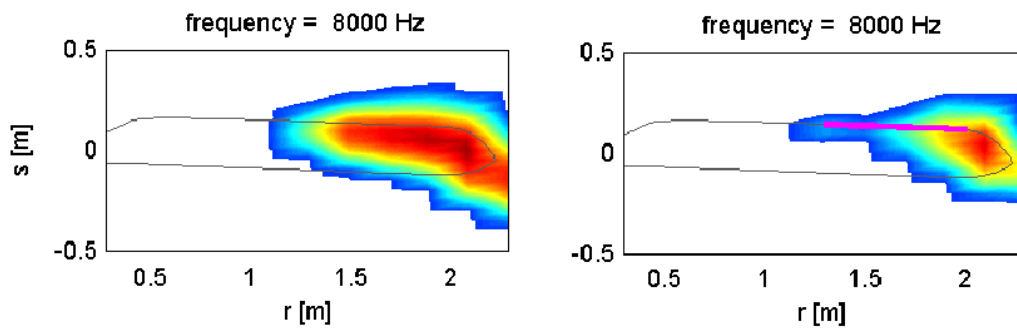


Figure 4.15: Sound intensity plots for a standard and a serrated X5 rotor. The magenta line on the right plot represents the position of the serrations. (Oerlemans et al. 2001).

CASE SET UP

In the previous chapters an overview of the mathematical and numerical theory of computational fluid dynamics and acoustics has been given. It constitutes the foundation of what will be exposed in the current chapter to outline the procedure that was followed to perform the model simulations. An explanation shall be given on what blade geometries were used in this study, the mesh characteristics and numerical methods that were applied.

5.1 Blade Geometry

In (Oerlemans and Méndez-López 2005) noise of wind turbine blades is seen to be generated at around 75% to 95% of the blade length. The blade profile that is used in the research presented in this thesis has been provided by the Denmark based blade designer and manufacturer LM Wind Power as a model used in about 35% to 55% of some of their blade design's length, which range from 40 m to 61.5 m long. The discrepancy between the sections at which this profile is used with the region of the blade that is expected to generate sound is of no concern since what is desired in the analysis is the comparison between noise and CFD behaviour of the different three-dimensional geometries and serrations that were chosen for this research.

It shall be stressed now—and explained later with more detail—that the objective of this study will be addressed using a comparative approach of the different results obtained by modelling a small section of the blade under realistic operating conditions. That is, instead of attempting to model the entirety of an operating wind turbine, task which would require unrealistic computational power in terms of what's available at the time of writing this thesis.

In addition, it shall be noted that no precise details will be given on the geometry of the blade profile so as to protect the intellectual property of LM Wind Power. Neither can the expected aerodynamic results be published and instead only the obtained figures shall be used. Despite of this, it must be also noted that the blade *has* been slightly modified from its original form to a degree small enough such that any discernible differences in its aerodynamic properties shouldn't be expected.

For the simulations, a two-dimensional model of the blade was used for preliminary tests, both of aerodynamics and aeroacoustics. In the three-dimensional simulations a blade section was used with a chord length of 1.5 m and spanwise length of 0.3 m. This width fits 8 serrations of $\lambda = 0.0375$ m wavelength. To study the effect of different serration ratios, λ/h , where h is the serration amplitude, two values of h were used, $h_1 = 0.075$ m and $h_2 = 0.15$ m such that the serration ratios are $\lambda/h_1 = 0.25$ and $\lambda/h_2 = 0.5$. A rendering of these models can be seen in Figure 5.1 and an overlay of the geometries can be seen in Figure 5.2. Figure 5.3 shows a close up of the serrations.

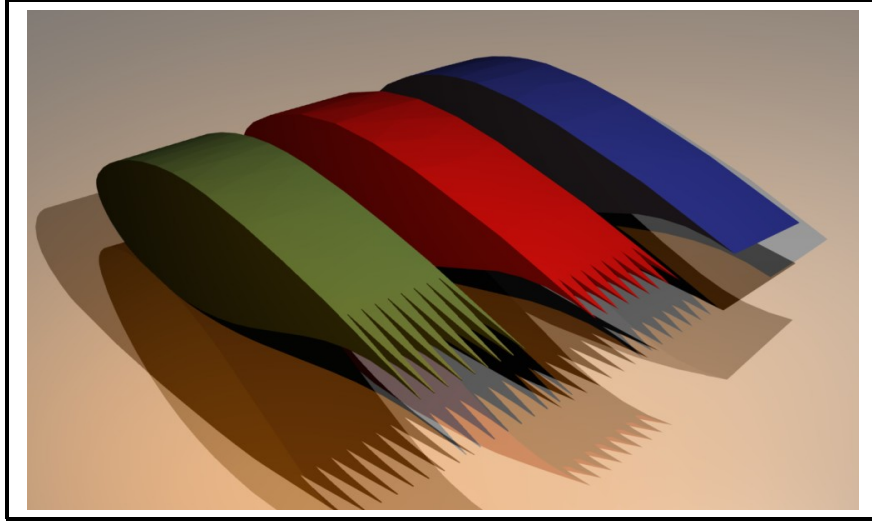


Figure 5.1: Rendering of the three blade geometries used in this research

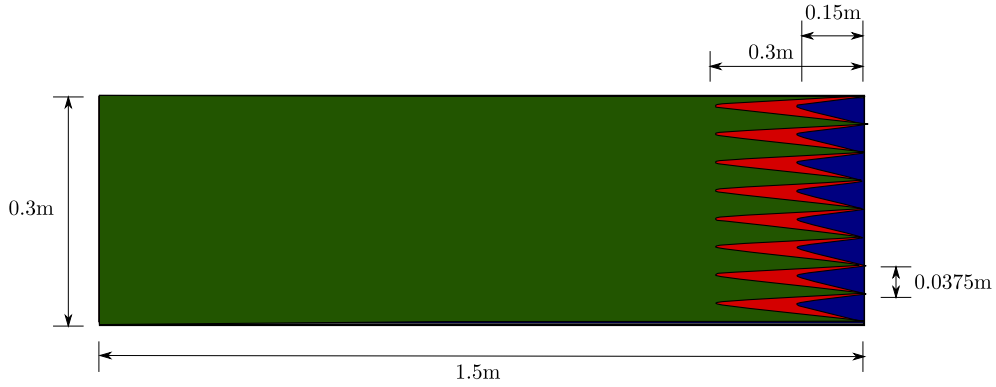


Figure 5.2: Overlay of the three-dimensional serration geometries used. In green is $\lambda/h_1 = 0.25$; in red is $\lambda/h_2 = 0.5$; in blue is the original blade geometry without serrations. *Note: in this graph the shown geometries do not adhere precisely to those used in the simulations and are just for illustration purposes and showing of the serration dimensions that were used.*

The choosing of the serration ratio was based on recommendations given in (Howe 1990) and exposed in Section 4.4. From his research, it's expected to reduce noise as $10 \log(10h/\lambda)$ [dB] in the height frequency range. The serrations were made by cutting straight wedges (triangular prisms) off from the original blade. This leaves a series of serrations that extend *into* the aerofoil body leaving thicker edges in the serration's valleys (the innermost arista). The presence of these blunt sections is expected to change the performance of the blade by introducing new and complex flows in the areas immediately behind them. Amongst the effects, varying pressure regions behind the blunt trailing edges are expected to be encountered which can sharply modify the blade's drag coefficient, C_d . A more detailed analysis of this shall be given in the next chapter. Other serration geometries are possible and could fair better both aerodynamically and costwise at the manufacturing/retrofitting stage. The achievement of these goals go beyond the objective of this research and the effort will be concentrated in comparing the acoustic behaviour changes amongst the proposed geometries. All the blades were built solely on Gambit from the 2D x - y vector dataset provided by LM Wind Power.

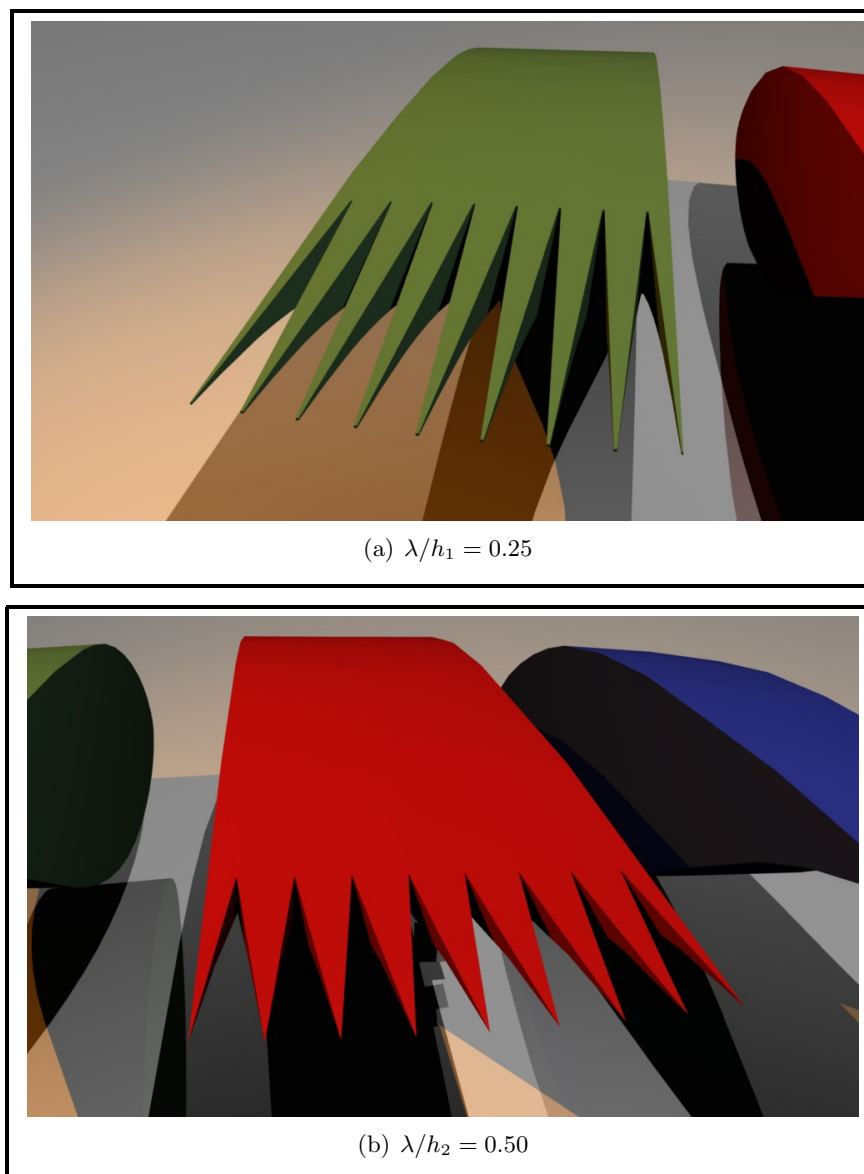


Figure 5.3: Close up of the serrations.

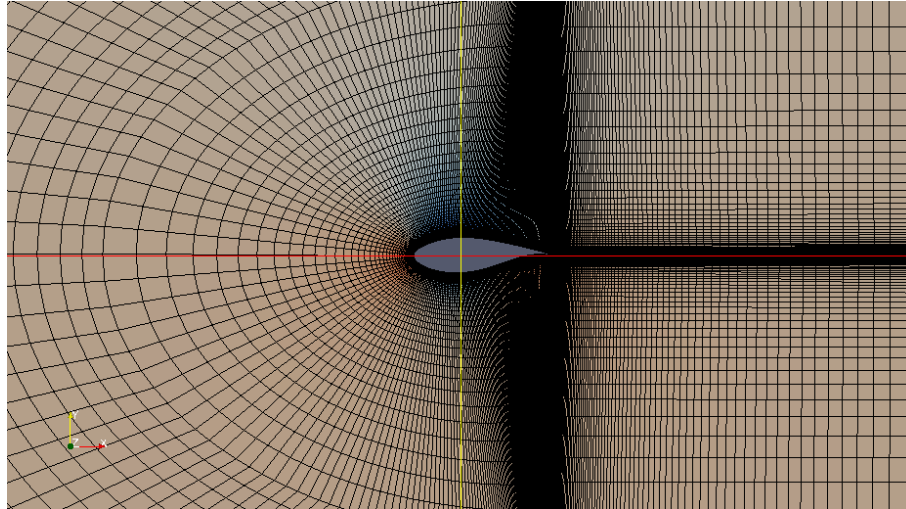
5.2 2D Set Up

The mesh and blade design were performed at Uppsala University using Gambit 2.3 while the simulations were performed on Fluent 6.3. The post-processing of the results was done in Fluent and Paraview, the latter used to produce the visualizations found in this and the next chapter with the exception of the raytraced renderings, which were performed using Blender.

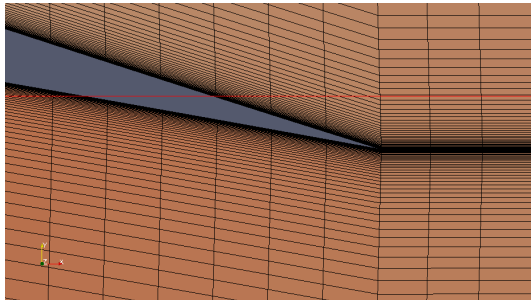
The 2D mesh used is a C-H shaped grid which gives the advantage of a good resolution at the wake region of the blade. The Proudman/Lilley approach has been used as the numerical acoustic solver and thus it is of particular importance to resolve the turbulence properties within a good approximation. The most acoustically important turbulent contributions are expected to occur in this wake area, thus supposing the need for this finer mesh. A detail of the mesh can be seen in Figure 5.4.

A good resolution has been chosen at the blade boundary layer that reaches a 5.0×10^{-5} first to second row ratio with a 1.1 growth ratio. This has yielded y^+ values between 0 and 1 in the

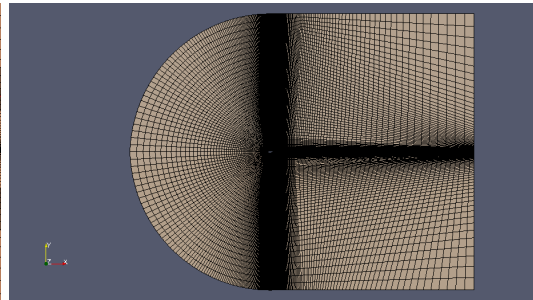
Characteristics	
Cells	70950
Faces	142704
Nodes	71754

Table 5.1: 2D mesh characteristics.

(a) Close up on blade



(b) Close up on trailing edge



(c) Whole numerical domain

Figure 5.4: 2D mesh details

simulations¹, as is recommended (*Fluent 6.3, User's Guide 2006*). The rest of the domain shows a progressive growth until reaching a maximum size of one chord length. The boundaries are situated at 20 chords in the x_- direction, 30 chords in the x_+ , and 20 chords in the y direction. A structured grid has been chosen since it may help reduce the time needed to reach a stable solution, in comparison to an unstructured grid. The characteristics of the mesh are found in Table 5.1.

As it was mentioned before, the Proudman/Lilley approach² was used, therefore allowing the use of a steady state RANS turbulence model. For this simulation the so-called realizable $k-\varepsilon$ model was chosen with enhanced wall treatment and run as a double precision density based implicit model with a second order upwind scheme. In this case, the density based solver faired faster convergence results compared to the pressure based solver, having in the 2D geometry the

¹The value y^+ is known as the dimensionless wall distance. See Appendix A.2.

²This method is referred to in Fluent as the "Broadband Noise Sources" model.

added advantage that, while this solver needs approximately double the amount of memory to run, the case was small enough to fit in the available hardware.

The Ffowcs-Williams and Hawkings acoustic model, which is also available in Fluent, was also tested with different parameters than those described above, yet it didn't yield the expected results. Further research into it wasn't pursued as the overall solution time seemed impractical when considering the requirements that the 3D model would later impose. The main difference between it and the Broadband Noise Sources model is that it needs a transient solution while the latter only requires the statistical turbulence results as achieved by a steady state solution. The output of Ffowcs-Williams and Hawkings does offer more information in the sense that the acoustic power levels are represented in their frequency spectrum form. The procedure requires the user to specify a number of points in or outside the numerical domain which are called receptors and are analogous to microphones. On the other hand, the broadband model offers an acoustic power level data set over all the numerical domain showing where noise is being produced and at what level. Both approaches offer a great quantity of value in this particular study, yet, having to choose a more efficient method in terms of run-time and considering that trailing edge noise can be regarded as having a broadband nature in the case of wind turbines and not tonal as could be the case in jet engine noise generation, the broadband noise model was ultimately chosen.

The outer edges of the numerical domain represent far-field boundary conditions with a 0.15 Mach number flow speed while the blade boundary has been defined as a wall. With a chord length of $L = 1.5$ m, the Reynolds number of the case was set at 5.13×10^6 with $\mu = 1.79 \times 10^{-5}$ Pa · s and $\rho = 1.175629$ kg/m³, calculated as

$$\text{Re} = \rho \frac{LU_\infty}{\mu}$$

where U_∞ is the free stream flow velocity, calculated from the Mach number as

$$\text{Ma} = U_\infty/c$$

for c the speed of sound in this medium. For a simulated pressure of 101325 Pa the resulting free stream velocity is approximately $U_\infty = 51.8$ m/s at a temperature of 300 K. The given values for Mach and Reynolds numbers were recommended by LM Wind Power as being within the range of this blade's typical operating conditions. The results of the simulations run under these conditions shall be covered in the next chapter.

5.3 3D Set Up

The 3D blade was constructed from the 2D geometry dataset provided by LM Wind Power which in turn was slightly modified to fit a sharp trailing edge. This 2D geometry was extruded into the z axis and an appropriate grid was constructed around it.

The chief concern when dealing with the 3D geometry in this research was to optimize the simulation to fit the available hardware resources and still achieve a valid solution. The simulations were run on a system with approximately 3.5 GB of total memory, of which some 80% of it was allocatable for use. The resolution of the mesh was limited by this resource and, along with the meshing strategy, other parameters were also considered to optimize the running of the simulations for this research. The general size of the numerical domain was reduced in comparison to the 2D case. In the 3D simulations the domain extends 10 chord lengths into the x_- , y_+ and y_- direction, and 30 chord lengths into the x_+ direction to allow a proper diffusion of the turbulent region into the main flow. Figure 5.5 shows a view of the numerical domains for the three simulated geometries.

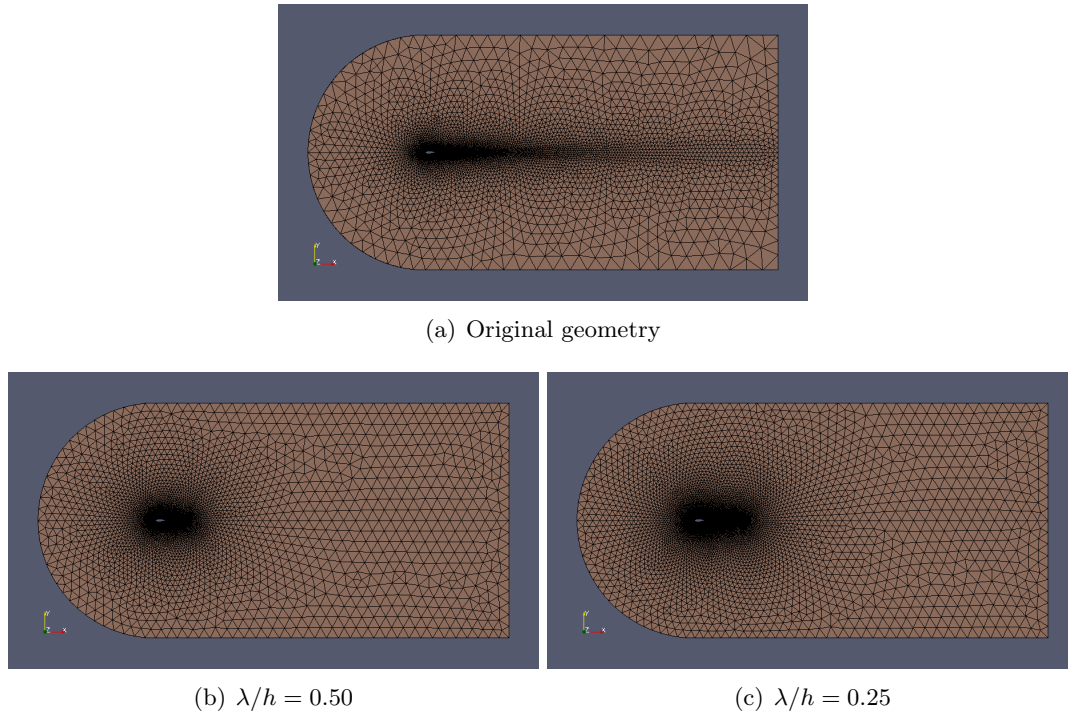


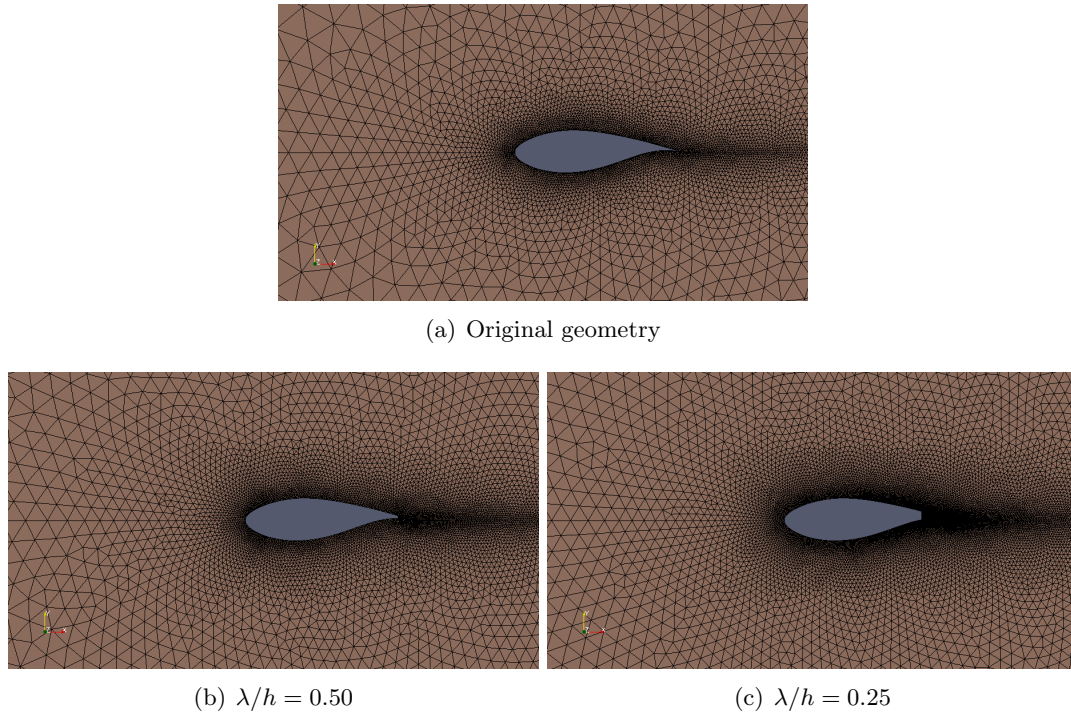
Figure 5.5: 3D mesh, view of the full numerical domain

The domain was built by constructing two volumes around the aerofoil with a flat horizontal interface between them that originates from the leading and trailing edge of the blade and serves to control the mesh growth and in turn allow to concentrate more nodes around the wake area. A growth function was used to control the allocation of nodes in the rest of the domain. It was impossible to achieve the same level of resolution near the boundary layer as in the 2D case and, instead of pursuing a range of $0 < y^+ < 1$, the aim was to achieve $30 < y^+ < 500$, as recommended (*Fluent 6.3, User's Guide 2006*). A close up of the blades' grids can be seen in Figure 5.6.

As it can be observed in these figures, the sides of the volume were meshed using an unstructured triangular grid in all cases. In Figure 5.7 the meshing of the aerofoil faces is detailed. For the original geometry, an unstructured triangular grid was used while, in the serrated cases, a quadrilateral grid was used instead to try to reduce the total number of nodes used.

Each case brought up important insight on how the simulations were behaving and helped find a better meshing strategy for the next. It can be seen in Figure 5.5, for example, that the original geometry case has a larger number of nodes in the wake of the blade while in the serrated blade cases it was decided to concentrate more nodes in regions closer to the trailing edge, as it's visible in Figure 5.6. Also there is an important number of nodes that had to be reserved for the inside sections of the serrations as these are complex aerodynamic structures and the information gathered from them is the critical to this research. In the 0.25 serration ratio case, the geometry poses a particular difficulty in the sense that the shape of the serrations contains several very sharp corners. To ease the meshing task, it was decided to cut off a small section (around 0.01% the chord length) of these inner corners and the serration extensions. A visualization of this can be seen in Figure 5.8. This modification effectively improved the mesh quality in the volume regions of the serrations while the solution is not expected to diverge by any noticeable amount in comparison to having sharp edges as in the 0.50 serration ratio case.

Further modifications on the mesh were performed during the running of the simulation

**Figure 5.6:** 3D mesh blade close up

	Geometry		
	Original	$\lambda/h = 0.50$	$\lambda/h = 0.25$
Cells	372206	846903	2058431
	1913914	2267854	2574644
Faces	783904	1731289	4191296
	4306529	5003039	5419733
Nodes	82987	160715	382351
	564953	620198	579333

Table 5.2: 3D mesh characteristics. The first line contains values for the initial mesh and the second line contains them for the final mesh refined with Fluent's adaptation tool.

by using Fluent's mesh adaptation tool on sectors of high gradients. Pressure and different turbulence variables were used as parameters at different points during the simulation until a satisfactory convergence of residuals and a levelling out of the lift and drag coefficients was observed. More on this shall be presented in the next chapter.

The mesh characteristics can be seen in Table 5.2, which compares the initial mesh with the final mesh after having refined it with Fluent's adaptation tool and shows a large difference between the two in some cases. Adaptation allowed for the refinement of results only in sections where it mattered the most, especially those of complicated aerodynamics such as around the serrations, and also sped up the total simulation run time by having the first iterations run on a model containing considerably less nodes.

The boundary conditions are the same as in the 2D case but now a thin boundary surrounding the large faces seen in Figure 5.5 handles the far-field boundary condition. These faces, placed

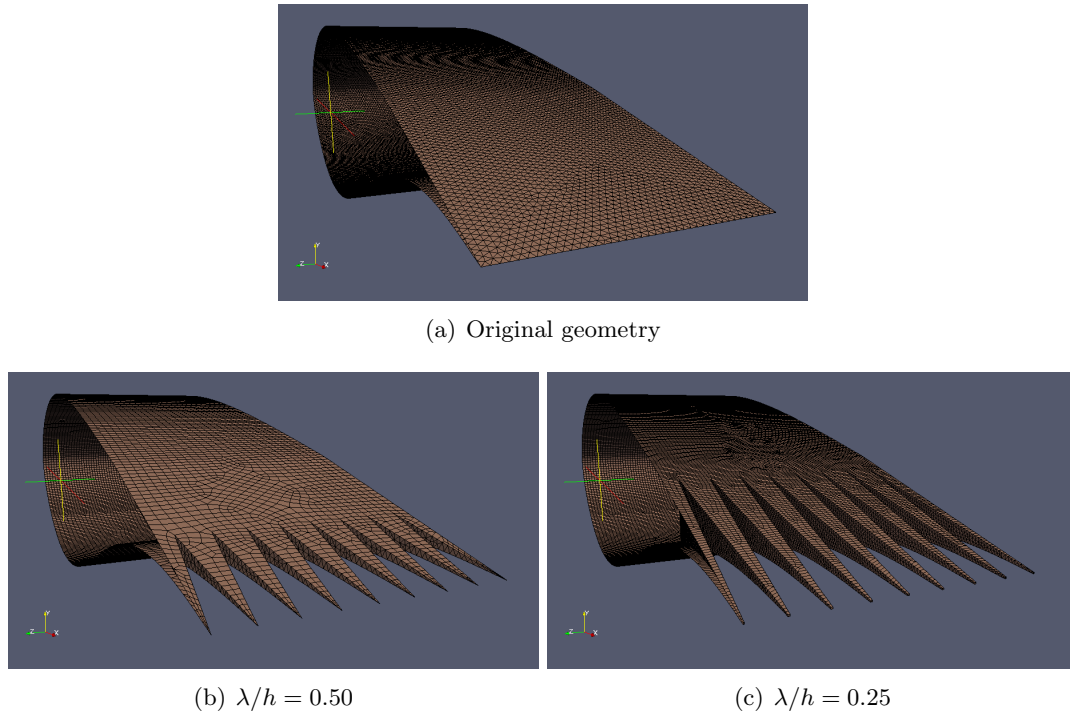


Figure 5.7: 3D mesh close up on trailing edges.

on the x - y plane, were set up as symmetry type boundary conditions since the case is handling only a small section of the blade and can be thought of repeating itself beyond the z axis limits. A real-life scenario could differ in this sense because the flow's velocity could present a radial component, while in this case it is thought to be perfectly perpendicular to the blade. In order to model such a behaviour, either a full scale model with rotating blades would have to be constructed or have measured very detailed field data in order to handle this case with enough realism. Non the less, both options are impractical at the moment and the radial velocity can be thought to be small enough to not cause too much deviation from the reached solution. Despite of this, if the radial component were to be significant it could be an important factor since the optimal shape of the serrations is thought to depend on the incoming flow's direction and, if they were encountered at a significantly different angle, they could lose their effectiveness or even lead to an increase in the noise produced by the blade.

The solver settings of the 3D case remain similar to those used in the 2D case. A summary of them can be seen in Table 5.3. The main difference is the use of a pressure-based solver instead of the density-based one used in the 2D case. As it was mentioned before, the latter is an implicit method which uses up as much as double the memory as the former—used in its explicit form. If the density based solver was applied in the 3D simulations, it would seriously limit the resolution of the grid. It is stated in (*Fluent 6.3, User's Guide 2006*) that, although previously a difference between both methods made them useful in only different cases, advancements in the code used in Fluent have allowed users to freely chose between them without losing validity in the solution. The key mathematical properties of the two are:

Density based The continuity equation is used to obtain the density field while the pressure field is determined from the equation of state. It is typically used for compressible flows.

Pressure based The pressure field is extracted by solving a pressure correction equation which is in turn obtained by manipulating the continuity and momentum equations. It is typically

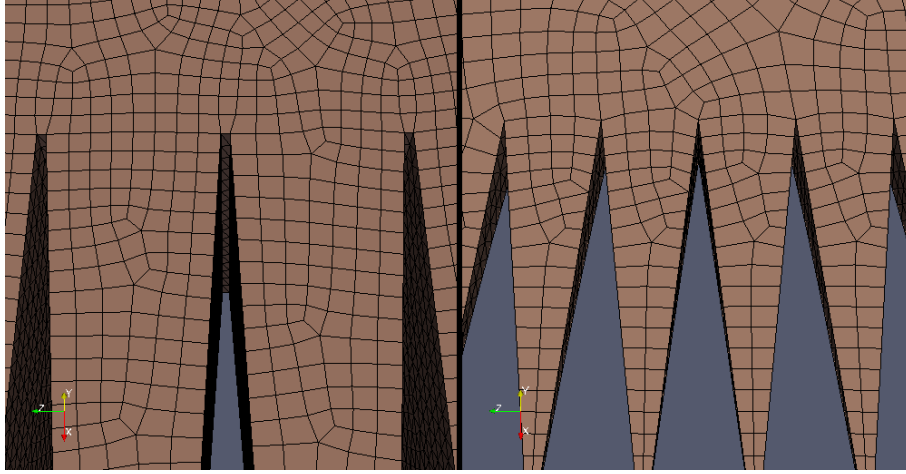


Figure 5.8: Comparison of the handling of the serration's inner edges of the 0.25 and 0.50 serration ratio geometries, respectively.

Parameter	Value
Precision	Double precision
Solver	Pressure-based
Time	Steady state
Viscous model	Realizable $k-\varepsilon$ turbulence model
Wall treatment	Enhanced wall treatment
Heat transfer	Enabled
Equations solved	Flow / turbulence / energy
Pressure-velocity coupling	SIMPLE
Discretization scheme	Second order upwind for all parameters

Table 5.3: Solver settings for the 3D simulations

used in incompressible or low compressibility flows.

In both cases the velocity field is obtained from the momentum equations.

The enhanced wall treatment option is turned on for the $k-\varepsilon$ turbulence model to aid in the solution of the boundary layer near the blade's surface. This method works by choosing between a two-layer model if near-wall meshes are fine enough to resolve the laminar sublayer and using enhanced wall functions if the mesh is too coarse in this region. In the current 3D model the solver will typically encounter the latter case as the boundary layer was impossible to resolve as finely as in the 2D case without using an impractical large number of nodes. In 2D, where the boundary layer *has* a very fine mesh, the solver will instead most likely use the two-layer model in the vast majority of the region close to the blade. The grid adaptation tool was used extensively to fine-tune the mesh size near the blade to appropriate y^+ values.

The wind turbines that are fitted with this blade model have variable pitch control and for this simulation a 6° angle of attack (AOA) was chosen, a value which was also recommended by LM Wind Power as being typically encountered in operating conditions. The Mach number was set at 0.15 and 5.13×10^6 Reynolds number. This, as in the 2D case, yields a mean stream velocity of $U_\infty = 51.8$ m/s. Other parameters are the same as in the 2D case and are presented in Table 5.4. The density has been defined by the ideal gas law for an incompressible flow and

Parameter	Value
Main stream velocity	51.8 m/s
Reynolds number	5.13×10^6
Mach number	0.15
Pressure	101325 Pa
Temperature	300 K
Density	1.175629 kg/m^3
Viscosity	$1.79 \times 10^{-5} \text{ Pa} \cdot \text{s}$
Characteristic length	1.5 m
Angle of attack	6.0°

Table 5.4: Simulation conditions

is calculated by Fluent as

$$\rho = \frac{p_{\text{op}}}{RT/M_w}$$

where R is the universal gas constant, T is the temperature, M_w is the molecular weight of the gas and p_{op} is the given operating pressure of the case. The viscosity is calculated through Sutherland's viscosity law which uses an idealized intermolecular-force potential. It's given by

$$\mu = \frac{C_1 T^{3/2}}{T + C_2}$$

where C_1 and C_2 are coefficients given as $C_1 = 1.458 \times 10^{-6} \text{ kg/m} \cdot \text{s} \cdot \text{K}^{1/2}$ and $C_2 = 110.4 \text{ K}$ for air at moderate temperatures and pressures.

SIMULATIONS AND RESULTS

6.1 The 2D Case

The 2D simulations performed in this research were used as test beds for the 3D simulations that were to be carried out later. Several turbulence models, solvers, acoustic settings, grid requirements and other parameters were compared in order to find a series of settings that would give a faster convergence and a good solution while optimizing computational expense.

Initially, the intent had been to study the blade's acoustic profile using the FW-H model, which requires an unsteady solution to be modelled and, although it allows for the use of a lighter one-variable turbulence model, ultimately the required time to reach a reasonable acoustic solution was too large especially considering that it should be extrapolated to the much more expensive 3D model.

The time requirements for the unsteady solution are

$$\begin{aligned}\Delta t &= 10^{-1} \frac{1}{f_{\max}} \\ T &= 10 \frac{1}{f_{\min}}\end{aligned}$$

where Δt is the simulation time step, T is the final simulation time, f_{\max} is the maximum sound frequency that is desired to be modelled and f_{\min} is the minimum frequency (Sovani 2005). Following this rule, if one wanted to simulate for $f_{\max} = 10$ kHz and $f_{\min} = 20$ Hz, which represents just the lower half of the average human audible range, then $\Delta t = 1 \times 10^{-5}$ s and $T = 0.5$ s, meaning that the simulation would have to run for 50000 time steps (each of which may involve an unspecified number of iterations). Furthermore, there is a considerable overhead since the typical procedure for running an unsteady simulation involves achieving convergence through a steady-state simulation before starting to advance in time. Unfortunately, these goals are unobtainable with the computational capabilities that were available for this research so, considering that the simulations would later have to be run on the 3D geometries, an alternative model was needed.

This second option was chosen to be the Proudman/Lilley approach to sound modelling, called "Broadband Noise Sources" in Fluent. It's a method that, as it was reviewed in section 3.3, requires data obtained from a steady-state solution to calculate noise generation. With Proudman/Lilley, the acoustic power, P_A , is solved as a function of the turbulence viscosity ratio, ε , and the turbulence kinetic energy, k , as seen in equation (3.14), both of which are values that are readily available from the RANS k - ε turbulence model. This method's most noticeable difference with FW-H is that, instead of calculating the source's acoustic frequency spectrum at specified receiver locations in space, it calculates the acoustic power measured per

	Angle of Attack	
	1°	6°
C_l	0.5476	1.1198
C_d	0.0124	0.0161

Table 6.1: Lift and drag coefficients found for the 2D simulations

unit volume (with units $[\text{W}/\text{m}^3]$). The resulting solution is an acoustic power data cloud of the numerical domain. So, although one may lose the ability to study the frequency spectrum profile of a certain source—something which can only be achieved under rather computationally demanding conditions—an important insight on where and with what amount of power noise is being produced is achieved using relatively inexpensive steady-state methods. This is particularly useful in cases where the sound being produced is expected to be of a broadband nature, i.e. it's spread out more evenly over the whole frequency spectrum, opposite of being tonal which would show notable maximums in one or several ranges of the spectrum.

Fortunately, as seen earlier in Figure 4.10, the conditions under which a wind turbine normally operates cause its blades to produce noise in a mostly broadband character with the lower frequencies having only a slightly higher acoustic power level than higher frequencies. Nonetheless, it will be seen later that an alternate mean to approaching acoustic frequency is ultimately required to achieve a full picture of how serrations affect sound and that just a study of ε and k based acoustic power level is not enough. Furthermore, the study of the full frequency spectrum sound generation by wind turbine blades through the use of FW-H and high accuracy turbulent model numerical methods should not be neglected if the computational power is available.

Considering the requirements of the Proudman/Lilley method, as proposed in (Lilley 1994), one is recommended to apply it to low Mach and high Reynolds number conditions. In the current research, a Reynolds number of 5.13×10^6 is used and 0.15 Mach, values which somehow fit into this requirement but, although (*Fluent 6.3, User's Guide 2006*) does cite certain Mach number limitation, the method is known to have been used in previous, higher Mach studies such as (Khondge, Sovani, Kim, Guzy and Farag 2005), (Horváth and Vad 2009), (Dozolme, Metwally and Marchal 2006) and (Patidar 2009).

For the purpose of this thesis, the 2D simulations were performed at 2 angles of attack (AOA), $\alpha_1 = 1.0^\circ$ and $\alpha_2 = 6.0^\circ$, to study the blade's behaviour and the effect that the AOA has on sound generation. The Reynolds number used to conduct the simulations was chosen so that it modelled the low end of the blade's operating conditions, and thus allowing for the boundary layer resolution requirements to be alleviated as much as possible. The lift and drag coefficients, C_l and C_d , respectively, that were found with the simulations are presented in Table 6.1 and the pressure profiles on the blade surface for both AOA's can be seen in Figure 6.1. Figure 6.2 shows an overlay of pressure contours for both AOA's and Figure 6.3 shows the flow streamlines in the $\alpha = 6^\circ$ case.

Concerning the acoustics results of the 2D simulations, it was found that, from an acoustic intensity per volume analysis based on the Broadband Noise Sources model, the larger AOA case does seem to generate sound with higher intensity than at lower AOA's. As seen in Section 3.3, equation (3.14), the Proudman/Lilley model solves acoustic power, P_A or ASP, per volume, in terms of k and ε . In Figure 6.4 an ASP colour representation around the aerofoil has been constructed for both AOA cases. Even though the ASP has values of up to 110 dB in regions that are very close to the aerofoil, it has been clipped to a range of $[0, 70]$ dB to improve the detail on more important regions (in the present case, higher values compromise very small regions and thus have a small contribution to the total sound intensity). Two contours have been highlighted with values of 55 dB and 50 dB.

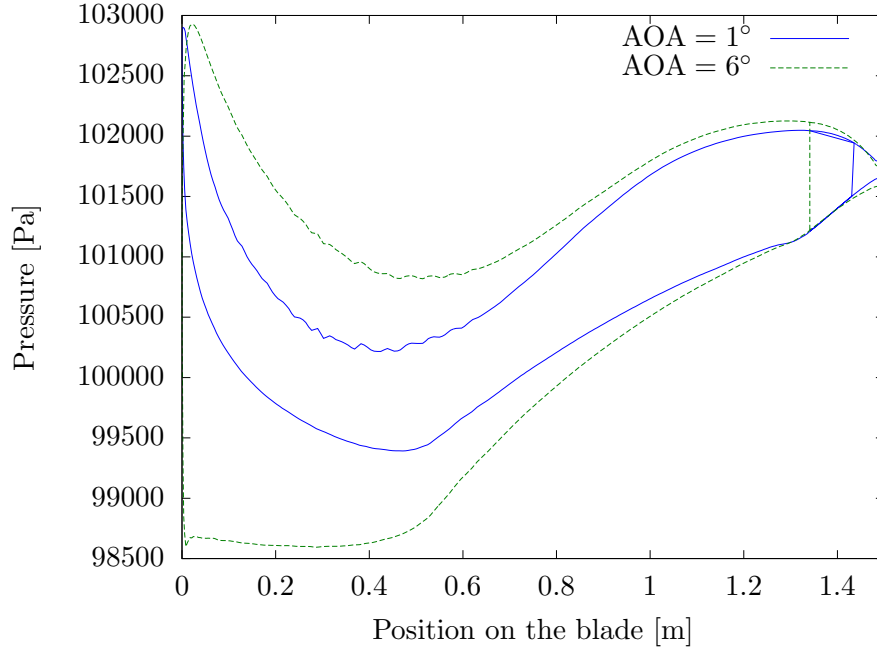


Figure 6.1: Pressure profiles for the 2D cases

Several characteristics can be observed from this visualization:

- First, the sound *is* being generated mainly from the trailing edge part of the blade, as it has been assumed so far that it would. The blade is seen to leave a wake behind it of decreasing sound level.
- Secondly, the higher AOA case shows a lag in sound level decrease, easily seen from the larger size of the 55 dB and 50 dB contours. This means that higher ASP level regions now occupy more area behind the blade, thus contributing more to the overall sound level. Figure 6.5 highlights the area difference between same ASP levels in both AOA's.
- Thirdly, in the 6° case, a larger region of higher ASP can be seen on the suction (upper) part of the trailing edge. It must be noted that sound from one side of the blade will have minimal contribution in the direction of the opposite side since the blade itself will behave as an insulator while at the same time function as an reflection surface operating in its own direction. From this fact, it can then also be assumed that this larger and more intense ASP region on the suction side could increase sound through directivity to an observer standing in that direction. The suction side of the blade points towards the downwind part of the wind turbine.

The amount of partial contribution this factor adds to the total noise generation is unclear yet, in an LES study done on a NACA-0018 blade at $\alpha = 6^\circ$, a slighter higher noise level was found for measurements taken at angles of up to 60° above the downwind direction compared to those taken below it (Kim, Lee and Fujisawa 2006). See Figure 6.6. This asymmetry may be a result of the aforementioned observation.

So far, an insight on sound level generation has been given with aid from the Proudman/Lilley model but it will be seen later that sound level intensity itself cannot not describe sound generation with enough completeness to form a clear analysis into how serrations will change its

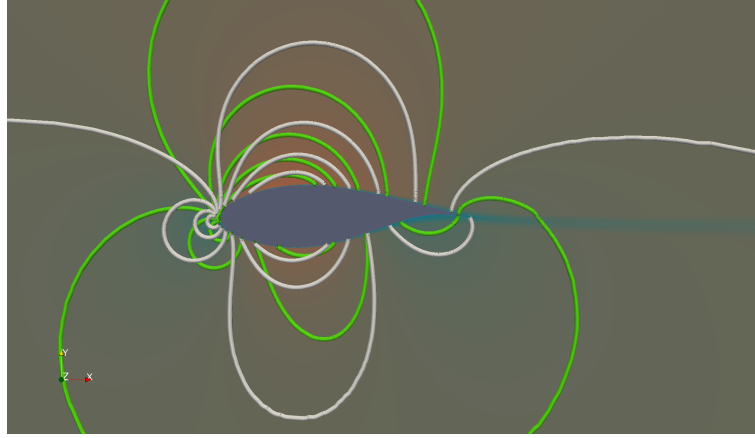


Figure 6.2: Comparison of pressure contours for $\alpha = 1^\circ$ (white) and $\alpha = 6^\circ$ (green).

characteristics. Because of this reason, a supporting analysis will be carried out concerning the length scale properties of the eddies shed by the blade.

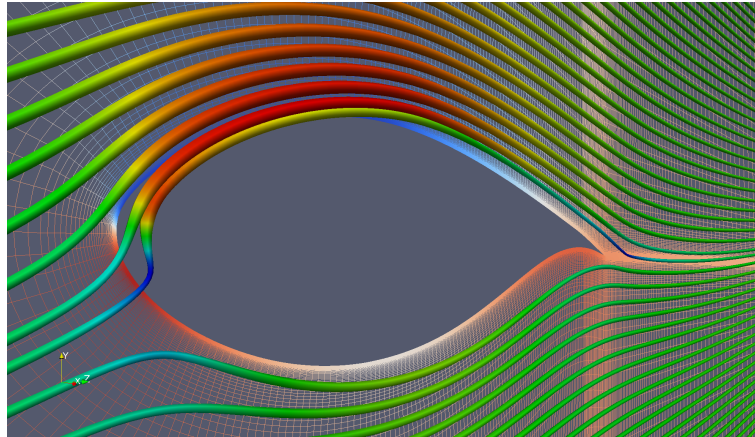
It is known that a turbulent eddy of turbulence length scale, TLS, $l' = 2\pi/k_T$, will generate acoustic frequencies in the order of u_k/l' where u_k is the velocity perturbation of the eddy k_T (Stein 1967). Furthermore, TLS values can be approximated, for the k - ε turbulence model used here, by

$$l' = C_\mu \frac{k^{3/2}}{\varepsilon}$$

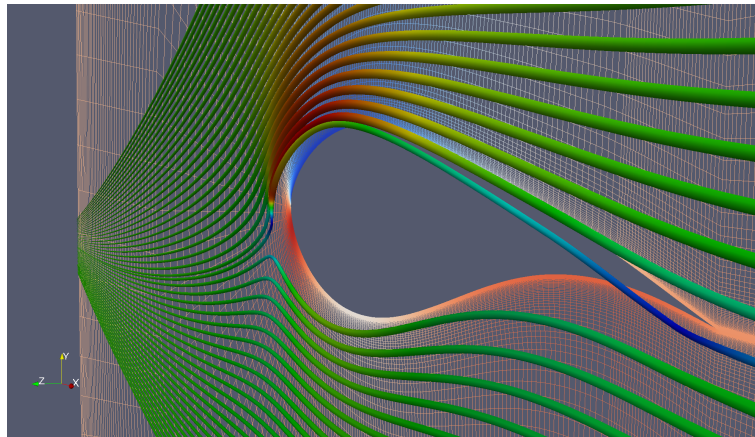
where C_μ is a constant usually taken to be $C_\mu = 0.09$ (Shih 1990). Given this, l' can easily be calculated from the simulation CFD results and regions with different TLS values can be extracted from the flow field. Expecting that u_k remains relatively constant, the frequency of sound can be assumed to be inversely proportional to l' , such that higher l' it will emit a lower pitched sound.

In Figure 6.7, different TLS regions are visualized. The colour scale has been roughened to only show 5 values from 1.0×10^5 to 1.0×10^2 to aid in readability. The region with smaller TLS values, here represented in red, will emit higher pitched sound compared to lower TLS regions such as those represented in green. The importance of this analysis lies in that the increased lower TLS valued regions for the $\alpha = 6^\circ$ case in comparison to the $\alpha = 1^\circ$ case. In addition to these areas being more prominent, they also lie in higher APL regions. In the same figure two APL contours have been highlighted, the 55 dB and 45 dB levels, and, as it can be observed, in the low AOA case, TLS regions of around 5.0×10^3 breach only slightly the 45 dB contour, while in the higher AOA case the same region goes well beyond even the 55 dB region.

This result supposes that, at higher AOA's, the blade will emit more sound but also in a lower frequency due to the shedding of larger scale eddies. To support this claim, studies done in, for example, (Hutcheson and Brooks 2006), predict that at an AOA of 8.8° has an APL of around 6 dB higher at frequencies of about 300 Hz than compared to a blade at 3.8° AOA. The difference evens out at around 1 kHz. This experimental study involved a NACA 63-215 aerofoil of 0.40 m chord length at $Ma = 0.17$ with a sharp trailing edge.



(a) View from the leading edge



(b) View from the trailing edge

Figure 6.3: Flow and pressure results for $\alpha = 6^\circ$. The flow field is visualized as velocity magnitude varying streamlines over a pressure scaled grid visualization in the background.

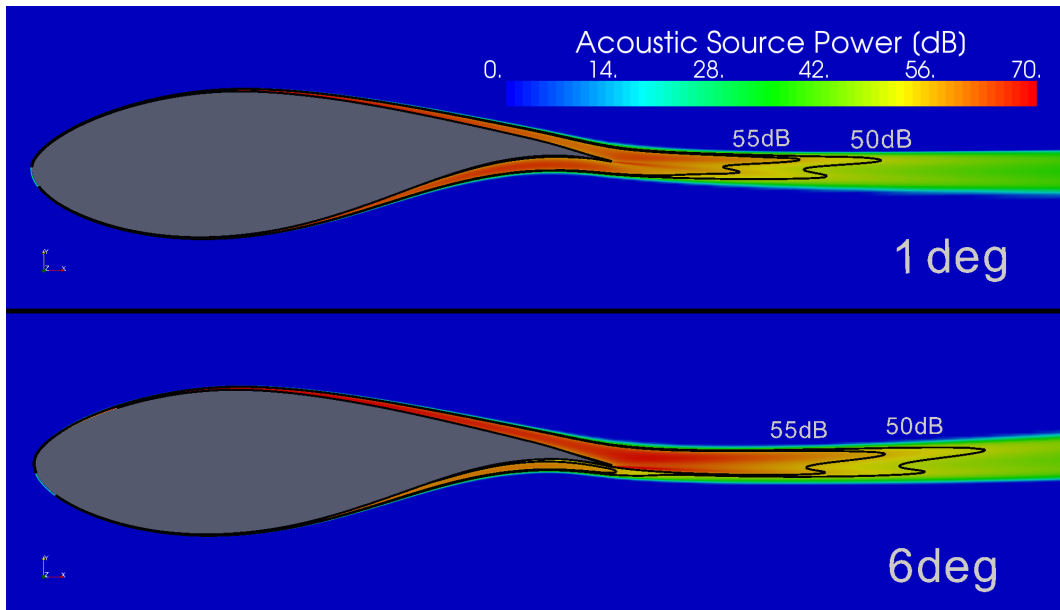


Figure 6.4: Acoustic results from the 2D simulations comparing both AOA's. The colour scale represents acoustic power source per unit volume measured in the numerical domain by the Proudman/Lilley model.

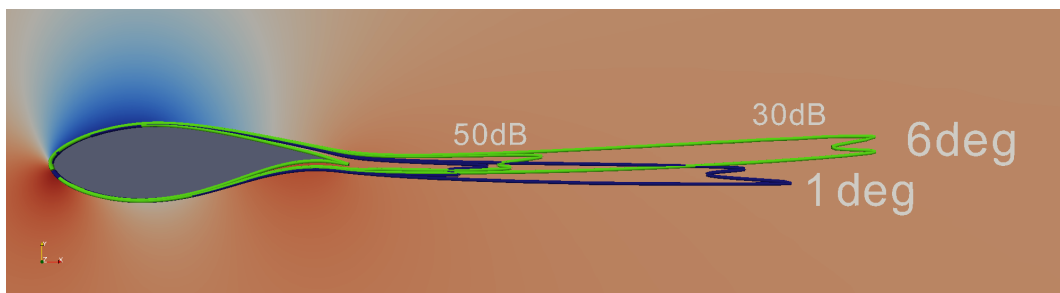


Figure 6.5: Two acoustic source power contours for both AOA's showing a larger swept area by the 6° AOA case.

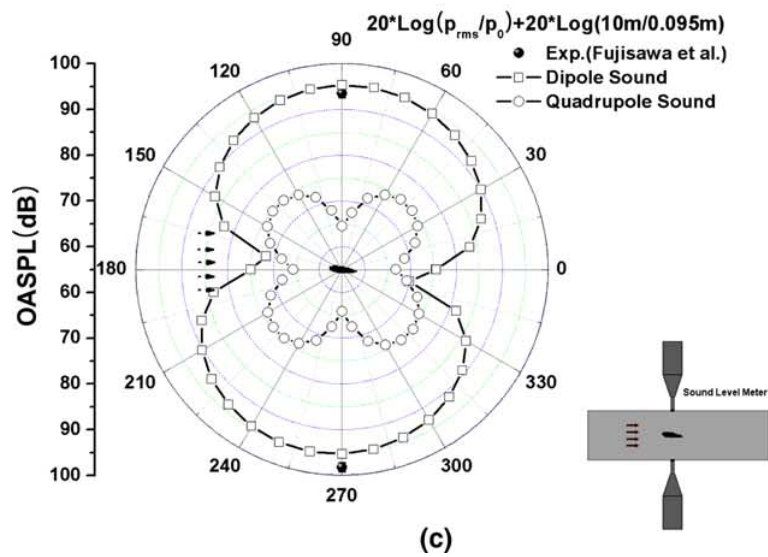


Figure 6.6: Sound radiation found for a NACA-0018 aerofoil at $\alpha = 6^\circ$ through LES (Kim et al. 2006).

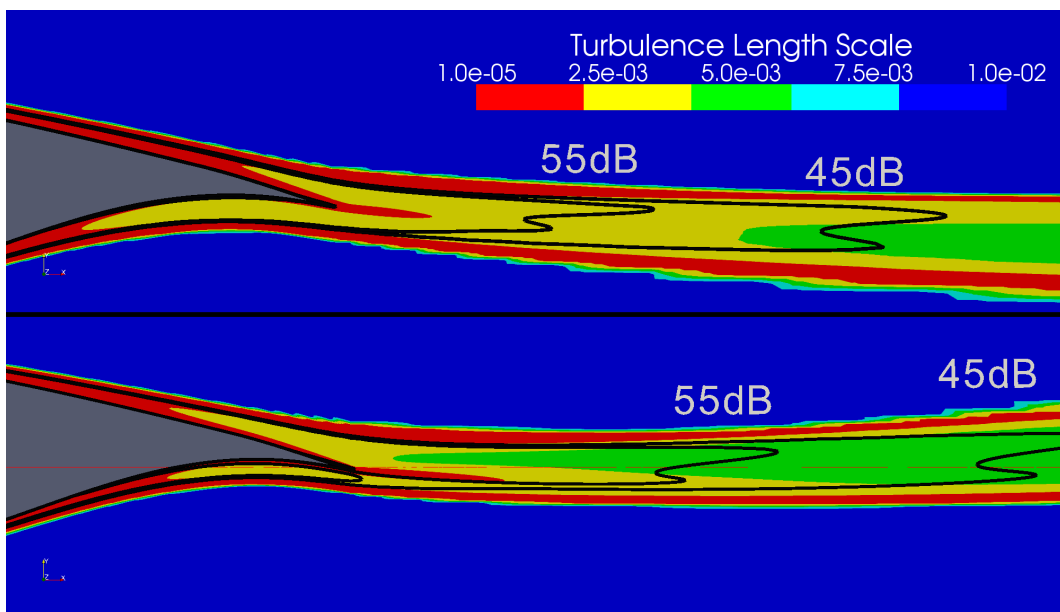


Figure 6.7: Comparison of turbulent length scale regions for the two AOA's that were simulated ($\alpha = 1^\circ$ on top and $\alpha = 6^\circ$ on the bottom).

	Geometry		
	Original	$\lambda/h = 0.50$	$\lambda/h = 0.25$
C_l	1.1276	0.7933	0.5266
C_d	0.0097	0.0249	0.0204

Table 6.2: Lift and drag coefficients for the 3D simulations.

6.2 The 3D Case

As mentioned above, the 3D case studied for this research was run on a $Re = 5.13 \times 10^6$, $Ma = 0.15$ simulation (same as in the 2D case) for a single AOA of $\alpha = 6^\circ$. Each of the three geometries were run on an initial grid, as specified in Table 5.2, which emphasized resolution on the wake region. Initially, a first order scheme was used for a few hundred iterations to attempt a faster convergence, and then changed to second order schemes. Progressively the mesh was adapted to increase resolution on areas of interest, especially concerning pressure and several turbulence parameters. The end of the runs was chosen by an evening out of the C_l and C_d values, coupled with a moderately relaxed overall parameter convergence (below a 10^{-4} ratio).

Lift and drag coefficient results can be seen in Table 6.2 where, for the original geometry, there is a good agreement with the 2D case for the same AOA. The blade geometries for which serrations were cut experience a very sharp and expected decrease in efficiency from the original blade. This is expected because the serrations were made from the body of the blade itself by removing relatively large sections in the trailing edge. The reduced blade area will impose a clear penalty on lift, but also the big design shift from an already optimized blade will pay its toll.

Pressure profiles for the serrated blades, seen in Figure 6.8, vary greatly at the trailing edge section and experience an evident difference in pressure along the rest of their length, showing the $\lambda/h = 0.25$ serration case to be the most affected. It can be assumed at this point that it is highly recommended to pursue a different serration design. Aside from the evident lift efficiency penalty this design has, it also involves a modification on the current blade design that could make them much more vulnerable to mechanic failure due to the complex geometry and introduction of weak spots on structurally important sections of the blade. In addition, it would be ideal to use a design which would allow for currently installed blades to be retrofitted instead of replaced. The most obvious design that would come to mind is that of a thin attachment that would fit on the trailing edge of the blade and which contains the serration geometry. A possible issue that this method brings up may concern the length that the serrations need to be efficient in noise reduction while at the same time taking into account what this added length means in terms of structural stability and aerodynamic impact.

Non the less, the decision of using the current design was taken on a few considerations. Amongst them are that the 3D model construction process seemed to be facilitated since the process involved the original model to be modified by applying boolean operations from simple geometries; namely, subtracting triangular prisms from it. Secondly, the meshing process for the current design incurred in the added concern for having a proper grid in the small spaces between the serrations, but at the same time was relieved from having an added boundary layer region and having the grid satisfy very thin structures and their surroundings (as would be the case of attaching a serrated attachment to the trailing edge). Furthermore, several parameters are involved in the selection of a design when adding a serrated attachment, such as if the original blade would be made to follow smooth contours into the newly added extension and at what angle to apply the attachment in relation to the original trailing edge and even the flow direction.

All these options offer very exciting possibilities into the optimization of serrated trailing edges but do require a vast number of cases to be considered and simulated. This fact was pro-

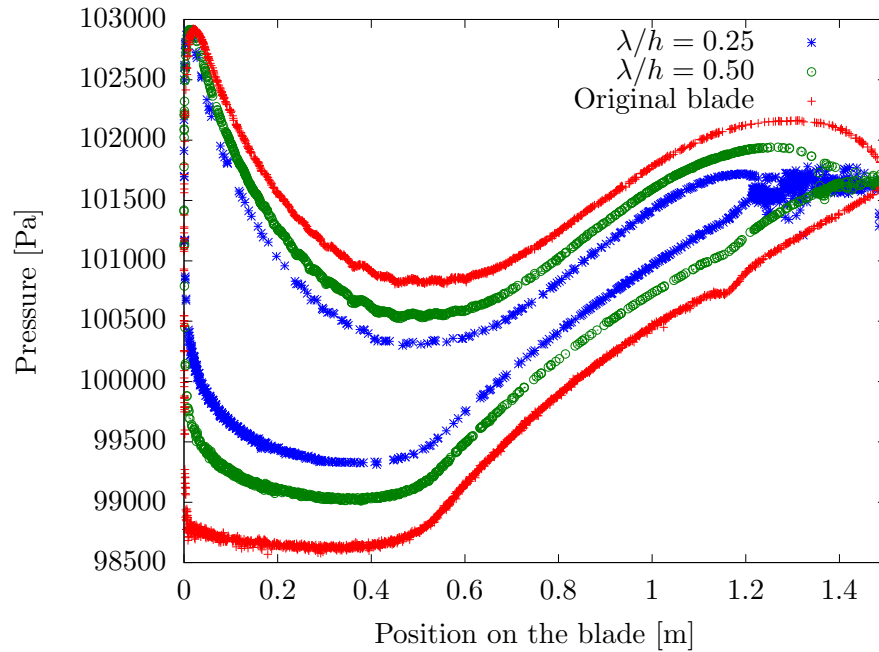


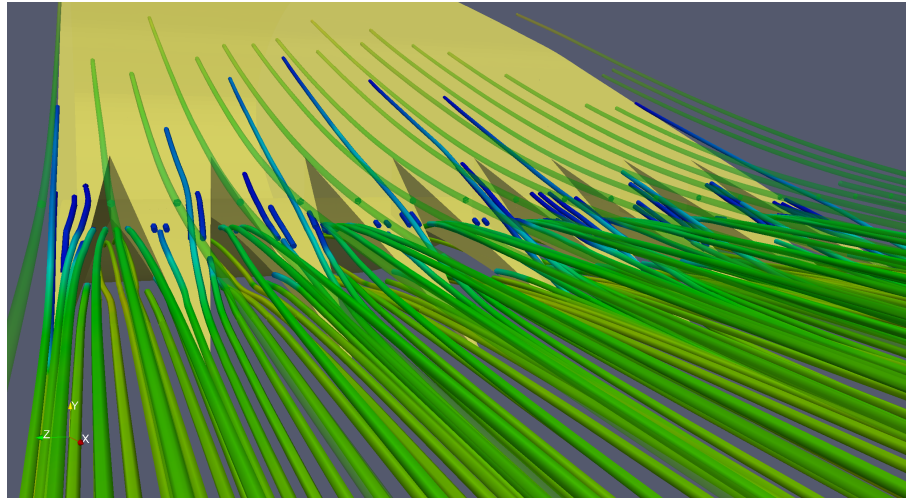
Figure 6.8: Pressure profiles for the 3D case, multiple geometries.

hibitive for this research and the number of simulations performed was limited by the constrained amount of computational power that was available. In addition, although it was predicted that the current design option would yield suboptimal lift coefficients, the results *do* offer an insight on how and how much a complicated geometry such as this one affects the blade's performance. Furthermore, comparison with later studies done with alternative designs may offer valuable insight.

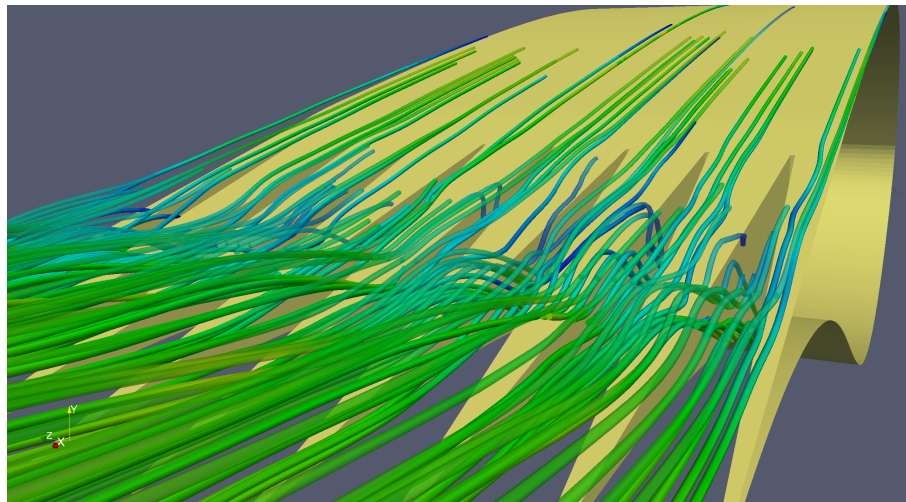
Flow around the serration structures can be seen in Figure 6.9 where the increasingly turbulent behaviour of the 0.25 serrations ratio case over the 0.50 ratio due to the serration geometry is made evident by the more complex flow of the former. Here the streamlines are coloured by velocity magnitude where blue represents lower value. In the 0.25 ratio case, the flow appears to be even travelling vertically upwards through the gaps sometimes and at varying speeds. This supposes the presence of pressure gradients in the inner regions of the structures, as seen in the case of the blade surface in Figure 6.10. In general, the surface of the serrations on both the upper and lower side of the blade, not just the inner sides, show higher pressure values than the areas right before them (on the upwind side), something that further sheds light onto where the aerodynamics are failing and causing the blade to lose so much of its lift coefficient. This factor comes as a direct result of the complex and turbulent behaviour of the air seeping through the serration gaps and interacting with the oncoming flow, interrupting it.

A turbulence intensity visualization can be seen in Figure 6.11, where two planes have been used to visualize the flow's turbulence properties when coming out from a serration crests and a valleys (outer and inner corners of the serration). In the 0.25 serration ratio case, the turbulence intensity is much higher than in the 0.50 ratio case, exhibiting oscillating properties that are particularly visible on the flow coming from the serration valley and which fit what was expected from the flow streamline details of Figure 6.9.

Acoustically, the blades seem to have results that differ from what was observed in the 2D



(a) $\lambda/h = 0.50$



(b) $\lambda/h = 0.25$

Figure 6.9: Streamlines showing flow around the serrations.

case. In Figure 6.12, the top blade shows the acoustic results for the original geometry where three ASP contour levels are shown, 25 dB, 35 dB and 45 dB. It's immediately evident, when comparing with Figure 6.4, that the noise levels have been reduced and, while in the 2D case the lowest contour that was shown had a value of 50 dB it still displayed a larger size than the lowest value observed here, which is of just 25 dB. Remembering that the ASP is calculated through Proudman/Lilley as a function of k and ε , the way the k - ε turbulence model behaves in 3D, compared to 2D, is very important in the determination of the ASP values. What is known is that turbulence, being inherently three-dimensional, may yield more accurate results in such a simulation compared to the 2D case where information may lack or be lost. From having a good aerodynamic approximation between both the 2D and 3D case, it can be supposed that the grid resolution near the blade and model parameters are well chosen, something that could otherwise influence the accurate generation of turbulence in the trailing edge and flow separation from the boundary layer. It would be suggested that, to determine the accuracy of this solution for the turbulence parameters, a series of tests be conducted, particularly in terms of grid size, to analyse the behaviour of the resulting ASP levels. Unfortunately, the allocation of such resources and time to conduct these tests is unachievable at this moment. Non the less, considering that the

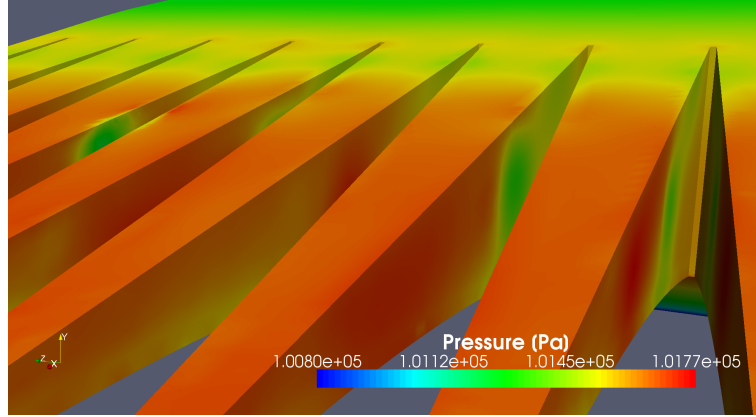


Figure 6.10: Pressure detail on the surface of the serrations' gaps and suction side of the blade.

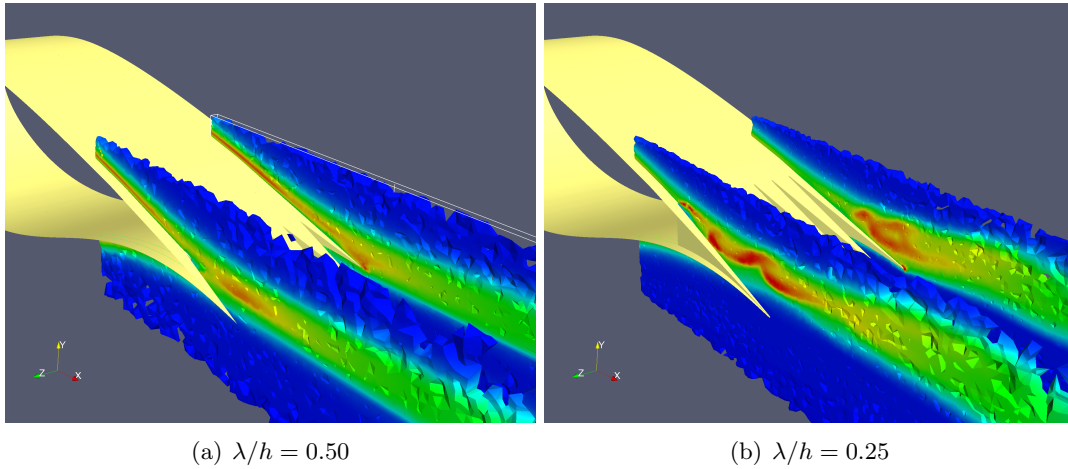


Figure 6.11: Turbulence intensity planes, located at both a serration valley and crest (front and back, respectively) on both serrated blade geometries to show the different turbulent flow that's being generated.

objective pursued is to conduct a comparative analysis between the three proposed geometries, any lack of accuracy that was to occur on one simulation will be reproduced in the others, seeing that all were meshed with keeping similar properties in mind.

In comparing the different 3D geometries, it can be observed that, although all were conducted at the same AOA, there *is* a noticeable difference between ASP behaviour. The 0.25 ratio case displays a much larger ASP volume for the same value compared to the original geometry. Compared to the 0.50 ratio blade, the levels are maintained at a similar position in the wake, with the contours of the 0.25 ratio showing slightly thicker layers. Another noticeable difference between the two blades with serrations is that the 0.25 ratio one exhibits contours that appear to be much less stable than the 0.50, showing wave-like patterns and greater variation in their thickness. In the 0.50 ratio case, on the other hand, the three contours that were extracted maintain a quite constant and straight thickness throughout their length.

From the previous analysis, it could be concluded that noise levels are actually increased by the use of this particular serration design. In reality, what can be said so far is that the Proudman/Lilley model predicts a higher acoustic source power from the presence of a more intense and unstable turbulence caused by the serrations protruding into the main flow field,

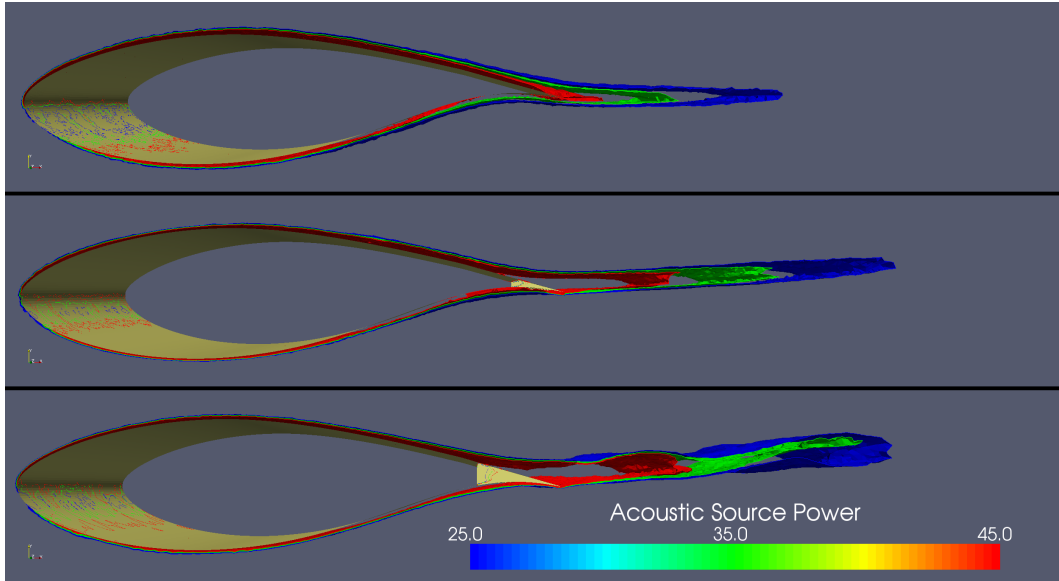


Figure 6.12: Comparison of three acoustic source power contours for the three blade geometries; the original blade at the top and the 0.50 and 0.25 serration ratio blades second and third, respectively. The ASP values extracted are 25 dB, 35 dB and 45 dB.

causing disturbances and strong interactions. This was clearly seen in Figures 6.9 and 6.11, and could be particularly enhanced in this case where a blade design with a trailing edge fitted with a downward curvature is being used and the serrations are carved into it. This trailing edge geometry puts the serrations in the way of the otherwise undisturbed flow, thus forcing it to find its way around them. When it does, and shows up on the upper side of the blade, it creates disturbances of different levels (because of the serration morphology variation itself) on the flow that's coming from the upper side of the blade. If the serrations were to be oriented *with* the flow, such a big disturbance could be averted and instead the turbulence would be given different scales by causing the boundary layer to have different time lengths to interact with the non-slip surface of the serrations. This, of course, can only be assumed until it is properly modelled and it would depend greatly on the flow transition between the blade itself and the serration geometry, amongst other factors that were mentioned above.

Considering the fact that this particular serration design has a very large impact on the turbulence behind the wake, it is important to note again that the Proudman/Lilley approach requires the flow to be mainly isotropically turbulent (meaning that turbulence has the same characteristics in all directions). The 2D case and original geometry 3D case can somehow fulfil this requirement in that the only turbulence generation structure is the trailing edge itself, thus creating a turbulent flow that remains constant lengthwise, slightly decaying chordwise into the wake, and with strong gradients just in the vertical turbulent mixing areas and boundary layer limits.

With the introduction of the serrations, turbulence in the wake has become anisotropic in the overall region thus calling for greater care when applying this method, including an expected loss of accuracy. This must be factored in the aforementioned observation in that the serration case noise now, from visualization such as in Figure 6.12, actually seems to have a greater intensity. But, again, what can only be deduced is that the turbulence-generated overall noise is larger just due to the appearance of a region of higher k and ε values, as is actually expected. Non the less, the properties of the sound that is being generated *do* escape the capabilities of the method and

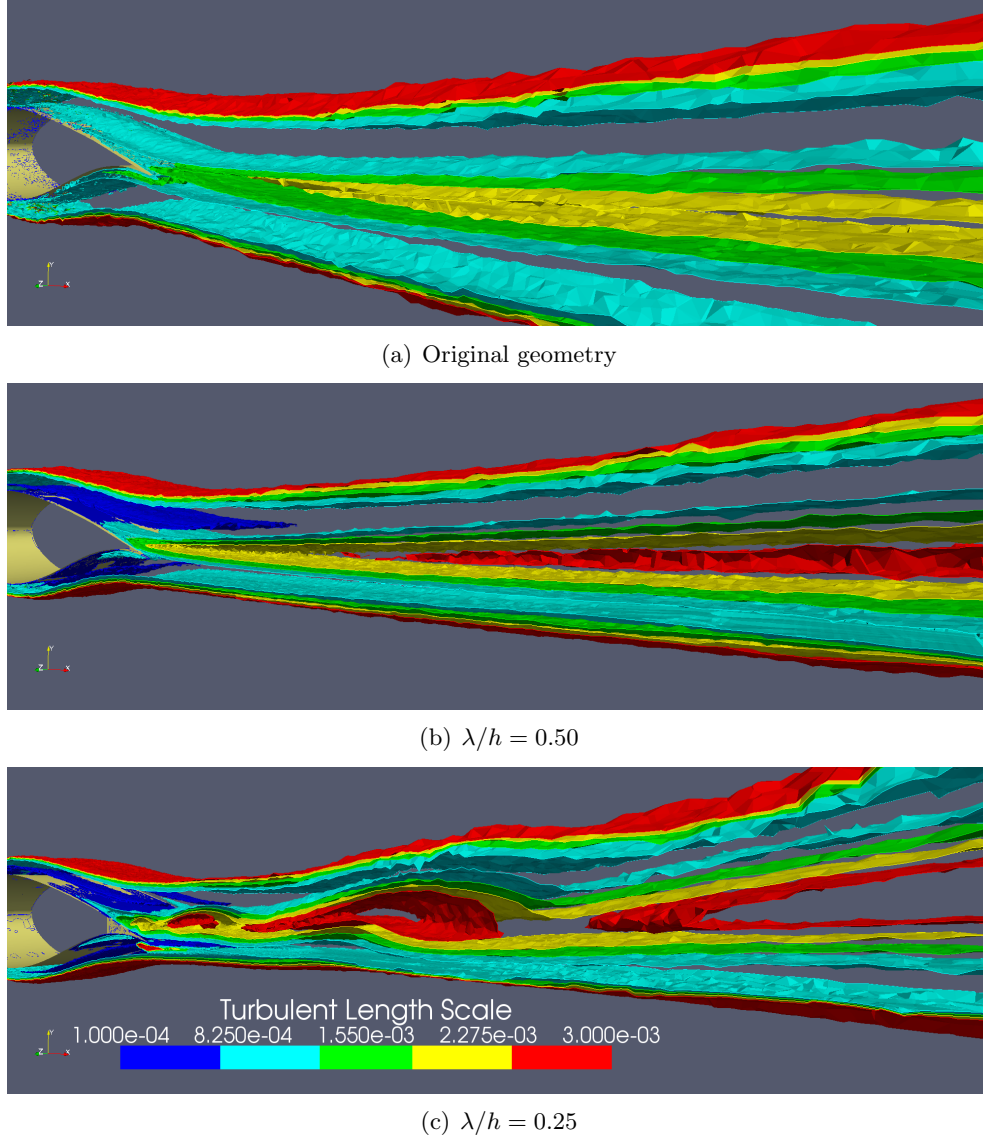


Figure 6.13: Contours of turbulent length scales.

will be approached, as it was done in the 2D case, with a turbulent length scale eddy analysis.

The turbulence anisotropy that one has to deal with now, considering this serration design, can be exemplified in Figure 6.13, where a comparison of TLS contours between the three geometries is visualized. Here blue represents turbulence of small scales and red represents turbulence of larger scales. It can easily be seen that the original geometry case contains wide TLS areas with similar, more homogeneous values ordered in a filed pattern with the contours almost parallel to each other. The larger region is contained between values of 8.25×10^{-4} , yet doesn't reach as small as 1.0×10^{-4} . The larger turbulent scales of values of around 3.0×10^{-3} are only present outside the wake area, meaning that they are not part of the trailing edge turbulent structures.

On the other hand, the 0.50 serration ratio geometry begins to exhibit a wider range of TLS values, each with slimmer, more heterogeneous regions. Even a contour value of 3.0×10^{-3} is noticed in the middle of the wake, evidencing the presence of larger eddies evolving from flow around the serrations. In the 0.25 ratio case the variations are even more evident and intense.

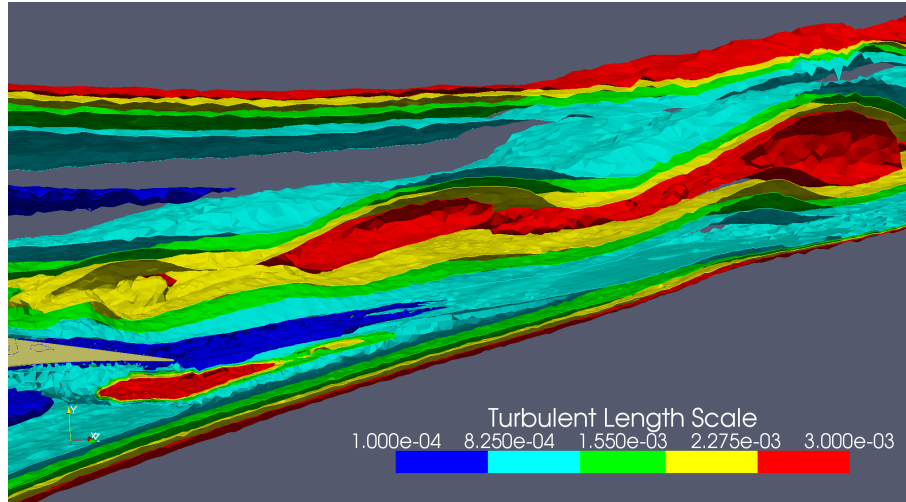


Figure 6.14: Detail of turbulence length scales around the trailing edge of the 0.25 serration ratio geometry.

A close up view of the trailing edge section can be seen in Figure 6.14. The TLS values in this case range through all the calculated contour values inside the wake region with an important and prominent presence of larger scale eddies (in red). These even seem to occur around a small region on the lower end part of the trailing edge. The TLS regions appear to be unstable and would require a time-dependant simulation for a proper behaviour analysis of how they evolve and change in time. Non the less, it's evident that the turbulence has now become anisotropic without there being a dimension in which it seems to share the same properties.

Due to this anisotropy, it's expected that the Proudman/Lilley method will yield inaccurate or misleading results. This comes as a direct result from its handling k and ε values, indistinctly of what kind of turbulence scale is being experienced at a certain point in space. This will lead to a view of sound as a generalized frequency spectrum, which in an isotropic turbulent flow, may indeed accurately be considered to exhibit a broadband profile. When the turbulent flow is anisotropic, the different turbulence length scales will contribute differently and modify the broadband nature of the spectrum. As it was seen in Section 6.1, TLS values, l' , are related to the acoustic frequency they generate as u_k/l' where u_k , the velocity perturbation of the eddy, will be assumed here to have only small variations that don't contribute to the noise frequency.

The most important aspect that this consideration brings up is how similar TLS values contribute constructively to noise generation. In fact, it is expected that when eddies with similar length scales share the same region, the noise generation potential of that region will increase (Lighthill 1954). As an analogy, the presence of TLS of similar values can also have an impact on the structure of a body that mimics acoustic consequences. The adding up of similarly scaled eddies in the flow around such a body can generate mechanical stresses of considerable strength on it, and thus it's often desired to modify its source by retrofitting said body with aerodynamic elements which help widen the range of TLS values being generated. Such is the case of tall industrial chimneys which are constructed with a small, flat helical structure on the upper section, as seen in Figure 6.15. If this element were not to be used, the generated turbulence could exert constructive fluctuations which would induce forces on the chimney of frequencies that are dependant on the incoming wind speed. Due to long term exposure to these forces, or to the oscillations equalling the natural frequency of the chimney, structural damage through fatigue or even collapse could occur.

From a causality point of view, the situation in such a case is exactly the same as in acoustics

but involving fluctuations of much larger scales than those we can hear. Ultimately, the effect is the same; the vibration of a structural element due to turbulent eddies being shed, be that a chimney or our timpani. In the case of aerofoils, the presence of a larger number of similar scaled eddies is expected to exhibit a constructive interference factor to noise generation while, if a region contains a wider range of TLS values, noise may experience as a consequence a reduction in intensity. This extended range is provided by the serration geometry fitted to the blade, as seen in Figure 6.13.

To analyse the acoustic power of different TLS values, Figure 6.16 helps to visualize the ASP regions where two TLS values are contained in. In the sub-figures, TLS contour levels of values 0.003 and 0.002 were obtained and are shown for the 0.25 serration ratio case in the upper frames and 0.50 ratio in the lower ones. These contours are coloured by ASP levels to compare how the same TLS values contribute to noise generation for the two serration geometries. In the 0.25 ratio case, as it was mentioned before, the 0.003 TLS levels, and other higher values, are more prominent on areas closer to the blade's trailing edge and inside its wake region. Here it can be seen that, in comparison to the 0.50 ratio geometry, the 0.003 is particularly much more prominent and appears much closer to the blade, which in turn means that it's closer to the regions with higher ASP levels. In fact, this contour does reach 67 dB at its closest point to the blade, while in the 0.50 ratio blade it merely shows up and its contribution is minimal.

Regarding the 0.002 TLS contour, it appears much more prominently on both geometries, achieving in each case the highest ASP levels shown. The 0.25 ratio case does present a wider contour shape which again appears to be unsteady, contrary to the other case where its edges follow a much straighter path and where the upper and lower limits are closer to one another. Remembering that the wider the volume encompassed by a TLS region, the more power it will output, seeing that ASP levels are given per unit of volume, and thus the 0.25 ratio serrated blade does show to have a much more intense generation of noise from the larger TLS in regard to either the 0.50 ratio or the original blade geometry.

When comparing a 0.001 TLS contour, as seen in Figure 6.17, the differences are still quite evident. Here the original blade is compared to the 0.25 serration ratio case and in both visualizations the 0.001 contour is capped by another contour showing where the 0.002 region starts (shown in grey). It's made evident how much thicker and prominent the 0.001 to 0.002 region is in the original blade than compared to the serrated blade, something which further exemplifies the difference in homogeneity between one case and the other.

A few deductions can be made from these observations. First of all, by following the acoustic frequency's inverse proportional relation to the turbulence length scale that generates the noise, the 0.25 ratio serrations can be expected to generate a lower pitched broadband noise profile than the other cases, with the original blade having the highest pitched profile. This being so, it would mean that the serration ratio plays somewhat a role of being a weight function on the acoustic spectrum which gives it more prominence in the lower ranges as it becomes smaller.



Figure 6.15: Chimney showing the helical structure used to reduce mechanical stress generated by vortex shedding. Source: <http://www.faqs.org/photo-dict/phrase/3609/industrial-chimney.html>

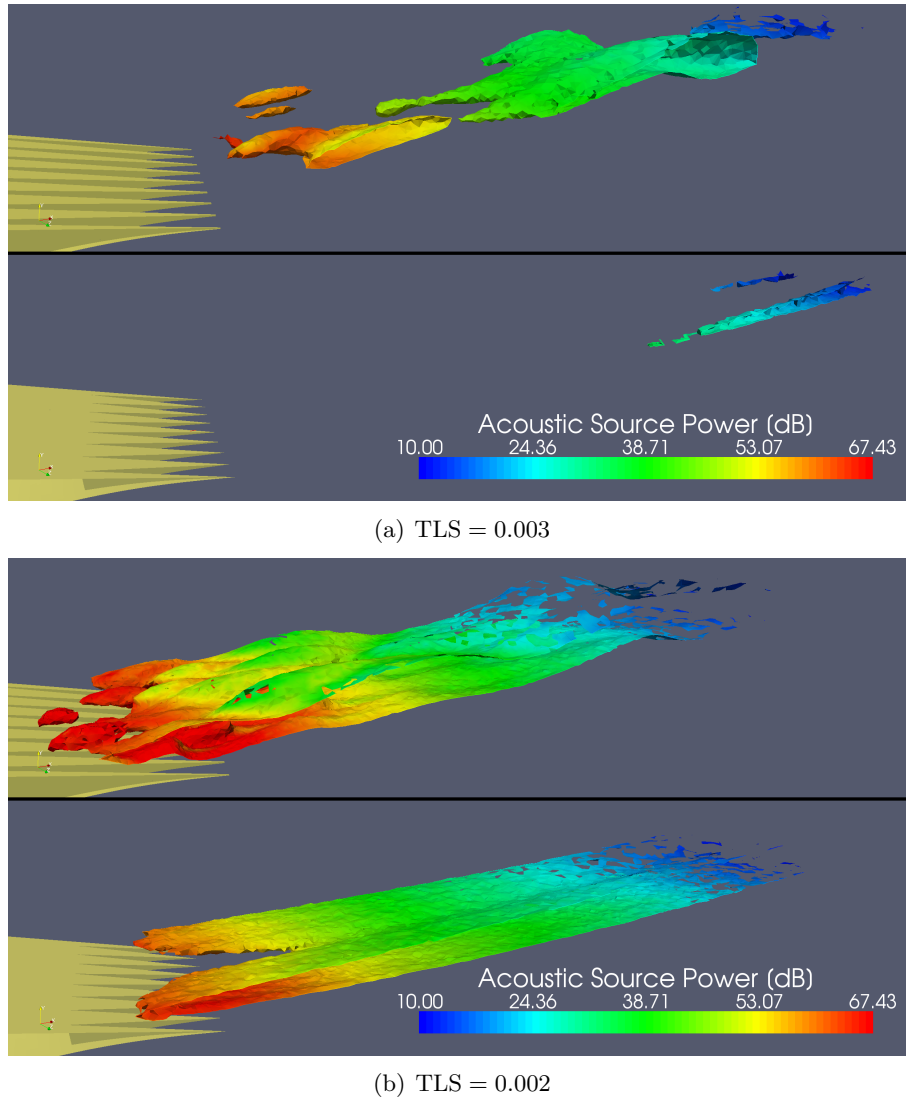


Figure 6.16: Comparison of TLS contours coloured by ASP levels generated by a 0.25 serration ratio (upper frames) and 0.50 (lower frames).

A similar behaviour was observed in the 2D case for higher AOA's and a reference was made to the experimental study conducted in (Hutcheson and Brooks 2006) where a NACA 63-216 showed higher low frequency values at steeper AOA's. Even though this fact was concluded for the 2D analysis, a similar phenomenon is being observed here, where an increase in both generated turbulence intensity and turbulence length scales by the modification of a parameter that changes the flow's behaviour (AOA in the 2D case and the presence of serrations in the 3D case) bring higher TLS levels closer to higher ASP regions, thus causing a similar change in the generated acoustic profile for both types of scenarios.

Concerning the effect of serrations, it has been observed experimentally in (Oerlemans et al. 2001) that, when blades are retrofitted with them, the more evident noise reduction occurs in the higher regions of the acoustic frequency spectrum. This key observation backs the proposed conclusions drawn from this thesis and offers motivation into its applicability.

Secondly, by scaling up the amount of higher valued TLS close to regions of higher acoustic levels, the amount of noise generating eddies with different length scales is also increased, thus helping to avoid having many of similar valued eddies in large regions together, something

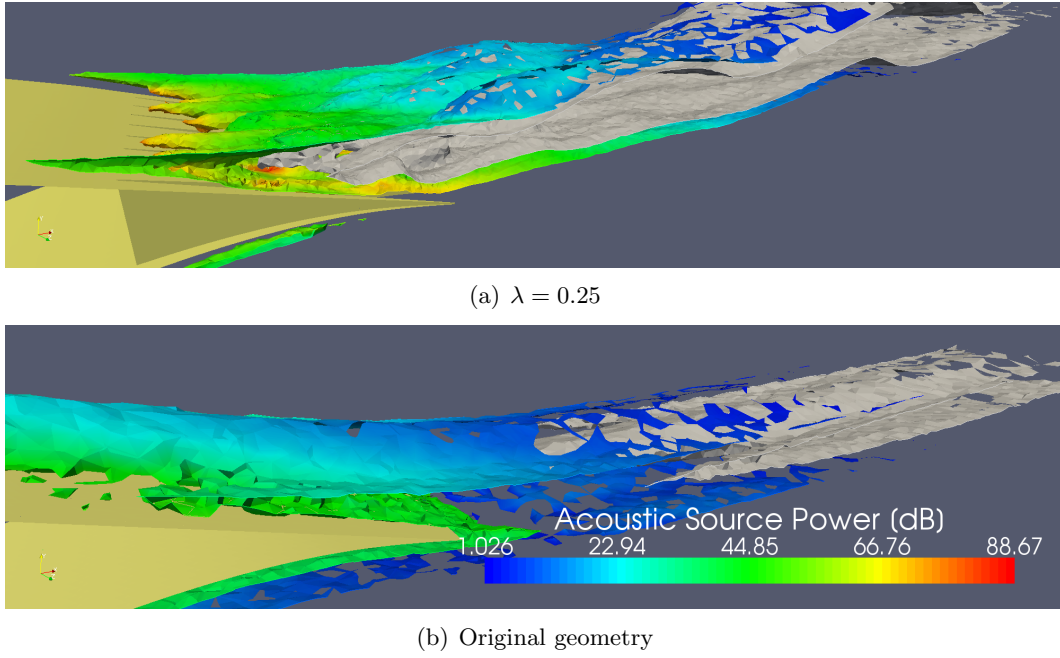


Figure 6.17: Comparison of a 0.001 TLS contours coloured by ASP levels (limited by the 0.002 contour, coloured in grey) for the 0.25 ratio case and the original geometry.

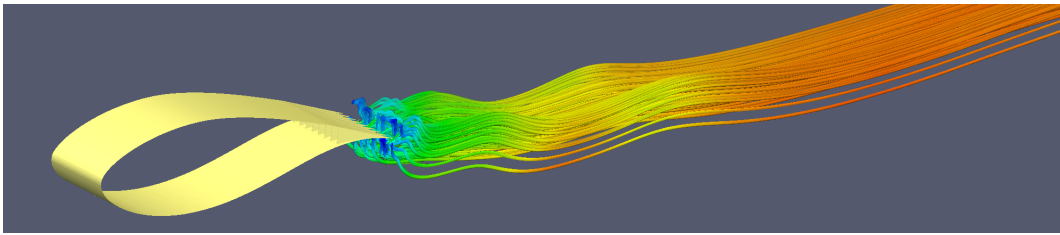


Figure 6.18: Flow is seen to oscillate over a certain length behind the blade as a consequence of the serrations. Here $\lambda/h = 0.25$ and the streamlines and blade have been transformed slightly to emphasize this effect. The colour scale represents flow velocity magnitude.

which may cause a constructive interference pattern in the pressure fluctuations they create, thus emitting more noise. By applying serrations to the blade, a wider range of TLS levels become acoustically active and may help avoid sound peaks in certain frequencies (tonal noise) or even bring down overall broadband noise levels.

Thirdly, fluctuations are seen in the 0.25 serration ratio case. A time-dependant solution should be obtained to properly study the effects they have and how they behave, but it is possible that these oscillations will ultimately excite pressure fluctuations in the fluid at frequencies of low pitched sound, thus negatively contributing to the noise mitigation efforts. They may also be contributing to flutter which, although it may not represent very loud noise properties, could be important in how it interacts with the blade in terms of mechanical stress. Figure 6.18 shows these oscillations as observed in the flow streamlines leaving the trailing edge of the 0.25 serration ratio blade (the streamlines have been scaled to emphasize the vertical movement).

What has been achieved though this analysis is an insight on how a certain serration design affects flow properties, aerodynamic characteristics of the blade, and possible acoustic implica-

tions. The acoustic model used, which follows the theory described by Proudman and Lilley as seen in Section 3.3, fails to predict noise attenuation by itself, possibly as a consequence of the higher level of turbulence anisotropy experienced when serrations are used. Yet, if coupled with an analysis of turbulence length scales, noise behaviour achieves a more complete view where, if increasing the range of TLS acoustically contributing eddies does in fact allow a reduction in the rate of constructive acoustic pressure fluctuations, then the overall noise intensity may be brought down by the use of serrations with a possible shift of the acoustic spectrum to a lower frequency range than compared to an unserrated blade, something which has been previously observed in (Oerlemans et al. 2001).

CONCLUSIONS

The goal pursued in this research has been to analyse how serrations used in wind turbine blades affect noise generation with the intention of outlining a noise reduction strategy.

For this purpose, a series of simulations were run using the $k-\varepsilon$ turbulence model on both 2D and 3D configurations. From these, two 2D cases of different AOA values and three 3D cases of different blade geometry were presented in Chapter 6. The unserrated blade design used follows closely a real-life wind turbine blade profile and the simulations were set to closely recreate this profile's typical operating conditions. A Reynolds number of 5.13×10^6 was used with 0.15 Mach.

The serrations were made by cutting off triangular prisms from the 3D blade. This leaves a serration with a thick edge on its valleys and with sharp points as crests. Two serration ratios were used, $\lambda/h = 0.50$ and 0.25 for λ the serration wavelength and h the amplitude. A rendering of the blade was seen in Figure 5.1 and its dimensions in Figure 5.2.

Aerodynamically, the simulations on the original blades, both in their 2D and 3D configurations gave very good results in terms of expected lift coefficient, and maintain consistent values amongst them for both lift and drag coefficients. In the case of the serrated blades, the lift coefficient was seen to drop sharply as the serration ratio got smaller. This is a clear consequence of having used such an invasive serration design which greatly modifies the blade's original shape by taking away a considerable amount of areas of aerodynamic importance. This effect was expected when deciding on this design, yet it was kept as for several reasons, including that it was expected to fair better in terms of the required grid resolution and that the aerodynamic data would non the less be useful to compare how serration sizes of this type would behave aerodynamically.

To perform the acoustic analysis, a Proudman/Lilley method approach has been used and coupled with an analysis on sound contributing eddy length scales to produce a clearer picture of how the serrations change noise characteristics.

In 2D, the findings indicate that sound is indeed being generated mainly by turbulence structures shed from the trailing edge section of the blade. Secondly, it was shown that noise levels increased from the 1° AOA simulation to the 6° one. Furthermore, when analysing the turbulent length scales (TLS) that are being produced in both cases, the higher AOA showed an increase of lower TLS regions which in turn find themselves in areas of higher acoustic source power (ASP). This indicates that at higher AOA's the sound frequency may shift to the lower side of the spectrum causing lower pitched noise to become more prominent. This hypothesis was observed in (Kim et al. 2006), where sound at around 300 Hz for higher AOA's was shown to be some 6 dB louder. Lastly, sound directivity to regions on the upper downwind section of the domain could be perceiving slightly increased noise levels in comparison to other regions, caused by a more prominent sound generating region that was observed on the suction side of the trailing edge.

The 3D serrated blades were seen to produce a great deal of added turbulence structures, especially at a 0.25 serration ratio. Very inefficient flow structures are seen seeping through the serration teeth which in turn have a big effect on the airflow coming from the upper side of the blade. The serrations displayed a higher pressure level than the areas of the blade that lay before them. Furthermore, the turbulent structures for a 0.25 serration ratio appear to behave in an unsteady fashion, something which would call for that flow to be solved with a time dependent scheme to be fully understood.

Using the Broadband Noise Sources model, the 3D geometry displayed increasing ASP levels for smaller serration ratios and overall larger when compared to the original unserrated blade, opposite from what could be expected by accounting for the hypothesis proposed in (Howe 1990) and experimental data observed in Section 4.5. It is believed that the complex and anisotropic turbulence behaviour, due to the presence of the serrations, causes this model to fail its sound prediction capabilities by neglecting at what frequency sound is being produced. Because of this, a TLS analysis was conducted to pursue a better understanding of the acoustic properties of this, more complex turbulent flow.

It was observed that serrations, somehow like an increasing AOA in the 2D case, will lead to much more varied turbulence structures to be present. Particularly, it was shown, that TLS values increase in regions close to the trailing edge but are also more mixed. This indicates that noise of lower frequency, caused by larger length scale eddies which exist at sound contributing levels, begin to appear, something that has been measured experimentally in (Oerlemans et al. 2001). Following a hypothesis used in (Lilley 1994) which states that TLS of similar values may cause constructive pressure fluctuations that increase sound, then, by decreasing the amount similar TLS levels in the same region and instead injecting different values in it, one could expect a reduction in noise generation of the trailing edge as an effect of the serration influence on the flow.

7.1 Further Work

The treatment of a TLS analysis to compliment the Proudman/Lilley model when studying acoustics seems to fair as an interesting candidate when a limited amount of computational resources are available for the scale of the acoustics problem that is at hand.

Nevertheless, further verification of this method is necessary through experimental or high definition computational methods such as LES or DNS to be able to weigh its contribution potential. Additionally, the accuracy of the two hypothesis used in this research¹ need to be also verified by similar means to cement a better understanding of how serration influenced flows affect sound generation.

Higher resolution computational methods with better turbulence models will yield a better understanding on the different behaviour that was observed between the 2D and 3D models in terms of turbulence measurements in the wake of the blade, something which has direct implications on sound generation.

Transient methods should be applied to complete the modelling of the observed fluctuations in the more turbulent flows. Clearly, they will also be necessary in order to extend the capacity to use more advanced methods such as FW-H, which then can be used on a low scale model to verify the applicability of a TLS-analysis coupled Proudman/Lilley approach. If computational resource availability permits it, a larger scale model would be desired as a simulation candidate to produce a more faithful scenario of more real operating conditions where rotating blades might be considered. This would allow the simulation of radial velocity components on the blade, and other

¹Which are, first, that by reducing the amount of similar noise contributing turbulent scales one is able to reduce overall noise production, and secondly, that TLS indeed generate acoustic frequencies in the order of u_k/l' as proposed in (Stein 1967).

acoustic complexities such as blade/tower interactions, blade tip vortex interactions and how turbulence created from the serrated trailing edges affects the downwind air pattern including regions where other wind turbines may be located and could then be negatively affected.

The application of more computationally expensive and precise models on simpler geometries will allow to study the relation of TLS and sound frequency behaviour. Once this is better established, a clearer conclusion can be drawn from the observed TLS's and especially how they affect sound when they're in a more heterogeneous setting. Achieving this will allow to have better first-hand predictions in the model design of serrated blades and how their geometries can be expected to affect sound. Even more importantly, the TLS-Proudman/Lilley method described in this thesis could gain a higher applicability and, as a direct consequence, a very big relief in computational power requirements can be achieved by not having to use the much more expensive computational aeroacoustics methods that are known today.

DEFINITIONS

A.1 Reynolds Number, Re

The Reynolds number, given by

$$\text{Re} = \rho \frac{LU_\infty}{\mu}$$

is a dimensionless number which relates a characteristic length, L , the mean fluid velocity, U_∞ , the density, ρ , and the dynamic viscosity, μ , of the fluid to give a measure of the ratio of inertial forces, given by

$$\rho \frac{V^2}{L}$$

and the viscous forces,

$$\mu \frac{V}{L^2}$$

thus helping to determine which of them has prominence in defining the fluid's behaviour. If the fluid is mainly inertial then it is expected to behave as a turbulent flow (high Reynolds number), yet if it is predominantly viscous it will behave as laminar (low Reynolds number).

The onset of turbulent flow is a progressive phenomenon that starts at around $\text{Re} = 5 \times 10^3$ to $\text{Re} = 5 \times 10^4$, therefore the Reynolds number is important in predicting how a flow will behave around an object (of L characteristic length). In the case researched in this thesis a Reynolds number of 5×10^5 is used with L equalling the chord length of the blade section that was used.

When doing experimental studies in a wind tunnel, the Reynolds number plays a critical role. By using a principle called dynamic similarity, the subject of the research, e.g. an aircraft, doesn't have to be studied in its full size but instead a smaller scale model can be used as long as one keeps the Reynolds number at the same value. This means that the smaller scale model can be made to behave exactly the same as the full scale body by just changing the fluid's properties, most commonly the mean flow velocity. Thus, if one wishes to model an aircraft flying at 200 m/s but only a 1:4 scale model can be fitted into the wind tunnel, theoretically the flow velocity inside the tunnel can be set to 800 m/s and the same results would be expected.

A.2 The Dimensionless Wall Distance, y^+

The dimensionless wall distance is defined from the wall distance, y , as

$$y^+ = \frac{yu_\tau}{\nu}$$

where ν is the kinematic viscosity of the fluid and u_τ is called the friction velocity which is defined as

$$u_\tau = \sqrt{\tau_w / \rho}$$

where τ_w is the wall shear stress. It is directly related to the dimensionless velocity u^+ as

$$u^+ = \frac{1}{\kappa} \ln y^+$$

where $\kappa \approx 0.41$ is called the Kármán constant. Its usefulness comes when considering the behaviour of viscous fluid near a no-slip wall since it allows the calculation of the dimensionless velocity and the obvious extension to the true velocity in this region. But there are several regions where this law, called the *law of the wall*, is non applicable and other estimations for the friction velocity are used. For $y^+ < 5$, a layer called the viscous sublayer, the equality $u^+ = y^+$ holds instead. Beyond this distance and until 30 wall units one encounters the buffer layer where neither the law of the wall nor the viscous sublayer equality hold.

A.3 The Dirac Delta Function, $\delta(x)$

Heuristically the Dirac delta function can be expressed as an entity that is zero everywhere except at the single point x where its value approaches infinity, thus

$$\delta(x) = \begin{cases} \infty & \text{if } x = 0 \\ 0 & \text{if } x \neq 0 \end{cases}$$

Furthermore, it is constrained to satisfy the identity

$$\int_{-\infty}^{\infty} \delta(x) dx = 1$$

Yet no real function can follow these properties and it would be more rigorously defined as a distribution or measure. As the latter, one can consider it to take an argument being the subset of the real numbers, \mathcal{A} , and returns $\delta(\mathcal{A}) = 1$ if $0 \in \mathcal{A}$ and $\delta(\mathcal{A}) = 0$ otherwise. The integral identity would be explained by considering an idealized mass point placed at 0 such that the integral of δ would come to be the integral of a function against its mass distribution.

A.4 Green's Function¹

Let

$$\mathcal{L}y(x) = f(x) \tag{A.1}$$

an ordinary differential equation where \mathcal{L} is a linear differential operator. Suppose that a function $G(x, z)$ known as Green's function yields the solution to A.1 as

$$y(x) = \int_a^b G(x, z) f(z) dz \tag{A.2}$$

where z is the integration variable and a set boundary conditions in the range $a \leq x \leq b$ are imposed. By applying \mathcal{L} to both sides of A.2 one obtains

$$\mathcal{L}y(x) = \int_a^b [\mathcal{L}G(x, z)] f(z) dz = f(x) \tag{A.3}$$

¹Adapted from (Thijssen 1998)

which leaves

$$f(x) = \int_a^b \delta(x-z) f(z) dz \quad (\text{A.4})$$

a straight substitution from the fundamental defining property of the Dirac δ -function,

$$\int f(t) \delta(t-a) dt = f(a)$$

Equation A.4 then clearly leads to require that

$$\mathcal{L}G(x, z) = \delta(x-z)$$

for A.3 to hold for any arbitrary function $f(x)$. This means that Green's function, $G(x, z)$, must satisfy the original ordinary differential equation with the right hand side set equal to a delta function, thus $G(x, z)$ may be thought of physically as the response of a system to a unit impulse at $x = z$. A number of further restrictions must be set on $G(x, z)$, namely:

- $G(x, z)$ is continuous in x and z
- $\mathcal{L}G(x, z) = 0$ for $x \neq z$
- $\mathcal{B}G(x, z) = 0$ for $z \neq 0$ where \mathcal{B} represents the boundary condition operator
- $\partial^{(i)}G/\partial x^{(i)}$ is continuous up to order $n-2$ at $x = z$ where n is the order of the ordinary differential equation, but $\partial^{(n-1)}G/\partial x^{(n-1)}$ has a discontinuity of $1/a_n(z)$ at $x = z$ where a_n is the n^{th} order coefficient of the differential equation.

Consider now a system described by partial differential equations (PDEs) in the form

$$\mathcal{L}u(\mathbf{r}) = \rho(\mathbf{r}) \quad (\text{A.5})$$

where now \mathcal{L} represents a linear *partial* differential operator such as Laplace's ∇^2 . The PDE can be inhomogeneous in the way that if $u(\mathbf{r})$ is a solution it does not imply that any constant multiple $\lambda u(\mathbf{r})$ is also a solution. If one then seeks a solution to A.5 then the Green function $G(\mathbf{r}, \mathbf{r}_0)$ is a solution of

$$\mathcal{L}G(\mathbf{r}, \mathbf{r}_0) = \delta(\mathbf{r} - \mathbf{r}_0)$$

and the solution to A.5 is given by

$$u(\mathbf{r}) = \int G(\mathbf{r}, \mathbf{r}_0) \rho(\mathbf{r}_0) dV(\mathbf{r}_0)$$

A.5 Wedge Product, \wedge

The wedge product² is the product in an exterior algebra such that, if α and β are differential k -forms of degrees p and q , it follows

$$\alpha \wedge \beta = (-1)^{pq} \beta \wedge \alpha$$

and is not generally commutative but it does follow an associative behaviour,

$$(\alpha \wedge \beta) \wedge u = \alpha \wedge (\beta \wedge u)$$

²As exposed in (Rowland 2010)

as well as being bilinear

$$\begin{aligned}(c_1\alpha_1 + c_2\alpha_2) \wedge \beta &= c_1(\alpha \wedge \beta) + c_2(\alpha_2 \wedge \beta) \\ \alpha \wedge (c_1\beta_1 + c_2\beta_2) &= c_1(\alpha \wedge \beta_1) + c_2(\alpha \wedge \beta_2)\end{aligned}$$

for c_1 and c_2 constants.

In the case treated in this thesis the differential k -forms are degree 1 tensors, i.e. vectors, such that $p = q = 1$ and thus follow

$$\mathbf{v} \wedge \mathbf{w} = -\mathbf{w} \wedge \mathbf{v}$$

for $\mathbf{v}, \mathbf{w} \in \mathbb{R}^n$, where \mathbb{R}^n is a real, n -degree vector space. For this particularity, the wedge product is closely related to the cross and triple products. Having $\{\mathbf{e}_1, \mathbf{e}_2, \dots, \mathbf{e}_n\}$ the basis for the \mathbb{R}^n vector space, then the wedge product of a pair of vectors

$$\begin{aligned}\mathbf{v} &= v_1\mathbf{e}_1 + v_2\mathbf{e}_2 + \dots + v_n\mathbf{e}_n \\ \mathbf{w} &= w_1\mathbf{e}_1 + w_2\mathbf{e}_2 + \dots + w_n\mathbf{e}_n\end{aligned}$$

is, using Einstein summation over the same indices,

$$\begin{aligned}\mathbf{v} \wedge \mathbf{w} &= v_i\mathbf{e}_i \wedge w_j\mathbf{e}_j \\ &= \sum_{i=1}^n \sum_{j=1}^n (v_i w_j - v_j w_i) (\mathbf{e}_i \wedge \mathbf{e}_j)\end{aligned}$$

where

$$\begin{aligned}\{\mathbf{e}_1 \wedge \mathbf{e}_2, \mathbf{e}_1 \wedge \mathbf{e}_3, \dots, \mathbf{e}_1 \wedge \mathbf{e}_n, \\ \mathbf{e}_2 \wedge \mathbf{e}_1, \mathbf{e}_2 \wedge \mathbf{e}_3, \dots, \mathbf{e}_2 \wedge \mathbf{e}_n, \\ \dots, \mathbf{e}_n \wedge \mathbf{e}_1, \mathbf{e}_n \wedge \mathbf{e}_2, \dots, \mathbf{e}_n \wedge \mathbf{e}_{n-1}\}\end{aligned}$$

is the basis for the $\wedge^2(\mathbb{R}^n)$ space. This is, for this vector space, the same definition as for the cross product, $\mathbf{v} \times \mathbf{w}$. If one were to use a third vector, \mathbf{u} , also defined in \mathbb{R}^n , then $\mathbf{u} \wedge \mathbf{v} \wedge \mathbf{w}$ would imitate the triple product, $\mathbf{u} \cdot (\mathbf{v} \times \mathbf{w})$.

BIBLIOGRAPHY

- Aerts, J. and Dirckx, J. (2009). Nonlinearity in eardrum vibration as a function of frequency and sound pressure, *Hearing Research* **In Press, Corrected Proof**: –.
- Ask, J. and Davidson, L. (2010). Flow and dipole source evaluation of a generic SUV, *Journal of Fluids Engineering* **132**: 051111.
- Bardina, J., Ferziger, J. and Reynolds, W. (1980). Improved subgrid-scale models for large-eddy simulation, *American Institute of Aeronautics and Astronautics, Fluid and Plasma Dynamics Conference, 13th, Snowmass, Colo., July 14-16, 1980*, 10 p.
- Batchelor, G. (2000). *An introduction to fluid dynamics*, Cambridge Univ Pr.
- Beranek, L. and Vér, I. (1992). *Noise and Vibration Control Engineering: Principles and Applications*, John Wiley & Sons.
- Bertagnolio, F. (2008). Trailing edge noise model applied to wind turbine airfoils, *Technical report*, Forskningscenter Risø Roskilde.
- Brentner, K. and Farassat, F. (1994). Helicopter noise prediction: the current status and future direction, *Journal of sound and vibration* **170**(1): 79–96.
- Brentner, K. and Farassat, F. (1998). An analytical comparison of the acoustic analogy and Kirchhoff formulation for moving surfaces, *AIAA journal*.
- Brentner, K. and Farassat, F. (2003). Modeling aerodynamically generated sound of helicopter rotors, *Progress in Aerospace Sciences* **39**(2-3): 83–120.
- Brentner, K., Perez, G. and Bres, G. (2002). Toward a better understanding of maneuvering rotorcraft noise, *AHS International, 58 th Annual Forum Proceedings*-, Vol. 2, pp. 1552–1562.
- Brooks, T. and Hodgson, T. (1981). Trailing edge noise prediction from measured surface pressures, *Journal of Sound and Vibration* **78**(1): 69–117.
- Brooks, T., Pope, D. and Marcolini, M. (1989). Airfoil self-noise and prediction, *National Aeronautics and Space Administration Reference Publication Number 1218*.
- Chase, D. (1980). Modeling the wavevector-frequency spectrum of turbulent boundary layer wall pressure, *Journal of Sound and Vibration* **70**(1): 29–67.
- Crocker, M. (1998). *Handbook of acoustics*, Wiley-Interscience.

- Curle, N. (1955). The influence of solid boundaries upon aerodynamic sound, *Proceedings of the Royal Society of London. Series A, Mathematical and Physical Sciences* **231**(1187): 505–514.
- Dozolme, A., Metwally, H. and Marchal, T. (2006). Electronics Cooling Fan Noise Prediction.
- Ene (1997). *Planning Advice Note PAN 45: Annex 2: Spatial Frameworks and Supplementary Planning Guidance for Wind Farms*. Energy Technology Support Unit.
- Ewert, R. and Schröder, W. (2003). Acoustic perturbation equations based on flow decomposition via source filtering, *Journal of Computational Physics* **188**(2): 365–398.
- Ewert, R. and Schröder, W. (2004). On the simulation of trailing edge noise with a hybrid LES/APE method, *Journal of Sound and Vibration* **270**(3): 509–524.
- Farassat, F. and Brown, T. (1977). A new capability for predicting helicopter rotor and propeller noise including the effect of forward motion, *NASA*.
- Ferziger, J., Peric, M. and Morton, K. (1999). *Computational methods for fluid dynamics*, Springer Berlin.
- Ffowcs-Williams, J. E. and Hawkings, D. L. (1969). Sound Generation by Turbulence and Surfaces in Arbitrary Motion, *Royal Society of London Philosophical Transactions Series A* **264**: 321–342.
- Ffowcs-Williams, J. (1995). Aeroacoustics, *Journal of Sound and Vibration*.
- Fields, J. (1990). A quantitative summary of non-acoustical variables’ effects on reactions to environmental noise, *Busch-Vishniac, I., ed, 1990 National Conference on Noise Control Engineering: Reducing the Annoyance of Noise, Univ. Texas, Austin, TX*.
- Fluent 6.3, User’s Guide* (2006).
- Garrad, A. (1991). Wind energy in europe—time for action, *Technical report*, EWEA.
- Guidati, G., Wagner, S., Parchen, R., Oerlemans, S., van den Berg, R., Schepers, G., Braun, K. and Kooi, J. (1999). Design and testing of acoustically optimized airfoils for wind turbines (DATA), *1999 European Wind Energy Conference: wind energy for the next millennium: proceedings of the European Wind Energy Conference, Nice, France, 1-5 March 1999*, Earthscan/James & James, p. 101.
- Herbrandson, C. and Messing, R. (2009). Public health impacts of wind turbines, *Technical report*, Minnesota Department of Health, Environmental Health Division.
- Herrig, A., Würz, W. and Wagner, S. (2003). Silent rotors by acoustical optimization (SIROCCO), *Technical report*, Institute of Aerodynamic and Gas Dynamics, University of Stuttgart.
- Hoen, B., Wiser, R., Cappers, P., Thayer, M. and Sethi, G. (2009). The Impact of Wind Power Projects on Residential Property Values in the United States: A Multi-Site Hedonic Analysis, *Technical report*, Ernest Orlando Lawrence Berkeley National Laboratory.
- Horváth, C. and Vad, J. (2009). Broadband noise source model acoustical investigation on unskewed and skewed axial flow fan rotor cascades, *Conference on Modelling Fluid Flow, Budapest, Hungary*.

- Howe, M. (1978). A review of the theory of trailing edge noise, *Journal of Sound and Vibration* **61**(3): 437–465.
- Howe, M. (1990). Aerodynamic noise of a serrated trailing edge, *Journal of Fluids and Structures*.
- Howe, M. (1999). Trailing edge noise at low Mach numbers, *Journal of Sound and Vibration* **225**(2): 211–238.
- Howe, M. (2000). Trailing edge noise at low Mach numbers, part 2: Attached and separated edge flows, *Journal of Sound and Vibration* **234**(5): 761–775.
- Howe, M. (2006). Contributions to the theory of aerodynamic sound, with application to excess jet noise and the theory of the flute, *Journal of Fluid Mechanics* **71**(04): 625–673.
- Hu, F., Hussaini, M. and Manthey, J. (1996). Low-dissipation and low-dispersion Runge-Kutta schemes for computational acoustics, *Journal of Computational Physics* **124**(1): 177–191.
- Hutcheson, F. and Brooks, T. (2006). Effects of angle of attack and velocity on trailing edge noise, *International Journal of Aeroacoustics*.
- Kato, C., Yamade, Y., Wang, H., Guo, Y., Miyazawa, M., Takaishi, T., Yoshimura, S. and Takano, Y. (2007). Numerical prediction of sound generated from flows with a low Mach number, *Computers & Fluids* **36**(1): 53–68.
- Khondge, A., Sovani, S., Kim, S., Guzy, S. and Farag, A. (2005). On Predicting Aeroacoustic Performance of Ducts With Broadband Noise Source Models, *Technical report*, SAE International.
- Kim, H., Lee, S. and Fujisawa, N. (2006). Computation of unsteady flow and aerodynamic noise of NACA0018 airfoil using large-eddy simulation, *International Journal of Heat and Fluid Flow* **27**(2): 229–242.
- Larsson, J., Davidson, L., Eriksson, L. and Olsson, M. (2004). Aeroacoustic Investigation of an Open Cavity at Low Mach Number, *AIAA Journal* **42**: 2462–2473.
- Lele, S. (1992). Compact finite difference schemes with spectral-like resolution, *Journal of Computational Physics* **103**(1): 16–42.
- Lighthill, M. J. (1952). On Sound Generated Aerodynamically. I. General Theory, *Royal Society of London Proceedings Series A* **211**: 564–587.
- Lighthill, M. J. (1954). On sound generated aerodynamically. II. Turbulence as a source of sound, *Proceedings of the Royal Society of London. Series A, Mathematical and Physical Sciences* pp. 1–32.
- Lilley, G. (1994). The radiated noise from isotropic turbulence, *Theoretical and Computational Fluid Dynamics* **6**(5): 281–301.
- Mansour, N., Kim, J. and Moin, P. (2006). Reynolds-stress and dissipation-rate budgets in a turbulent channel flow, *Journal of Fluid Mechanics* **194**: 15–44.
- Moorhouse, A., Hayes, M., von Hünerbein, S., Piper, B. and Adams, M. (2007). Research into aerodynamic modulation of wind turbine noise, *Technical report*, University of Salford.
- Morris, P., Long, L. and Brentner, K. (2004). An aeroacoustic analysis of wind turbines, *AIAA Paper* **1184**: 2004.

- Morris, P., Long, L., Bangalore, A. and Wang, Q. (1997). A parallel three-dimensional computational aeroacoustics method using nonlinear disturbance equations, *Journal of Computational Physics* **133**(1): 56–74.
- Oerlemans, S. and Méndez-López, B. (2005). Acoustic array measurements on a full scale wind turbine, *AIAA Paper 2005-2963, Eleventh AIAA/CEAS Aeroacoustics Conference*, Vol. 23, p. 25.
- Oerlemans, S., Schepers, J., Guidati, G. and Wagner, S. (2001). Experimental demonstration of wind turbine noise reduction through optimized airfoil shape and trailing-edge serrations, *Nationaal Lucht en Ruimtevaartlaboratorium, NLR TP*.
- Off (2004). *Planning Policy Statement 22: Renewable Energy*. The Office of the Deputy Prime Minister of the United Kingdom.
- Parchen, R. (1998). Progress report DRAW: A prediction scheme for trailing-edge noise based on detailed boundary-layer characteristics, *TNO Rept. HAGRPT-980023, TNO Institute of Applied Physics, The Netherlands*.
- Patidar, A. (2009). Designing automotive rear air handling system for low flow induced noise using Broadband Noise Source and Ffowcs-Williams & Hawkings models, *Technical report*, SAE International.
- Pedley, T. (2001). James Lighthill and his contributions to fluid mechanics, *Annual Review of Fluid Mechanics* **33**(1): 1–41.
- Powell, A. (1960). Aerodynamic noise and the plane boundary, *The Journal of the Acoustical Society of America* **32**: 982.
- Proudman, I. (1952). The generation of noise by isotropic turbulence, *Proceedings of the Royal Society of London. Series A, Mathematical and Physical Sciences* pp. 119–132.
- Rogers, A. and Manwell, J. (2004). Wind turbine noise issues, *Technical report*, Renewable Energy Research Laboratory, University of Massachusetts at Amherst.
- Rowland, T. (2010). Wedge product, *MathWorld—A Wolfram Web Resource*. <http://mathworld.wolfram.com/WedgeProduct.html>.
- Sagrillo, M. (2010). Putting wind power’s effect on birds in perspective, <http://www.awea.org/faq/sagrillo/swbirds.html>.
- Sarkar, S. and Hussaini, M. (1993). Computation of the sound generated by isotropic turbulence, *NASA STI/Recon Technical Report N 94*: 21880.
- Sco (2002). *Planning Advice Note PAN 45: Annex 2: Spatial Frameworks and Supplementary Planning Guidance for Wind Farms*. The Scottish Government.
- Shih, T. (1990). An improved k-epsilon model for near-wall turbulence and comparison with direct numerical simulation, *NASA STI/Recon Technical Report N 90*: 27983.
- Singer, B., Brentner, K., Lockard, D. and Lilley, G. (1999). Simulation of acoustic scattering from a trailing edge, *The Journal of the Acoustical Society of America* **105**: 950.
- Smagorinsky, J. (1963). General circulation experiments with the primitive equations, *Monthly weather review* **91**: 99–164.

- Sovani, S. (2005). Aeroacoustics modeling, *Fluent Lunch and Learn seminar series, St. John's Conference Center, Plymouth, MI*.
- Spalart, P., Jou, W., Stretlets, M. and Allmaras, S. (1997). Comments on the feasibility of LES for wings and on the hybrid RANS/LES approach, *Advances in DNS/LES: proceedings of the First AFOSR International Conference on DNS/LES, Louisiana Tech University, Ruston, Louisiana, August 4-8, 1997*, Greyden Press, p. 137.
- Stein, R. (1967). Generation of acoustic and gravity waves by turbulence in an isothermal stratified atmosphere, *Solar Physics* **2**(4): 385–432.
- Tam, C. (2004). Computational aeroacoustics: An overview of computational challenges and applications, *International Journal of Computational Fluid Dynamics* **18**(6): 547–567.
- Tam, C. and Dong, Z. (1996). Radiation and outflow boundary conditions for direct computation of acoustic and flow disturbances in a nonuniform mean flow, *Journal of Computational Acoustics* **4**(2): 175–201.
- Tam, C. and Webb, J. (1992). Dispersion-relation-preserving schemes for computational aeroacoustics, *DGLR/AIAA Aeroacoustics Conference, 14th, Aachen, Germany*, pp. 214–222.
- Tam, C. and Webb, J. (1993). Dispersion-relation-preserving finite difference schemes for computational acoustics, *Journal of Computational Physics* **107**(2): 262–281.
- Thijssen, J. (1998). Mathematical Methods for Physics and Engineering: A Comprehensive Guide, *European Journal of Physics*.
- Tsai, C., Fu, L., Tai, C., Huang, Y. and Leong, J. (2009). Computational aero-acoustic analysis of a passenger car with a rear spoiler, *Applied Mathematical Modelling* **33**(9): 3661–3673.
- Wagner, S., Bareiss, R. and Guidati, G. (1996). *Wind Turbine Noise*, Springer, Berlin.
- Weed, C. (2006). Examples of noise standards and wind turbine noise regulations, *Technical report*, The Centerville Township Commercial Wind Ordinance Committee.
- Wilcox, D. (1998). Turbulence modeling for CFD.
- Yokokawa, M., Ken'ichi Itakura, A., Ishihara, T. and Kaneda, Y. (2002). 16.4-Tflops direct numerical simulation of turbulence by a Fourier spectral method on the Earth Simulator.
- Zhu, W. (2007). *Aero-Acoustic Computations of Wind Turbines*, PhD thesis, Technical University of Denmark.

ACRONYMS

AOA	Angle of Attack
APE	Acoustic Perturbation Equations
ASP	Acoustic Source Power
CAA	Computational Aeroacoustics
CFD	Computational Fluid Dynamics
DES	Detached Eddy Simulation
DNS	Direct Numerical Simulation
FLOPS	Floating Point Operations Per Second
FW-H	The Ffowcs-Williams and Hawkings aeroacoustics method
LEE	Linearised Euler Equations
LES	Large Eddy Simulation
NACA	National Advisory Committee for Aeronautics, which later became to be the National Aeronautics and Space Agency, NASA, and here refers to NACA aerofoils, a convention to calculate aerofoil shapes from, usually, a four or five number series.
NLDE	Non-Linear Disturbance Equations
ODE	Ordinary Differential Equations
PDE	Partial Differential Equations
RANS	Reynolds Averaged Navier-Stokes equations
TLS	Turbulent Length Scale
URANS	Unsteady Reynolds Averaged Navier-Stokes equations